The Mass Composition of
Ultra-High Energy Cosmic Rays
Observed by Telescope Array Observatory

Department of Physics, Graduate School of Science,

Tokyo Institute of Tehcnology

06D01070

Yuichiro TAMEDA

March 17, 2010

Contents

Abstract

After the discovery in 1912, cosmic rays were observed over the wide range of energies from 10^9 to 10^{20} eV. In particular, the existence of ultra-high energy cosmic rays (UHECRs) above 10^{18} eV is still attractive issue although the first observation is in 1963. In the energy spectrum above 10^{19} eV, the suppression was predicted so-called Greisen-Zatsepin-Kuzmin (GZK) cutoff. The energy spectrum of HiRes or Pierre Auger observatory (PAO) is in the good agreement with GZK cutoff. However, AGASA observed the eleven events which are contrary to the prediction. Moreover, PAO reported the correlation between the arrival directions and nearby AGNs, but the correlation is not consistent with the mass composition observed by PAO. On the other hand, HiRes suggested that the mass composition is dominated by pure proton which contradicts that of PAO.

The mass composition is quite important to investigate the origins of UHECRs. If the mass composition is determined, following subjects are expected to be constrained; the source models either acceleration by astronomical objects or new physics associated with the GUTs energy scale and the interpretation of "ankle" which is the bending structure in the energy spectrum.

In order to clarify the origins of UHECRs, Telescope Array (TA) experiment started observation from Nov. 2007 at the west desert in Utah, U.S. TA performs the hybrid measurements using the fluorescence detectors (FDs) of HiRes type, and surface detector ground array of AGASA type.

The mass composition analysis is achieved to compare the $X_{\max}$ distribution between the data and simulated air showers, where $X_{\max}$ is the atmospheric depth at which the number of shower particles reach maximum. The data is acquired by the FDs from Nov. 2007 to Oct. 2009. Analysis is applied for the data observed in the stereoscopic geometry. The $X_{\max}$ distribution of the data shows good agreement with a simulated distribution based on the pure proton composition model. The average $X_{\max}$ as the function of energy is also consistent with the pure proton composition.

Chapter 1

Introduction

Cosmic rays were discovered by V.F. Hess in 1912. After the discovery, various experiments have observed cosmic rays in the wide range of energies, from 10^9 to 10^{20} eV [71]. In any era, cosmic rays have been good proves for high energy physics because particles with energy of much higher than the limit of accelerator can be available in cosmic rays. For example, pions were discovered by the observation of cosmic rays interaction. At the present, it becomes possible to observe ultra-high energy cosmic rays (UHECRs) with energy around 10^{19} eV. UHECRs study has potential to clarify the extremely high energy phenomenon such as related to a grand unification theory. In general, cosmic rays are mainly charged particles, so that it is difficult to trace back the sources due to the interaction with magnetic fields. However, trajectories of UHECRs are not disturbed or much less. Thus, in the point of view of astronomy, UHECRs observations are expected as a start of particle astronomy.

The energy range of cosmic rays which can be detected is extended up to 10^{20} eV due to the progress of the detection technique. The existence of UHECRs is still attractive issue although the first observation is in 1963 [52]. It is predicted that the cosmic-ray flux of energy above 10^{19} eV suffers from suppression due to the interaction with cosmic microwave background photons, so called Greisen-Zatsepin-Kuzmin (GZK) cutoff [36, 91]. In the end of the twentieth century, High Resolution Fly's Eye (HiRes) and Akeno Giant Air Shower Array (AGASA) can be enumerated as representative experiments of UHECRs. AGASA is the ground array of particle detectors

with detection area of $100\,\mathrm{km}^2$, while HiRes adopts the fluorescence technique. HiRes experiment reported the energy spectrum of GZK energy region which is consistent with the GZK cutoff [3]. On the other hand, AGASA observed 11 events with energy above $10^{20}\,\mathrm{eV}$ [73]. In this case, though the source of such events should be located within $\sim 100\,\mathrm{Mpc}$, related sources have not been identified, yet. The existence of GZK cutoff has not been concluded due to systematic uncertainty of $\sim 20\%$ in the energy determination of both experiments. It is also the factor of difficulty to observe UHECRs that the arrival frequency is quite small as the primary energy increases, as $\propto E^{-3.1}$. For the detailed investigation, larger exposure and higher accuracy are required. In the case of mass composition, the result of Fly's Eye shows the change from heavy dominant to light dominant above $10^{17}\,\mathrm{eV}$ [18]. On the other hand, AGASA didn't detect the systematic change from the properties of muons [37].

In the beginning of this century, Pierre Auger Observatory (PAO) and Telescope Array (TA) have started observations of UHECRs. Both experiments have larger aperture than previous experiments. Additionally, hybrid system which consists of two type detectors, ground array of particle detectors and fluorescence telescopes, are adopted. PAO is located in the southern hemisphere, while TA is located in the northern hemisphere. AGASA and HiRes are also located in the northern hemisphere. PAO started observation several year earlier than TA. Thus, PAO has already reported the energy spectrum and composition of UHECRs. The report of energy spectrum is consistent with GZK prediction [9]. On the other hand, it is interesting that the composition of UHECRs shows the contrary to the result of HiRes. The composition of HiRes favors proton dominant composition [2], but that of PAO favors the transition to heavy components [7].

The mass composition of UHECRs is a clue to clarify the origins of that. When origins of UHECRs are astronomical objects, the composition should consist of atomic nucleus, such as protons or heavier up to iron. The models of astronomical origin can be constrained. If the composition favors more light component such as neutrino or photons, new physics should be taken into account. Not only the source models but also the interpretation of the shape of energy spectrum can be constrained, such as ankle which is the bend structure around $10^{19}\,\mathrm{eV}$. Moreover, the consistency in the

correlation between the arrival direction and AGN reported by PAO [8] should be verified. Thus the mass composition should be considered for any subjects concerned with UHECRs.

TA started the full operation from Dec. 2007. The hybrid measurement using ground array and fluorescence telescopes is achieved. In this analysis, the first two years data of stereo events, observed by two fluorescence telescope stations, are analyzed. The mass composition of UHECR observed in northern hemisphere is discussed.

Chapter 2

Cosmic Rays

2.1 Energy Spectrum

Cosmic rays are high energy particles coming from outer space. The flux of cosmic rays mainly consists of protons, nuclei or electrons, and in a wide sense gamma rays or neutrinos. In 1912, cosmic rays were discovered by Austrian physicist V.F.Hess. Since the discovery, many experiments have observed cosmic rays with the various energies from 10^7 to 10^{20} eV by the progress of detection technique (Fig. 2.1). Cosmic rays with energy below 10^{15} eV are measured directly by balloons or space based experiments. However direct measurement of high energy cosmic rays with energy above 10^{13} eV is difficult due to their poor statistics, the arrival frequency of cosmic rays decreases proportional to the power law of their energies. Thus high energy cosmic rays are observed indirectly by the measurements of cosmic-ray air showers caused by the interaction with atmospheric nuclei.

Cosmic rays measurement in the energy range above 10^{10} eV does not suffer from the solar activity and the cosmic-ray spectrum is approximately proportional to the power law of energy. The bend of the energy spectrum around the energy 10^{15} eV and 10^{19} eV are called "knee" and "ankle", respectively. The flux of cosmic rays in the energy region below "knee", above "knee" and above "ankle" are approximated as $\propto E^{-2.7}$, $\propto E^{-3.0}$ and $\propto E^{-2.7}$, respectively. The energy spectrum in the energy range above 10^{20} eV has not been confirmed yet due to the low statistics or unknown

systematic errors. The Pierre Auger Observatory (PAO) and Telescope Array (TA) experiment started observation of the ultra-high energy cosmic rays above 10^{18} eV with larger aperture than the previous experiments to clarify the origin.
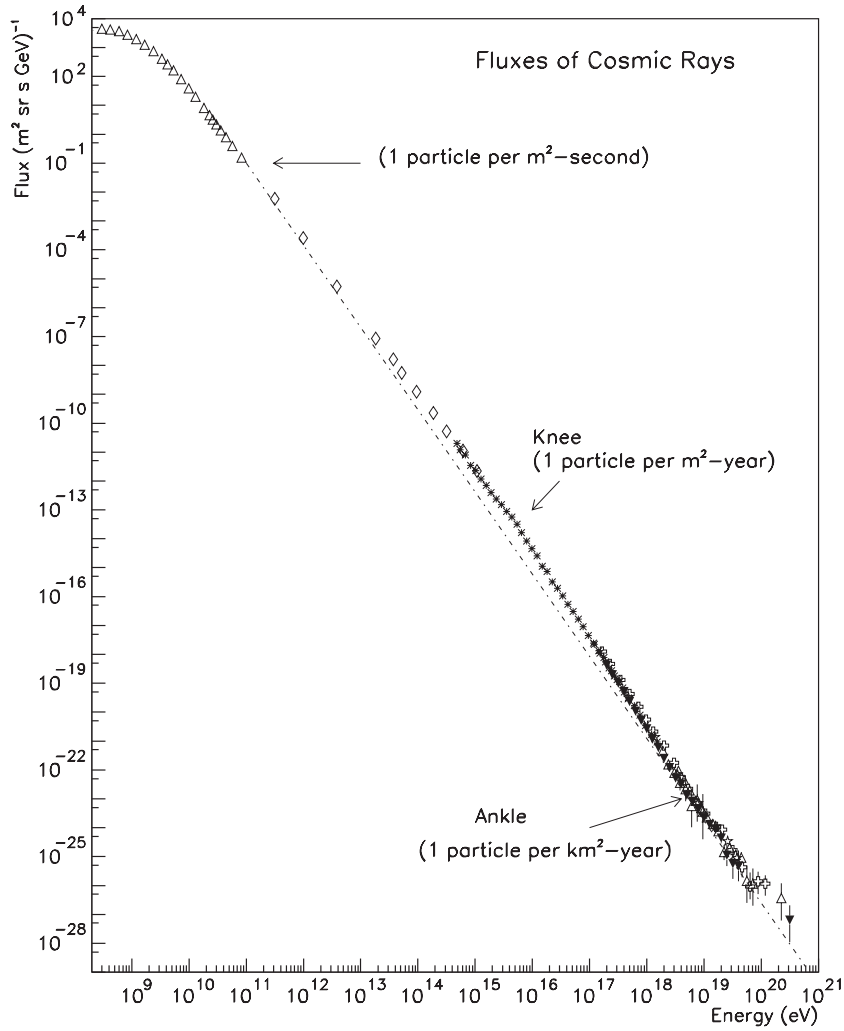

Figure 2.1: Cosmic-ray energy spectrum greater than 10^9 eV observed by the various experiment [71].
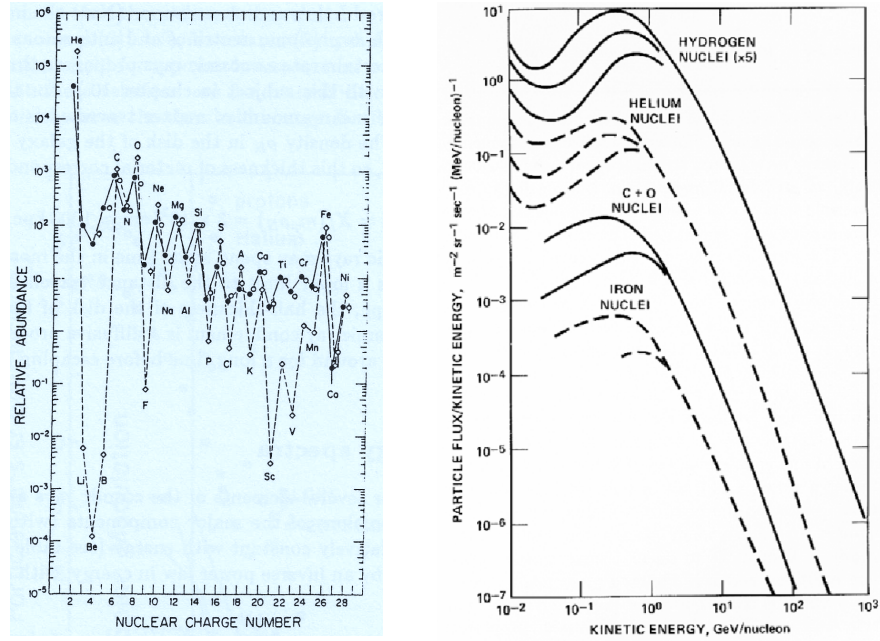
Figure 2.2: Left: The chemical abundance of cosmic rays (filled circles) and that of the solar system (diamond). Right: Cosmic-ray energy spectrum for each species.

2.2 Composition

The cosmic-ray abundance compared with that of solar system is shown in the left of Fig. 2.2. In the abundance, the even-odd regularity with atomic number is shown similar as that of the solar system. The most distinguished feature is the excess of two nuclei groups (Li, Be, B) and (Ti, V, Cr, Mn). This characteristic feature is due to the spallation of carbon or oxygen for (Li, Be, B) and of iron for (Ti, V, Cr, Mn) which interact with the interstellar medium (ISM). The cross sections of spallation are known; therefore, we can estimate the amount of matter traversed by cosmic rays, $X = 5 \sim 10\,\mathrm{g/cm^2}$. The number density of cosmic rays in the galaxy, ρ_N, is about one particle per $\mathrm{cm^3}$, so the thickness of matter is correspond to a distance $l = X/(m_p \rho_N) = 1\,\mathrm{Mpc}$, where m_p is the proton mass. This distance is much larger than the thickness of the galactic disc; thus cosmic rays are confined in the galaxy before escape.

The energy spectra of each component are shown in right of Fig. 2.2. Below the

energy of 10^9 eV, the flux does not show the power low due to the influence of the solar magnetic field and therefore suffers from the solar activity.

2.3   Cosmic-Ray Origin

The energy density of cosmic rays nearby the solar system is ~ 1 eV per cm^3 and this is comparable with that of the galactic magnetic field of 0.3 eV per cm^3. Thus, it is natural to assume that there are energy conversion between cosmic-ray charged particles and the galactic magnetic field. When the radius and thickness of the galactic disc are 15 kpc and 1.5 kpc respectively, the amount of energy is 10^{48} J. When the life time of cosmic rays in the galactic plane is 10^7 y, the generation rate of cosmic rays should be 3×10^3 W. When the typical energy of a super nova explosion is supposed to 10^{44} J and contribution of the cosmic-ray acceleration is $\sim 3\%$ of the total energy, the amount of cosmic-ray energy is supplied enough if an explosion occurs every 30 y.

Cosmic rays with energy below 10^{15} eV are confined by the galactic magnetic field, and those of origin are therefore assumed to be the galactic. However, in the case of high energy cosmic ray above 10^{18} eV, since Larmor radius of cosmic rays becomes larger than the thickness of galactic plane, it is expected that the distribution of arrival direction shows anisotropic under the assumption of the galactic sources model.

2.4   Acceleration Mechanism

In general, acceleration of particles is mainly dynamic, hydrodynamic and electromagnetic. For example, collision of particles with cloud is purely dynamical acceleration. Acceleration of plasma is described by hydrodynamic. The electromagnetic acceleration are caused by electric fields, such as neutral sheets, electromagnetic or plasma wave and magnetospheres of neutron stars.

The acceleration of a charged particle in electromagnetic field is expressed as following.

$$\frac{d}{dt}(\gamma m \boldsymbol{v}) \;=\; e(\boldsymbol{E} + \boldsymbol{v} \times \boldsymbol{B}), \qquad (2.1)$$

where γ, m, v and e are Lorentz factor, mass, velocity and charge of particle and $\boldsymbol{E}$, $\boldsymbol{B}$ are the electric and magnetic field. However, in most astrophysical environments, static electric fields cannot be maintained because of the very high electrical conductivity of ionized gases. Thus, the electric field of intergalactic space is globally neutral. Therefore, the acceleration mechanism can be associated with either non-stationary electric fields or time-varying magnetic fields. However, it seems difficult to accelerate to high energy efficiently.

2.4.1 Fermi Second-Order Mechanism

The basic idea of the acceleration mechanism of high energy cosmic rays by stochastic collisions is proposed by Fermi in 1949 [31]. In this idea, charged particles are reflected by magnetic mirrors associated with irregularities in the galactic magnetic field. The mirrors are assumed to move randomly with typical velocity V, and the particles gain energy statistically in these reflections. If the particles remain within the acceleration region, power law distribution of particle energies is derived naturally.

In this model, the mean energy gain is given by

$$\left\langle \frac{\Delta E}{E} \right\rangle = \frac{8}{3}\beta^2, \tag{2.2}$$

where $\beta = V/c$ is the mean non-relativistic velocity of the clouds in units of the light speed in vacuum. The energy gain increases as β^2, depends on only velocity of the clouds, and neither the magnetic field strength nor charge of particles.

The second-order Fermi mechanism results in a spectral distribution $N(E)$ in the form of a power law: $N(E) \sim E^{-n}$, where $N(E)dE$ is the number of particles with energy between E and $E + dE$.

However, there are a few problems as the acceleration mechanism of cosmic-ray origin. First of all, the random velocity of magnetic clouds is $\beta \sim 10^{-4}$. Additionally, the mean free path in the ISM is estimated to be $\sim$ pc and the number of collisions would be roughly one per year. Therefore, average gain of energy is very small, $< \Delta E/E > \sim 10^{-8}$. Unless we adopt the special case, small scale turbulence, such as the shell of young supernova remnants, this model is hopeless. Second, the effect of

energy losses is not considered. At the low energies, ionization losses is not negligible. Finally, there is an ambiguity in the index of the energy spectrum.

2.4.2 Acceleration at Shocks

Acceleration at the non-relativistic shock preceding the expansion of matter flowing at speeds larger than the speed of sound in the medium is more efficient than Fermi second-order, which is called as the first-order Fermi acceleration [19]. In this case, the average energy gain is

$$\left\langle \frac{\Delta E}{E} \right\rangle = \frac{4}{3}\beta, \tag{2.3}$$

where β is the shock velocity. In the second-order Fermi acceleration, process is not efficient because of that energy gain results in the small differential between the head-on collision and following collision. In the case of magnetically turbulent plasma, the collision of a particle is considered as only head-on collision.

2.5 Ultra-High Energy Cosmic Ray

2.5.1 UHECR Propagation

Cosmic rays are mostly charged particles so that the interaction with magnetic field is important for understanding the origins. The interaction with $2.7\,\mathrm{K}$ Cosmic Microwave Background (CMB) photons cannot be neglected for ultra-high energy cosmic rays (UHECRs) with energy above $\sim 10^{19}\,\mathrm{eV}$.

Interaction with Magnetic Fields

Cosmic rays are assumed as charged particles mostly protons. Thus, the interaction with the galactic magnetic field should be taken into account. The Larmor radius of

cosmic rays with energy E in the magnetic field B is

$$R \sim \left(\frac{E}{10^{19}\,\mathrm{eV}} \right) \left(\frac{3\mu G}{B} \right) \times 3\,\mathrm{kpc}. \tag{2.4}$$

The Larmor radius becomes $\sim 3.0\,\mathrm{kpc}$ for a proton with energy of $10^{19}\,\mathrm{eV}$ in the galactic magnetic field of $\sim 3\mu G$. Thus cosmic rays with energy above $10^{19}\,\mathrm{eV}$ can not be confined in the galactic disc whose thickness is $\sim 1.5\,\mathrm{kpc}$ and escape easily. There seems to be no correlation between the arrival directions of UHECRs and the galactic plane, so that it is natural to assume the origin of UHECRs as extra-galactic.
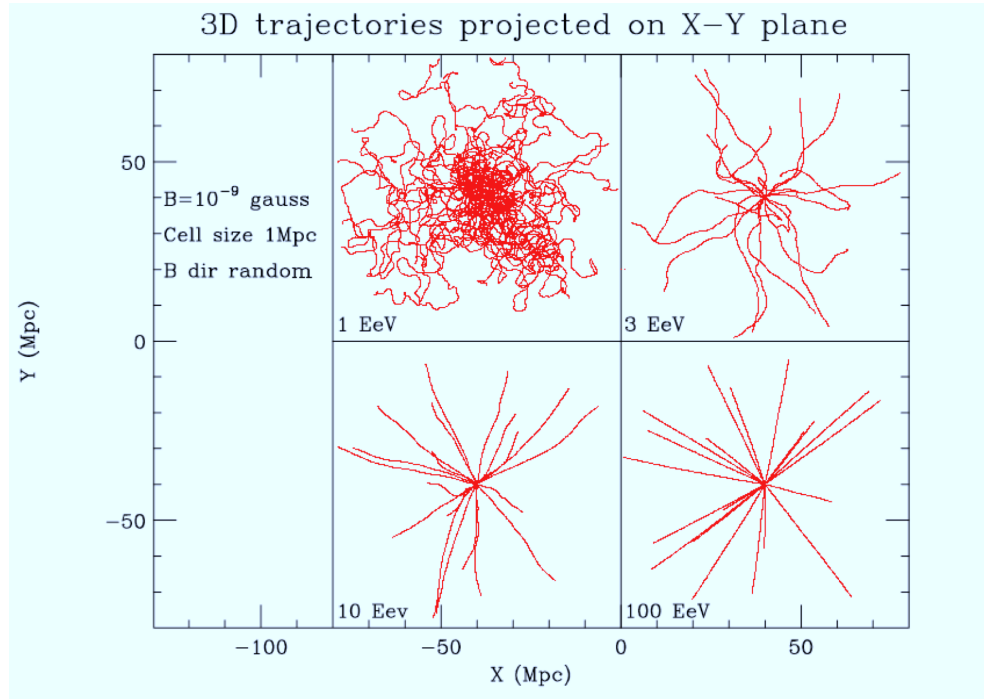

Figure 2.3: 20 trajectories of proton primaries emitted from a point source for energies of $1, 3, 10, 100\,\mathrm{EeV}$. The trajectories are followed until they reach a spatial distance of 40 Mpc from the source.

The strength of extra-galactic magnetic field is estimated $<< \mu G$ by the observation of Faraday rotation [50]. Figure 2.3 shows the simulated trajectories of the cosmic-ray propagation in the magnetic field of $\sim$ nG [26]. Cosmic rays with energy greater than 10^{20} eV can be point back to the point sources. However, in the case of cosmic rays with energy around 10^{19} eV, magnetic diffusion cannot be neglected. The deflection angle for a proton propagating a distance D in a magnetic field B with correlation length λ is given by [87]

$$\theta \simeq 0.025° \left(\frac{D}{\lambda}\right) \left(\frac{\lambda}{10\,\mathrm{Mpc}}\right) \left(\frac{B}{10^{-11}\,\mathrm{G}}\right) \left(\frac{E}{10^{20}\,\mathrm{eV}}\right), \qquad (2.5)$$

where E is the energy of a proton. When the magnetic scale is $10\,\mathrm{Mpc}$, the deflection angle propagated through the magnetic field of $\sim$ nG by a cosmic ray with energy of 10^{19} eV is $\sim 7°$.

Interaction with CMB photons

UHECRs interact with the CMB photons through pair creation and photopion production. When UHECRs collide with the CMB photons, and the center of mass energy exceeds the threshold energy of photopion production by Δ^+ resonance, UHECRs lose their energies rapidly through the interaction of $\gamma + p \rightarrow p + \pi^0, n + \pi^+$. Although below the energy of Δ^+ resonance, UHECRs also lose their energies by the pair production, $\gamma + p \rightarrow p + e^+ + e^-$. The attenuation length of protons by photopion production and pair creation is shown in Fig. 2.4 compared with that of iron [89]. Cosmic ray protons with energy above 10^{20} eV cannot reach the earth from the source greater than $100\,\mathrm{Mpc}$ away due to the interactions. The energy loss of the photopion production results in the cutoff of the cosmic-ray flux known as Greisen-Zatsepin-Kuzmin (GZK) cutoff [36, 91].

Figure 2.5 shows the modification factor which is an expected feature of energy spectrum, where all energy losses are taken into account [14]. The expected energy spectrum depends on the injection spectrum of sources. In the case of single source of UHECRs, it is expected that the energy spectrum shows the bump due to the pair creation. When UHECR sources are distributed uniformly, the bump feature

disappears and the dip appears alternatively. The dip feature does not shows the difference between the different index of injection spectrum shown in left Fig. 2.5. This means that the dip feature does not have a model dependence. However the dip feature appear for only pure proton model (see Fig. 2.5). If the mass composition is pure proton, the dip feature has a possible guide to calibrate the energy scale of spectrum.
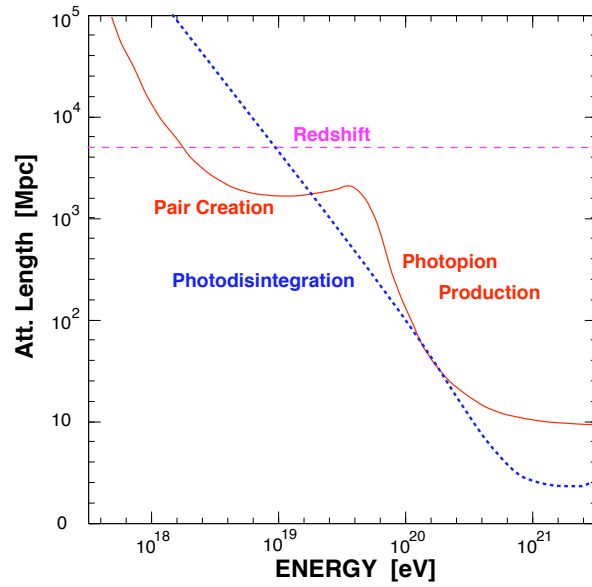

Figure 2.4: The attenuation length of cosmic rays as a function of energy. The solid curve shows the case of nucleons [90]. The dashed curve shows the case of iron [61].
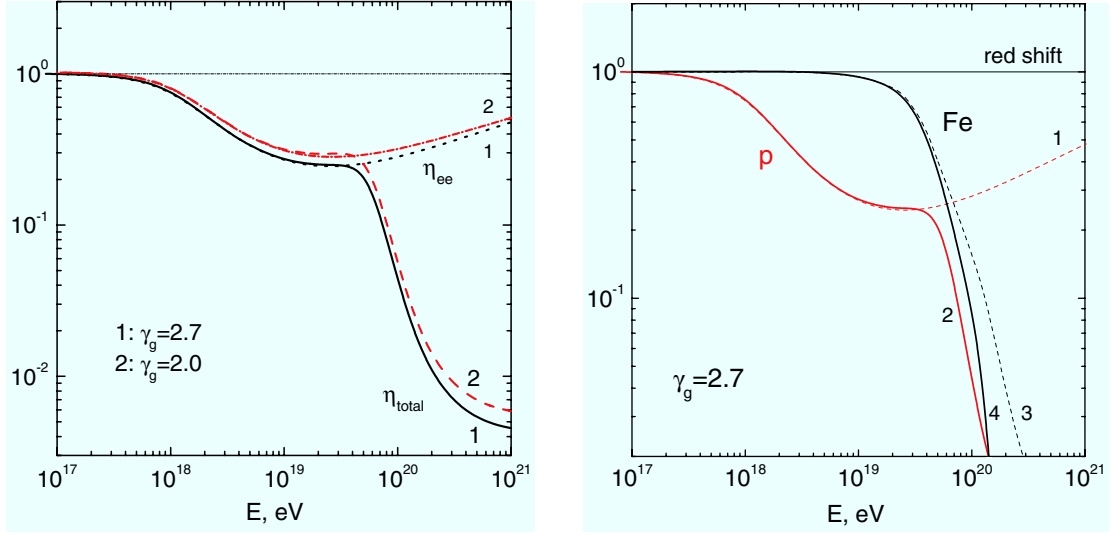
Figure 2.5: Modification factors for the power-law generation spectra with γ_g (left) and for pure proton or iron primary (right).

2.5.2   Acceleration up to UHE by Astronomical Objects

Cosmic rays are assumed to be accelerated by the plasma shock wave mainly. In order to accelerate cosmic rays up to some energy, the acceleration region should be larger than the Larmor radius of cosmic rays to confine them. Thus, the maximum energy depends on the size of the acceleration region. The relation between the maximum energy of acceleration $E_{\max}$ and the size of acceleration region L is given by simple equation,

$$E_{\max} \propto eZBL\beta c, \tag{2.6}$$

where βc is the velocity of the shock wave, eZ is the charge of accelerated particles and B is the strength of magnetic field. Figure 2.6, known as the Hillas plot [40], is the plot of candidates of astronomical objects which can accelerate cosmic rays up to some energies. As shown in Fig. 2.6, candidates which can accelerate cosmic rays up to 10^{20} eV are limited. Furthermore, these candidates should locate within 100 Mpc under the prediction of GZK effect. The mechanism of acceleration by these

astronomical objects, for example listed in the Fig. 2.6, is reviewed by Olinto well as following [56].
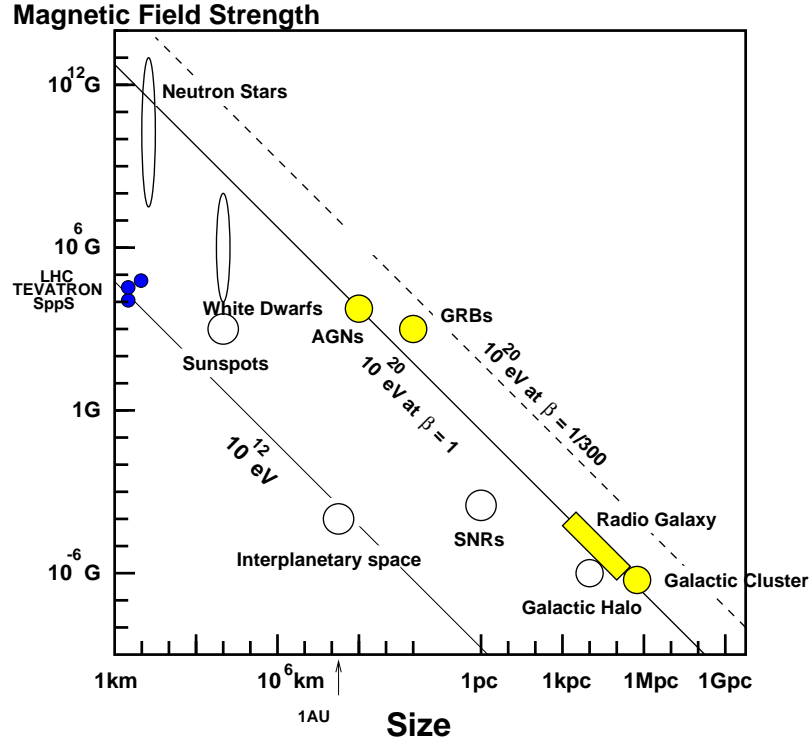

Figure 2.6: The Hillas plot which shows the relation between strength of magnetic field and scale of astronomical objects to accelerate up to some energies.

Cluster Shocks

Cluster shocks are reasonable acceleration sites up to UHECR, since E_{max} particles can be contained by cluster fields. However, high energy particles inside the cluster medium lose their significant energies when they escape. Up to $\sim 10\,\text{EeV}$, the shock around the Virgo Cluster may supply the UHECR flux [46].

AGN - Jets and Radio Lobes

Radio galaxies are one of the plausible astrophysical UHECR accelerators [40]. Jets from the central black holes of active galaxy end at a termination shock where the

interaction of the jet with the intergalactic medium forms radio lobes and hot spots. In those spots, particles are accelerated above $\sim$ EeV by the mechanism of the first-order Fermi acceleration [62]. The crossing of the tangential discontinuity between the relativistic jet and the surrounding medium may also be able to accelerate protons up to GZK region [58]. If we improve the observation statistics around GZK region, we may distinguish these models because of that the UHECR energy spectrum of latter model is flatter than the Fermi acceleration at the hot spots scenario. However, powerful AGNs with radio lobes or hot spots are rare and far apart. The closest possible object is M87 in the Virgo cluster which locates $\sim 18\,\mathrm{Mpc}$ away [12].

AGN - Central Regions

The central regions of active galaxies are possible engines for accelerator powered by the accretion of matters onto super massive black holes [40]. The nuclei of active galaxies can accelerate particles via a unipolar inductor. In the case of AGNs, the magnetic field is provided by the infalling matters and the spinning black hole horizon provides the imperfect conductor for the unipolar induction. However, in the central regions cosmic rays lose their energies due to the intense radiation field present in AGNs. Thus quasar remnants or super massive black halls in centers of inactive galaxies are raised as possible candidates [21].

Neutron Stars

Neutron stars with strong magnetic field of $\sim 10^{14}\,\mathrm{G}$, magnetars, are also possible astronomical accelerators [77]. In Fig. 2.6, the strength of magnetic field is enough to accelerate cosmic rays up to ultra-high energy. Cosmic rays can be accelerated in the light cylinder, power of that is mainly the rotational energy of magnetic breaking [83]. In general, the acceleration in a such region suffers from the significant energy loss. However, the plasma that expands beyond the light cylinder is free from the energy loss processes. When heavy nuclei such as iron are supposed as accelerated particles, they can be accelerated up to ultra-high energy in the relativistic Magneto-Hydro-Dynamics winds of young strongly magnetized neutron stars [20].

Gamma Ray Burst

Gamma Ray Bursts (GRBs) also can be candidates to accelerator of UHECRs. GRBs are distributed isotropically and the average rate of γ-ray energy emitted by GRBs is comparable to the energy generation rate of UHECRs with energy above 10^{19} eV, $\sim 10^{44}$ ergMpc^{-3}yr^{-1} [86]. The relativistic fireballs related to GRBs generate UHECRs with Fermi acceleration by internal shocks [84]. GRBs are required to locate within < 50 Mpc to avoid the GZK effect. However, the rate of GRBs is one burst per 100y. When GRBs are the source of UHECRs, we can see the correlation between the arrival direction of UHECRs and GRBs.

2.5.3 Possibility of New Physics

As the sources of UHECRs, various acceleration models by astronomical objects are proposed. However, there are no related objects reported identified as the sources. On the other hand, various models based on the new physics are proposed. Some of these are given as following.

Top Down Model

In order to avoid the problems to find possible astronomical accelerators up to ultra-high energy, it is natural to propose top down models which suggest that the sources have energy exceeding significantly the energy of UHECR originally. Such models are associated with grand unification theories (GUTs), supersymmetric grand unification theories (SUSY-GUTs) or superstring theories.

In the early stage of the big bang, cosmic strings, monopoles or topological defects (TDs) are supposed to be produced by the GUT phase transition when the strong and electroweak forces became separated. In top down models, UHECRs are generated due to the decay of TDs or super heavy relic particles (SHRPs) near our galaxy. TDs or SHRPs decay to higgs particles or super heavy fermions with GUT energy scale. As a result of the decay of these particles, jets are generated which consist of pions mainly. Hence, ultra-high energy gamma rays or neutrinos are generated [68].

Z-busts model is one of the expected Top down models [88]. UHE neutrinos with energy $\sim 10^{22}$eV are expected to produce UHE Z bosons by interaction with the 1.9K relic neutrino. Produced Z bosons immediately decay to $\pi^0, \pi^\pm$ and γ rays. When Z-bursts occur within a few tens of Mpc of the earth, these particles reach us and which can be observed as the super GZK events.

Lorentz Invariance Violation

In particle physics, Lorentz invariance (LI) might be broken at high energies by the idea of spontaneous symmetry breaking [65]. According to the breaking LI by a small first order perturbation in the electromagnetic Lagrangian, different particles can have different maximum attainable velocities which can be different from the speed of light [25]. Then, the interaction of protons with 2.7K CMB photons for pion production can be kinematically forbidden and photomeson interactions are turned off. The same case can occur for electron positron pair production. Thus, a very small amount of LI violation can turn off the photomeson and pair production interactions of UHECR with the CMB photons and eliminate the GZK cutoff.

2.5.4   Astronomical Origin or New Physics Scenarios

If UHECRs are produced by the astronomical objects, primary particles of UHECRs should be mainly nucleon, protons or heavier nucleon like irons. Moreover, due to the GZK effect, the accelerator should be located within at least 100Mpc. Thus, events of these are expected to be clustering near the directions of the sources.

On the other hand, new physics scenarios are related with ultra-high energy neutrinos or photons. Shower developments caused by UHE neutrinos incident on the earth become more deep and horizontal events can be expected. In the case of UHE photons, those are produced by the decay or annihilation of super heavy dark matter in the galactic halo and the distribution of arrival directions of those shows anisotropic. Top down model has also characteristic feature in energy spectrum, in which spectrum becomes harder than that of astronomical origin.

If Lorentz invariance violation occurs, in the energy spectrum, GZK cutoff and

dip of a pair production should be eliminated. However, this effect will be difficult to be concluded.

2.5.5 Energy Spectrum

The first observation of the UHECR with energy above 10^{20} eV was reported in 1963 [52]. UHECRs, thereafter, have been observed by various experiments, Haverah Park [51], Yakutsk [30], Fly's Eye [17], AGASA [73], HiRes [3, 1] and *etc.* In the twenty-first century, PAO and TA had started to observe UHECRs with hybrid detection technique. PAO reported the energy spectrum with the large exposure at the southern site [9].
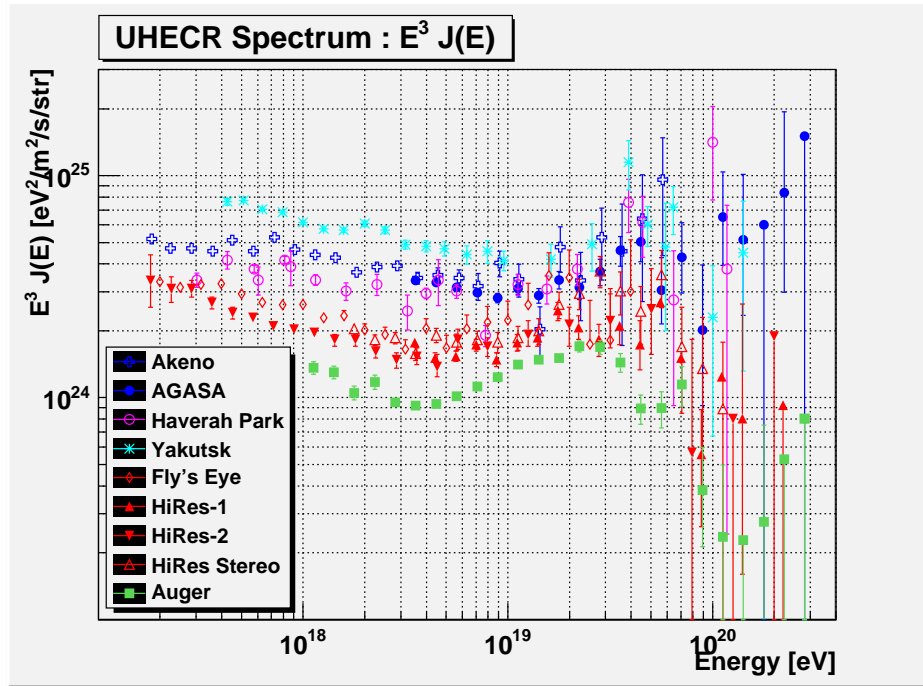
Figure 2.7: The energy spectrum of UHECRs observed by various experiment.

One of the reliable structure of UHECR spectrum is a hardening point, so-called "ankle". In the results of any experiments, such structure is shown. The "ankle" positions of each experiment are different, but the accuracies of energy determination of each are $\sim 20\%$. If it is possible to adjust the energy scale of energy spectrum

naively in the range of systematic errors, good agreement appears in "ankle" structure. However, the GZK cutoff is not the case.

The most attractive issue of UHECRs is the energy spectrum above 10^{19} eV. AGASA reported that 11 events above 10^{20} eV are observed which exceed the maximum energy predicted by the GZK mechanism [36, 91]. In Fig. 2.7, the energy spectrum observed by AGASA does not show suppression above the GZK cutoff. However, the energy spectrum reported by HiRes is consistent with the GZK cutoff. In the recent result reported by PAO, the energy spectrum is also consistent with the GZK suppression with much larger exposure. However, AGASA and HiRes are located in the northern hemisphere and PAO is located in the southern hemisphere. Thus, this result cannot conclude the contradiction between AGASA and HiRes.

2.5.6   Distribution of Arrival Directions

Figure 2.8 shows the distribution of arrival directions of 59 UHECR events observed by AGASA with energy above $10^{19.6}$ eV in the equatorial coordinate system [74]. This distribution is isotropic and does not correlated with the catalog of known astronomical objects. However, there are 6 doublet or triplet events which are 2 or 3 event set within the 2.5 degrees. The angular resolution of AGASA is 1.6°, thus these events can be considered that whose origins are the same.

On the other hand, PAO reported that the arrival directions of the UHECRs are correlated with the positions of relatively nearby active galactic nuclei shown in Fig. 2.9 [8]. The distribution is consistent with the extra-galactic model. Moreover, the correlation angular scale of a few degrees prefer the light component dominant in the flux of UHECRs or outside of our galaxy the magnetic fields are much weaker than expected.

2.5.7   Mass Composition

The energy spectrum or distribution of arrival directions are reported by various experiments as above. However, genuinely, in order to conclude these subjects, it is essential to clarify the mass composition of UHECRs.
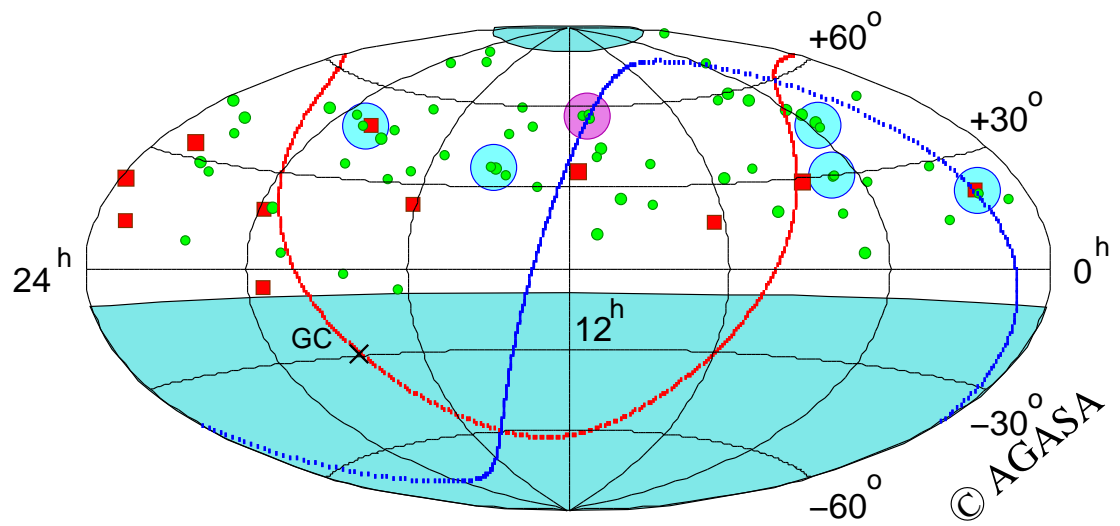
Figure 2.8: Arrival directions of cosmic rays with energies above 4×10^{19} eV observed by AGASA. Red squares and green circles represent cosmic rays with energies of above 10^{20} eV , and $(4-10) \times 10^{19}$ eV , respectively.
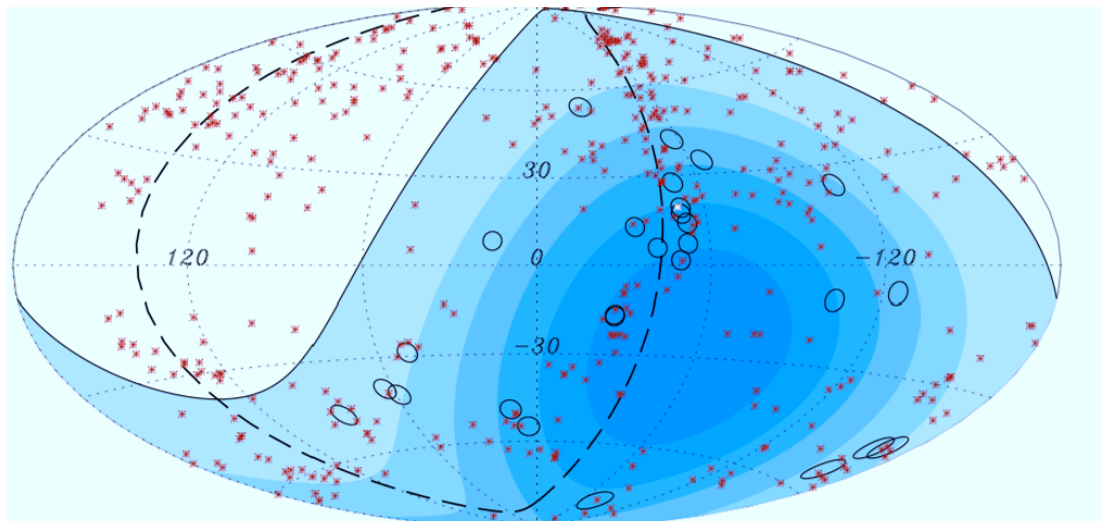

Figure 2.9: The circles of $3.2°$ are the cosmic rays with energy above 57EeV detected by PAO. The red points are positions of the AGNs within 71Mpc.

The fundamental questions of the sources of UHECRs can be constrained by the mass composition. The mechanism of acceleration up to such extremely high energy is still unknown. If the composition consists of nuclei such as protons or heavier, the astronomical origin is favored. In particular, the heavier dominated composition such as iron supports the model of acceleration by a neutron star with strong magnetic field. On the other hand, the flux of UHECRs contains the UHE photons, new physic such as Top down models can be possible.

In the case of the energy spectrum of UHECRs, there are mainly two interpretation of "ankle" structure. One is the transition from the galactic to extra-galactic model [13]. In this model, mixed composition is assumed, where CNO or Fe nuclei are several times more than the standard composition. The mixed composition model can explain the energy spectrum at the energy above $10^{18.5}$ or 10^{19} eV by only the extra-galactic component. Another plausible model is the pure proton model, in which the dip structure produced by pair creation of electron positron through the interaction with the CMB photons. According to the model, the flux of cosmic rays with energy above 10^{18} eV consists of only proton and the structure of "ankle" is contained in the energy region as dip. If the origin of "ankle" is the pair creation, the position of that can be utilized for the energy calibration.

Not only for the energy spectrum but also for the distribution of arrival directions, the mass composition of UHECRs can be crucial point. The distribution of the arrival directions from the same source should be diffused due to the interaction with the magnetic field. The larger the charge of cosmic rays, the scale of diffusion should become larger. The correlation with nearby AGNs reported by PAO suggests that the flux of UHECRs are dominated by light component.

Fly's Eye, HiRes and PAO reported the composition of UHECRs by the $X_{\max}$ technique [18][2][7]. $X_{\max}$ is the atmospheric depth where the number of shower particles reaches maximum. The left of Fig. 2.10 and Fig. 2.11 are the average $X_{\max}$. The average $X_{\max}$ observed by HiRes prefers the proton-dominated composition at energies above $10^{18.2}$ eV based on the analysis with QGSJET-01 and QGSJET-II. On the other hand, PAO observation implies that the UHECRs contain a large fraction of heavy or intermediate mass nuclei especially at the highest energies. The right of
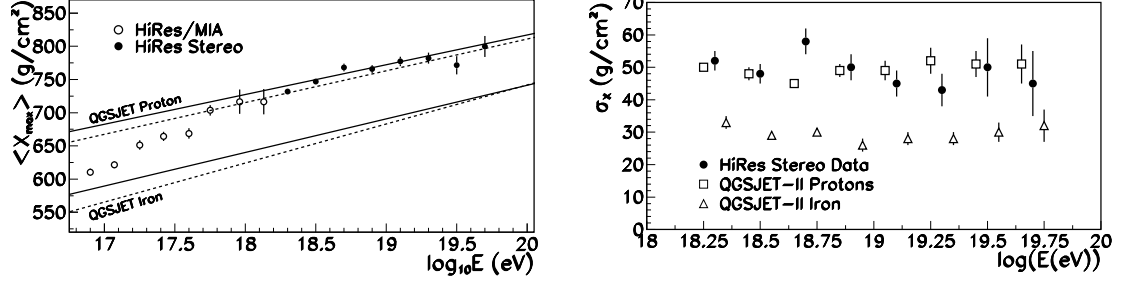
Figure 2.10: The average $X_{\max}$ and the RMS of $X_{\max}$ observed by HiRes compared with the air shower simulations with hadronic interaction model, QGSJET.
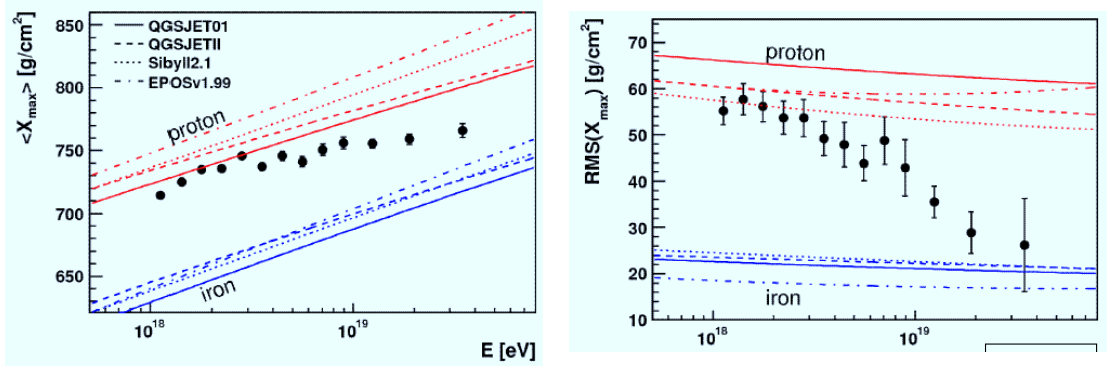

Figure 2.11: The average $X_{\max}$ and the RMS of $X_{\max}$ observed by PAO compared with the air shower simulations with hadronic interaction model, QGSJET, SIBYLL and EPOS.

Fig. 2.10 and Fig. 2.11 are the RMS of $X_{\max}$. In the case of HiRes, RMS($X_{\max}$) also back up the proton-dominated composition with good agreement. Furthermore, RMS($X_{\max}$) of PAO is getting smaller. This implies the flux of UHECRs contains little or no protons at the highest energy.

PAO also studies the mass composition with the surface detectors using the new parameter of the maximum of asymmetry. In this technique, the asymmetry of the arrival timing of shower particles is used and the maximum of that is also good parameter to identify the primary species [28]. This result also prefers the heavy component, consistent with $X_{\max}$ measurements. However, it is important that the

heavy dominant composition which is not consistent with the correlation of arrival directions with nearby AGNs observed by the same experiments.

In Fig. 2.12, average $X_{\max}$ of various experiments above the energy of 10^{14} eV are plotted together with UHE region, Yakutsk [70], CASA-BLANCA [33], SPASE [27], CACTI [59] and DICE [22]. In these experiments, $X_{\max}$ is observed by the Cherenkov light detection. From the slope of lateral distribution of the Cherenkov light, $X_{\max}$ can be determined. Above the "knee" region, the trend of mass composition getting from light component to heavy component is simply interpreted as a result of the diffusive shock acceleration, in which the positions of the "knee" of each component shift in proportion to the charge of the primaries [60]. The leakage box model also one of the plausible models of composition change, due to the rigidity dependence of the cosmic-ray propagation [24]. Thus, above the "knee" region to 10^{17} eV, the composition is getting heavier and mainly the galactic component. Above the 10^{17} eV, the transition from the galactic to extra-galactic component seems to be observed.
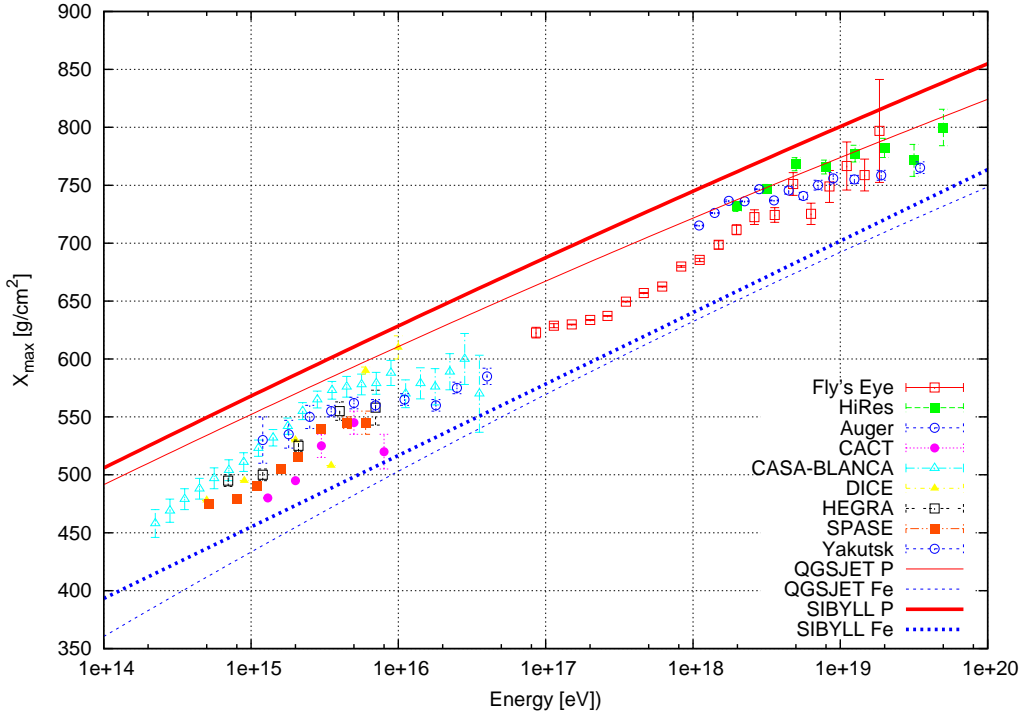
Figure 2.12: The average $X_{\max}$ observed by various experiments.

Chapter 3

Cosmic Ray Air Shower

An air shower is a cascade of particles caused by the interaction of a primary cosmic ray nucleus or photon at the top of atmosphere. The observed cosmic-ray energy is from 10^7 to 10^{20} eV. Cosmic rays with energy below 10^{14} eV can be measured directly by balloons or space experiments. On the other hand, high energy cosmic rays flux is proportional to the E^{-3} and direct measurement is not practical due to the demand for the large detection area and long exposure. Therefore cosmic rays with energy above 10^{14} eV measured indirectly to observe the cosmic-ray air shower particles which spread in wide area.

3.1 Air Shower Cascade

Primary cosmic-ray particles incident on the atmosphere interact with nucleus and generate secondary particles. Moreover, the secondary particles generate secondary particles. Air shower phenomenon is a result of these processes to generate huge number of particles. Figure 3.1 is a conceptual sketch of an air shower phenomenon.

3.1.1 Nucleonic Cascades

Primary cosmic ray hadron such as proton or nucleus produces secondary particles (mesons) passing through the atmosphere. The mainly produced particles are pions,
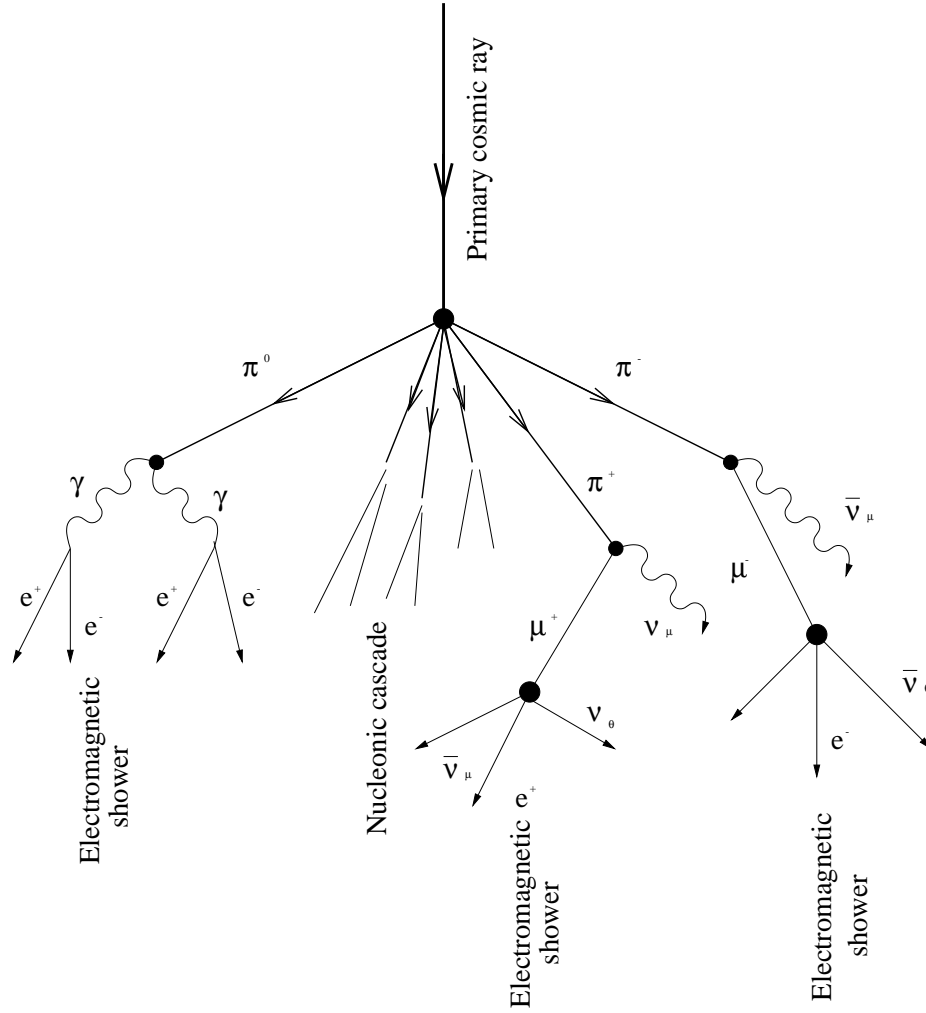
Figure 3.1: Conceptual sketch of air shower cascade.

which occur in three pions, π^+, π^- and π^0. Kaons and baryon-antibaryon pairs are also produced, if the energy is high enough but much smaller number.

The neutral pions undergo electromagnetic decay, $\pi^0 \rightarrow 2\gamma$, with an extremely short lifetime of 8×10^{-17} s. The photos from the decay develop electromagnetic cascade.

The charged pions decay to muons and neutrinos with a lifetime of 2.6×10^{-8} s,

$$\pi^{\pm} \rightarrow \mu^{\pm} + \nu_{\mu}. \tag{3.1}$$

The charged kaons also decay to muons or pions as following decay,

$$K^{\pm} \rightarrow \mu^{\pm} + \nu_{\mu},$$
$$\rightarrow \pi^{\pm} + \pi^{0}. \tag{3.2}$$

The branching fractions for the dominant decay modes of the kaons are 63.5% and 21.2% respectively.

The generated muons are also unstable and decay to electrons and neutrinos with a life time 2.2×10^{-6}s,

$$\mu^{+} \rightarrow e^{+} + \bar{\nu}_{\mu} + \nu_{e},$$
$$\mu^{-} \rightarrow e^{-} + \nu_{\mu} + \bar{\nu}_{e}. \tag{3.3}$$

3.1.2 Electromagnetic Cascades

High energy gamma rays produced by the decay of π^{0} cause pair creation to produce the electrons and positrons. The electrons and positrons generate high energy photons by bremsstrahlung. These charged particles also lose their energies by ionization in a medium.

Pair Production Photons interact through the three processes: photo-electric effects, Compton effect and pair production. Photo-electric effects and Compton effect should be taken into account at low energies below $\sim$ a few tens of MeV. Thus, these two processes can be neglected for high energy photons in the electromagnetic cascade.

Pair production is the process by the interaction between the high energy photon and the Coulomb field of the nucleus. The photon decays to electron and positron by this interaction. This process can occur only at energies higher than the rest masses of the electron and the positron. The differential probability per radiation length of air that a photon of energy E_0 creates an electron positron pair, one of which has an

energy $E = vE_0$ is ,

$$\psi_{\text{pair}}(v) \quad = \quad 1 - (\frac{4}{3} + 2b)v(1 - v), \tag{3.4}$$

where

$$b \quad = \quad \frac{1}{18\ln(183Z^{-1/3})} \tag{3.5}$$

and has a value of 0.0122 for air ($Z = 7.5$). The radiation length, X_0, is defined as

$$\frac{1}{X_0} \quad = \quad 4\alpha\frac{N}{A}Z(Z+1)r_e^2\ln(183Z^{-1/3})/\left[1 + 0.12\left(\frac{Z}{82}\right)^2\right], \tag{3.6}$$

where $\alpha = \frac{1}{137}$ is the fine structure constant. X_0 is 37.7 g/cm^2 in air. The pair creation probability is independent of the energy of the photons and depends only on the fraction of energy v taken by one of the pair.

Ionization   An electron or a positron in a medium lose their energy due to ionization and the energy loss is given by

$$\frac{dE}{dx} \quad = \quad -2\pi N\frac{Z}{A}r_e^2 m_e\left[\ln\left(\frac{\pi^2 m_e^2}{(1-\beta^2)^{3/2}I^2(Z)} - a\right)\right], \tag{3.7}$$

where $\beta = v/c$ the velocity of the electron, $I(Z)$ is the average ionization potential in eV of an atom of the medium with atomic number Z. $I(Z)$ for air is 80.5eV. The constant $a = 2.0$ for electrons and 3.6 for positrons.

Bremsstrahlung   Bremsstrahlung is the process by which a high energy electron emits a photon when it interacts with the electromagnetic field of the nucleus in the medium. The differential probability per radiation length of air that an electron or a positron of energy E emits a photon of energy vE is

$$\psi_{\text{brems}}(v) \quad = \quad v - (\frac{4}{3} + 2b)\frac{(1 - v)}{v}, \tag{3.8}$$

where b is given by Eq. 3.4. Integrating Eq. 3.4, the energy loss per radiation length as

$$\frac{1}{E}\frac{dE}{dx} = 1 + b \approx 1, \tag{3.9}$$

where x is the thickness of the medium measured in radiation lengths. The energy loss is proportional to the energy.

The energy loss at which radiation losses and collision loss are equal and has a value of 84.2MeV in air is called critical energy, ε_0. In the cascade, the number of particles grows exponentially and decreases after energies of cascade particles reach below the critical energy due to the energy loss.

3.2 Longitudinal Development

Shower particles lose their energy as the number of shower particles grow due to the processes mainly pair production and bremsstrahlung. The energies reach the critical energy, ε_0, and ionization process with nuclei or molecules in air become dominant. Thus, shower particles lose their energies rapidly and are absorbed in air and the number of shower particles turn to decrease. Such as the change of the number of shower particles pass through the medium is called as longitudinal development.

The longitudinal development induced by an electron with energy E_0, as a function of depth X, is given by

$$N_e(X) \sim \frac{0.31}{\sqrt{y}} \exp\left[X\left(1 - \frac{3}{2}\ln s\right)\right], \tag{3.10}$$

where $s \simeq 3t/(X + 2y)$ and $y = \ln(E_0/\varepsilon)$. This shower development includes only the electromagnetic component. Air showers induced by most of cosmic rays such as protons or nuclei, hadron component should be taken into account. However, it is well known that the cosmic ray air shower can be approximated as the superposition of the electromagnetic cascade. The famous approximation equation of shower particles

at the given atmospheric depth, Gaisser-Hillas (G-H) function [34], is given as

$$N(X) \; = \; N_{\max} \left(\frac{X - X_0}{X_{\max} - X_0} \right)^{\frac{X_{\max} - X_0}{X}} \exp \left(\frac{X_{\max} - X}{\lambda} \right). \qquad (3.11)$$

where X_0 is the point of the first interaction, $X_{\max}$ is the depth at which the number of electrons reaches maximum and $\lambda = 70 \, \mathrm{g/cm^2}$.

Figure 3.2 shows the comparison of the simulated shower development induced by various primaries and energies. Profiles of shower developments strongly depend on the primary particle type and energy. When the primary energy is determined, we can know the primary particle type. However, individual shower profile also shows the large fluctuation, thus composition study is forced to be achieved in statistical way.
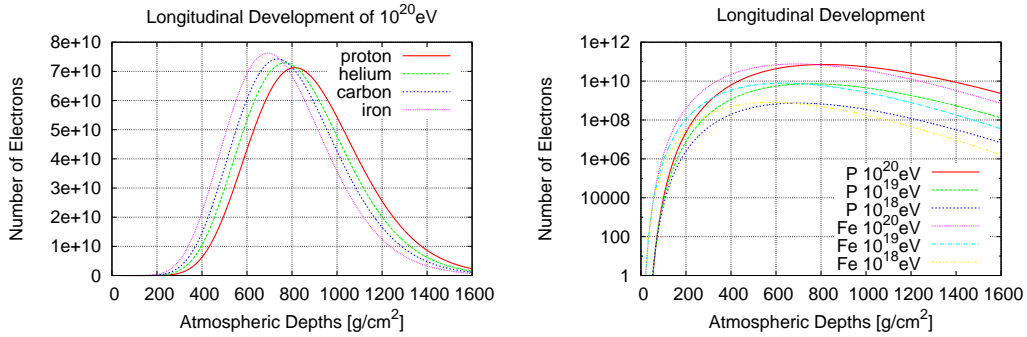
Figure 3.2: Simulated shower developments. Left: primaries are proton, helium, carbon and iron of 10^{20} eV. Right: primary energies are $10^{18,19,20}$ eV of proton or iron.

3.3   Lateral Distribution

The distribution of the shower particles in a plane perpendicular to the shower axis at a given depth is the lateral distribution shown in Fig. 3.14. The lateral distribution is calculated from electromagnetic cascade theory using the function calculated by

Nishimura, Kamata and Greisen [45, 41] known as NKG function represented by

$$f(r, s) \; = \; C(s) \left(\frac{r}{r_{\mathrm{M}}}\right)^{s-2} \left(\frac{r}{r_{\mathrm{M}}} + 1\right)^{s-4.5} \tag{3.12}$$

$$\rho(r, s) \; = \; \frac{N_e f(r, s)}{r_{\mathrm{M}}^2} \tag{3.13}$$

where r is the distance from shower axis, r_{M} is the Moliere unit, $C(s)$ is normalization factor, N_e is the number of electrons and s is the age parameter. The age parameter is empirically given by

$$s \; = \; \frac{3}{1 + 2X_{\max}/X}. \tag{3.14}$$

The age parameter become 1 at the shower maximum. Figure 3.2 shows the lateral distribution by NKG function at shower age, $s = 1$.
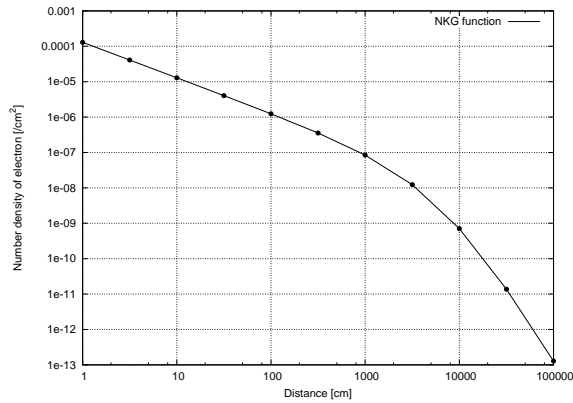
Figure 3.3: Lateral structure of electron number density in air shower whose primary is proton with energy 10^{19} eV at shower maximum.

3.4   Light Emission by the Shower Particles

Shower particles cause various light emissions in the atmosphere. The refractive index of air is greater than 1, so that electrons or protons in air showers emit the Cherenkov light. Moreover, the fluorescence emission is caused by excited nitrogen molecules exited by shower particles. The amount of light of Cherenkov and fluorescence emission are comparable. On the other hand, fluorescence light emitted isotropic, and Cherenkov emission has directional feature along the momentum direction of particles. Detection of these emission caused by shower particle enable to observe the shower development directory.

3.4.1   Cherenkov Radiation

When the velocity of charged particles become faster than the speed of light in the vacuum, particles emit the Cherenkov radiation. The reflective index of air is more than 1, so that air shower particles emit Cherenkov light in the atmosphere. The criteria of Cherenkov emission for charged particles is give as

$$n\beta > 1.0, \tag{3.15}$$

where $\beta = \frac{v}{c}$, v is the velocity of particles. Cherenkov light is a shock wave when velocity of particles exceed the light speed, the shock front is formed as a cone shape. The angle θ_c of Cherenkov light to the momentum direction of particles is given by

$$cos\theta_c \quad = \quad \frac{1}{n\beta}. \tag{3.16}$$

Particles lose their energies by Cherenkov radiation. When charged particles travel dL, the energy loss dW of Cherenkov radiation is

$$\frac{dW}{dL} \quad = \quad \frac{Z^2 e^2}{4\pi\varepsilon_0 c^2} \int \left(1 - \frac{1}{n^2\beta^2}\right) \omega d\omega, \tag{3.17}$$

where ω is a frequency of Cherenkov light, Ze is a charge of particles, ε_0 is the dielectric constant in vacuum and n is a refractive index of medium. The number of

photons emitted with the wave length λ is

$$
\begin{aligned}
\frac{d^2 N}{dl d\lambda} &= \frac{2\pi\alpha Z^2}{\lambda^2}\left(1 - \frac{1}{n^2\beta^2}\right) \\
&= \frac{2\pi\alpha Z^2}{\lambda^2}\sin^2\theta_c,
\end{aligned}
\tag{3.18}
$$

where, $\alpha = e^2/4\pi\varepsilon_0\hbar c = 1/137$ is the fine structure constant. The refractive index is approximated as

$$
\begin{aligned}
n &= 1.0 + \delta \\
\delta &= 0.000296 \times \frac{X}{1030[\mathrm{g/cm^2}]}\frac{273.2[\mathrm{K}]}{T}
\end{aligned}
\tag{3.19}
$$

where, n is the refractive index of atmosphere, $X\mathrm{g/cm^2}$ is the atmospheric depth and T is temperature [39].

The X_{max} of protons of primary energy $10^{19}\,\mathrm{eV}$ is simulated as $750\,\mathrm{g/cm^2}$ where the altitude is $2,600\,\mathrm{m}$ and the refractive index is 1.00022, thus the threshold energy to emit the Cherenkov light by air shower particles is about $24\,\mathrm{MeV}$ from Eq. 3.16.

According to the calculation by Nerling [54], the energy distribution of air shower particles is given by

$$
f_e(E,s) = a_0\frac{E}{(E+a_1)(E+a_1)^s},
\tag{3.20}
$$

where s is age parameter(Eq. 3.14). CORSIKA is one of the most popular simulation code of cosmic-ray air showers. Each parameter, a_0, a_1, a_2, depends on the hadron and electron threshold energy in CORSIKA. The number of electrons which emit the Cherenkov light can be estimated by this distribution.

The shower particle momenta are distributed along that of primary particle, so that angular distribution of Cherenkov light follows this. The angular distribution of Cherenkov light is given by

$$
A_\gamma(\theta,h,s) = a_s(s)\frac{1}{\theta_c(h)}e^{-\theta/\theta_c(h)} + b_s(s) \times \frac{1}{\theta_{cc}(h)}e^{-\theta/\theta_{cc}(h)}.
\tag{3.21}
$$

3.4.2   Air Fluorescence Emission

When high energy charged particles in the air shower pass through the atmosphere, they ionize and excite the nitrogen molecules. The excited nitrogen molecules emit fluorescence light due to de-excitation.

The wave band of fluorescence emission from nitrogen molecule is mainly $300 \sim 400 \, \mathrm{nm}$. The fluorescence spectrum of molecular nitrogen is a band spectrum due to their variety of broad bands in contrast to atomic line spectra. This band structure is caused by the vibration and rotational movements of the molecular nuclei. Energy of molecular states are expressed as the sum of three energy state,

$$E = E_{\mathrm{el}} + E_{\mathrm{vib}} + E_{\mathrm{rot}}, \tag{3.22}$$

where E_{el} is the potential electron energy of a static molecule and E_{vib} and E_{rot} are of vibrations and rotations of the molecular nuclei. There is a relation between three contribution as

$$E_{\mathrm{el}} : E_{\mathrm{vib}} : E_{\mathrm{rot}} = 1 : \sqrt{\frac{m}{M}} : \frac{m}{M}, \tag{3.23}$$

where m is the electron mass and M is the molecular nuclei mass. Thus, the difference of state by rotation is quite small.

The atmospheric fluorescence mechanism is mainly the transition from neutral nitrogen molecule to the second positive$(2P)$ system and from nitrogen ion to the first negative$(1N)$ system.

$$2\mathrm{Psystem} : \mathrm{C}^3\mathrm{II_u}(\nu^{'}) \rightarrow \mathrm{B}^3\mathrm{II_g}(\nu^{''})$$
$$1\mathrm{Nsystem} : \mathrm{B}^2\mathrm{II_u^+}(\nu^{'}) \rightarrow \mathrm{X}^2\mathrm{II_g^+}(\nu^{''}) \tag{3.24}$$
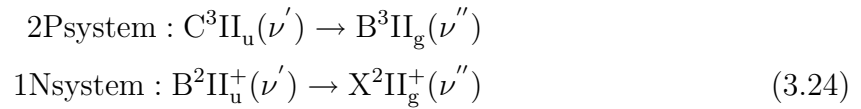
where, $\nu^{'}, \nu^{''}$ are the first and the last state of vibration. General decay law is given by

$$\frac{dN_{\nu'}}{dt} = -\left(\lambda_{\mathrm{rest}} + \sum \nu'' A_{\nu',\nu''} \right). \tag{3.25}$$

Quenching, radiationless deactivation, process is also effective to estimate the amount of fluorescence light. Quenching process is energy transfer via the collision with other molecule and strongly depends on the number density (pressure) and velocity (temperature).

The fluorescence yield are measured by many experiments [23] [43] [53] [15] [6] [85]. Figure 3.4 shows the fluorescence spectrum measured by Bunner. The wavelength of fluorescence emission are mainly ultraviolet. Figure 3.5 is the comparison of the number of fluorescence photons per energy deposit.
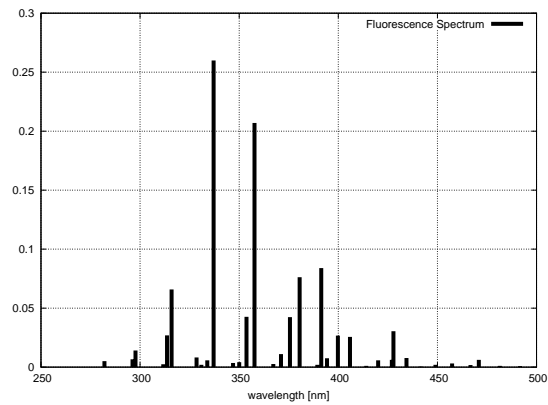
Figure 3.4: The spectrum of fluorescence emission in the air.
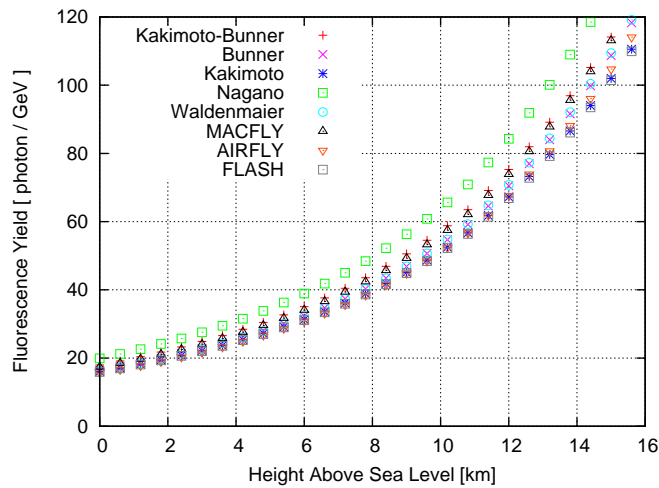
Figure 3.5: The fluorescence yield measured by various experiments.

3.5 Air Shower Detection: Fluorescence Technique

3.5.1 Detector General

The fluorescence technique had originally suggested by Greisen [35] or Suga [69]; the fluorescence light emitted by exited nitrogen molecule along the shower axis is detected for the measurements of air showers. The number of fluorescence photons are proportional to the energy deposit in the air. Thus, this is a one of the advantage to be able to estimate the primary energy calorimetric. Detection of fluorescence photons along the shower axis is the direct measurement of shower development, hence this can be powerful strategy to study primary particle type. The schematic view of fluorescence detection is shown in Fig. 3.6. The number of photons detected at the telescope is given by

$$\frac{dN_\gamma}{dx} = \frac{dE_{\text{deposit}}}{dx} \cdot \sum_\lambda \cdot Y_\lambda(p,T) \cdot T_{\text{atm}}(\lambda,x) \cdot \varepsilon_{\text{det}}(\lambda,x) \qquad (3.26)$$

where, dE_{deposit} is the energy deposit of the charged particles in an air shower at given atmospheric depth, Y_λ is the fluorescence yield as a function of pressure, p, and temperature, T, T_{atm} is the transparency of the atmosphere and ε_{det} is the detector efficiency. There is an uncertainty of atmospheric fluorescence yield of $15 \sim 30\,\%$, although many experiments measured. At the Telescope Array observatory, on site calibration is planed to measure the fluorescence yield of actual air to inject the electron beam with energy $40\,\text{MeV}$ from the linear accelerator in front of the telescopes [67].

The Fly's Eye experiment [16] is the pioneer to progress the fluorescence technique to detect air showers. In general, a fluorescence detector is a telescope consisting of large exposure mirror system and photon sensors cluster. The number of fluorescence photons at the detector is much small and wavelength of fluorescence light is almost ultraviolet, thus sensitive photon sensor such as photomultiplier tubes are adopted. Moreover, there are many background photons such as star light, therefore UV filter

also used.
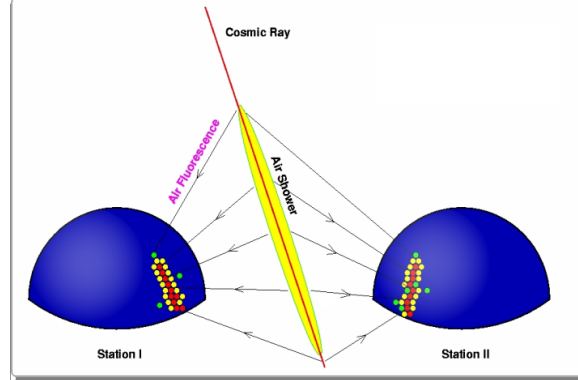
Figure 3.6: The concept of fluorescence technique. In particular, detection by two separated detectors is stereoscopic observation which improve the geometry reconstruction.

3.5.2 Rayleigh Scattering

The number of fluorescence photons from the shower axis are scattered and attenuated by the atmosphere. Thus, in order to estimate the number of photons on the axis, atmospheric profile, $T_{\mathrm{atm}}(\lambda, x)$ in the Eq. 3.26, is quite important. The atmospheric attenuation process are mainly Rayleigh and Mie scattering.

The Rayleigh scattering is elastic scattering process of light when the size of scattering particles is much less than the wavelength. Because of the scattering by atmospheric molecules, the sky looks blue. This process can be considered as the scattering between the photons and electrons in the atom and the cross section is given by

$$\sigma_{\mathrm{tot}} \;=\; \int \sigma(\theta) d\Omega = \sigma_{\mathrm{T}} \left(\frac{\lambda_0}{\lambda} \right)^4 \qquad (3.27)$$

where σ_{T} is the cross section of Thomson scattering. The cross section of Rayleigh scattering is proportional to λ^{-4}.

The ratio of the intensity of injection to that of traveling light is given by

$$\begin{aligned}
\frac{I}{I_0} &= \exp(-\gamma r) \\
\gamma &= \sigma_{\mathrm{T}} \left(\frac{\lambda_0}{\lambda}\right)^4 N
\end{aligned} \tag{3.28}$$

where r is the path length of light, N is the number density and γ^{-1} is the attenuation length (γ is called as the extinction coefficient).

3.5.3   Mie Scattering

Mie scattering is the scattering by aerosols or dusts in the atmosphere when the order of those are similar or little larger than the wavelength of visible light. The transmission of Mie scattering T_{Mie} is approximated by

$$\begin{aligned}
hd_{\mathrm{eff}} &= hd - (h_{\mathrm{det}} - h_{\mathrm{hill}}) \\
t &= \left(e^{-\frac{hv_{\mathrm{eff}}}{h_{\mathrm{m}}}} - e^{-\frac{hd_{\mathrm{eff}}}{h_{\mathrm{m}}}}\right) \frac{h_{\mathrm{m}}}{l_{\mathrm{m}} \cdot \cos\theta} \left(1 - \frac{h_{\mathrm{m}} \cdot \tan\theta}{R}\right) \\
&\quad - \frac{h_{\mathrm{m}} \cdot \tan\theta}{R \cdot l_{\mathrm{m}} \cdot \cos\theta} \left(hv_{\mathrm{eff}} \cdot e^{-\frac{hv_{\mathrm{eff}}}{h_{\mathrm{m}}}} - hd_{\mathrm{eff}} \cdot e^{-\frac{hd_{\mathrm{eff}}}{h_{\mathrm{m}}}}\right) \\
t_{\mathrm{Mie}} &= e^t,
\end{aligned} \tag{3.29}$$

where h_{m} is the scale height of aerosol distribution, l_{m} is the mean free path of Mie scattering, R is the radius of the earth and Fig. 3.7 shows the other variables.

In the case of phase function, the Rayleigh scattering is symmetrical, on the contrary, the Mie scattering is mainly forward scattering.
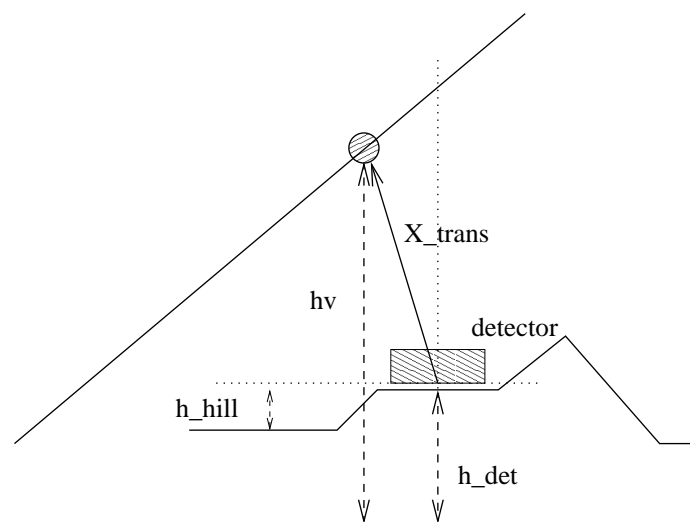
Figure 3.7: Parameters for Eq. 3.29

Chapter 4

Telescope Array Experiment

The Telescope Array (TA) collaboration has started operation of a large scintillation Surface Detector (SD) array and three Fluorescence Detector (FD) stations [47]. The TA observatory is located in Millard county, Utah, USA ($39.1° \mathrm{N}$, $112.9° \mathrm{W}$). Figure 4.1 shows the detector configuration of TA experiment. There are 512 scintillation counters arranged in a grid of 1.2 km spacing which cover the area of $678 \, \mathrm{km}^2$, and three FD stations whose field of view (FOV) covers over the SD array. The goal is to clarify the origin and astrophysics of UHECRs, with both air shower detection techniques, one of them is particle detection by the plastic scintillation counters array at the ground which is the same type of AGASA and another is the fluorescence detection by the telescopes array which is the same type of HiRes. As the same purpose, the Pierre Auger Observatory [10], located in Argentina, had started operation with water Cherenkov detectors array and fluorescence detectors.

One advantage of the TA experiment is that the TA site is located in the northern hemisphere, where the effects of the galactic magnetic field on the trajectories of UHECRs is smaller than in the case for the southern hemisphere [72]. Additionally, the Telescope Array has the same view of the sky as the HiRes experiment and it has a large overlap with the view of AGASA. Therefore, by tracing the arrival directions back to original sources of the UHECRs, we can investigate the anisotropy as reported by AGASA [75, 80] and HiRes [4, 5], with improved angular accuracy.
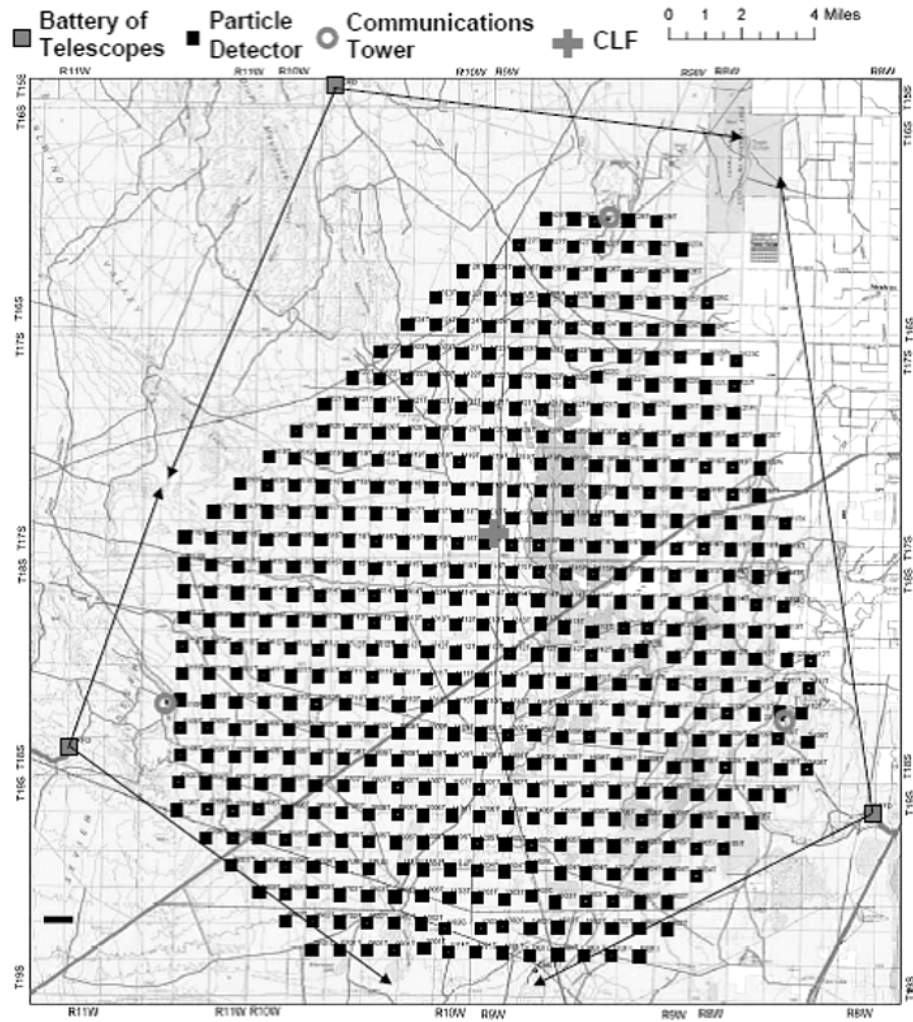
Figure 4.1: The detector configuration of the TA. Black square: particle detector, Gray: square Fluorescence detector station, Circle: Communication tower, Cross on the center of the map: Central laser facility. Arrows represent the edge of the field of view of FDs.

4.1   Fluorescence Detector

In the TA site, there are three FD stations surrounding the surface detector array. The southern two stations contain the twelve newly developed FD telescopes for Telescope Array Experiment each. The FOV of the FD is $15°$ in azimuthal and $16°$ in elevation angle. In the FD station, FD telescopes are arranged in 2 by 6 matrix. The FOV of the each station is $108°$ in azimuthal and $3 - 33°$ covering the SD array. The FD telescope consists of the spherical mirror with diameter of 3.3m and PMT camera (see Fig. 4.3). More details are described in following sections.

HiRes-I was transferred to rest of the northern station at the Middle Drum (MD). There are fourteen FD telescopes each consisting of a spherical mirror of 2m diameter and a PMT (Photomultiplier Tube) cluster at the focal plane. The effective mirror area is $3.75\,\mathrm{m}^2$ and the curvature radius is 4.74m. The FOV is $16.5°$ in azimuth and $16°$ in zenith. For the HiRes-I electronics, sample and hold system is applied [11].

Figure 4.2: The left figure is the FD station at Black Rock Mesa (BRM) which contains 12 fluorescence telescopes. The right figure is the FD station at Middle Drum and transferred HiRes-I mirror units.

4.1.1   The Telescope and Optics

One TA FD station consists of twelve telescopes. The FOV of one telescope is $18.0°$ in azimuth and $15.5°$ in elevation. The upper layer composed of 6 telescopes covers the entire azimuthal angle and the elevation angle of $3° \sim 18.5°$. The lower layer covers $18.5° \sim 34°$ in elevation.
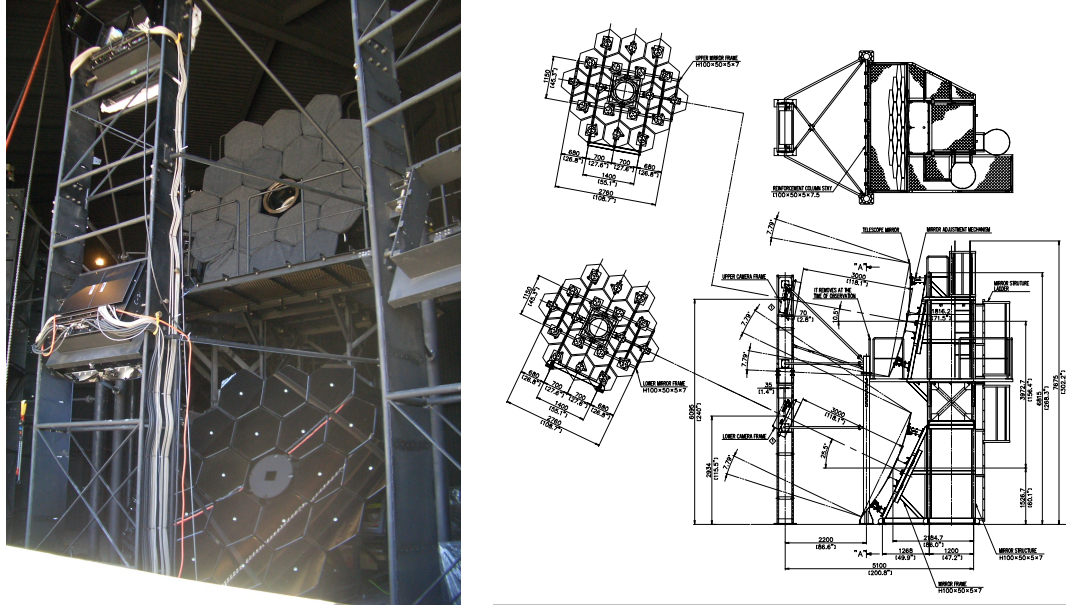
Figure 4.3: The newly developed telescopes and that of design. The mirrors of upper telescope are covered to prevent dusts.

We use a spherical mirror optics to obtain a wide FOV with reasonable focusing power. The support and adjustment mechanism for the segmented mirror is also simpler for the spherical mirror compared with the parabolic system. According to the ray tracing simulation, the spot size of 30 mm at the focal plane is obtained in most of the FOV (Fig. 4.4) when the spot sizes of each mirror at the curvature center is within the 20 mm. For all of the mirror, we measured the curvature radius and spot size at the curvature center before installing.

The telescope has a spherical mirror with a diameter of 3.3 m which is composed of 18 hexagonal shape segment mirrors. The total mirror area is 6.8 m^2. The curvature radius of each mirror is 6067 mm and the focal length is 2960 mm. The attachment angle of each mirror is adjustable in two directions. The location of the central mirror is made empty and is reserved for the optical alignment system or Xe flash lump for the PMT calibration during the observation.

Design of the segment mirror is shown in Fig. 4.5. The mirror is made by 10.5 mm
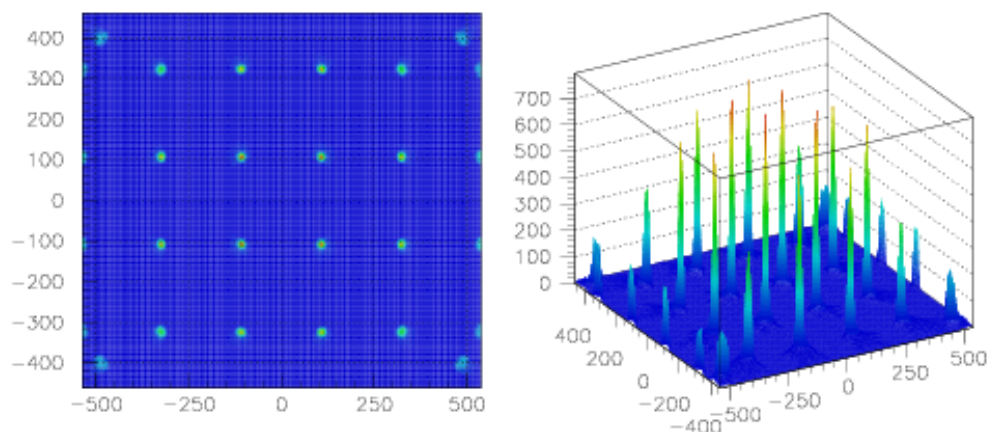
Figure 4.4: The spot size in mm scale obtained on the focal plane by the ray tracing. The focal plane is located at the 3000 mm from the center of mirrors.

thick Tempax glass. The mirror surface is coated with 200nm thick aluminum produced by the vacuum deposition. A hard protection surface of Al_2O_3 crystal with thickness of 50 nm is then produced in the solution containing ammonium hydroxide, tartaric acid and ethylene glycol. The reflectivity greater than 90% is obtained between $300 \sim 400$ nm wavelength. The spectral reflectivity can be adjusted to have a peak around 350 nm by tuning the thickness of anodization. The anodized surface is stable and the degradation of the reflectivity is $\sim 1\%$ / year. However, dusts on the mirror surface make less the reflectivity due to the expose to the outer air directly (Fig. 4.6). In order to monitor the time tendency of reflectivity, we measures the reflectivity at regular intervals by the portable reflectance spectrophotometer. The measured reflectivity of each layer in Fig. 4.6, each layer is divided by the height, shows the decreasing tendency with exposed time and localization in which the reflectivity became worse as lower layer. The mirror surface can be washed by pure water for the regular maintenance in the field. After washing the mirror, the reflectivity can be recovered (see Fig. 4.6).
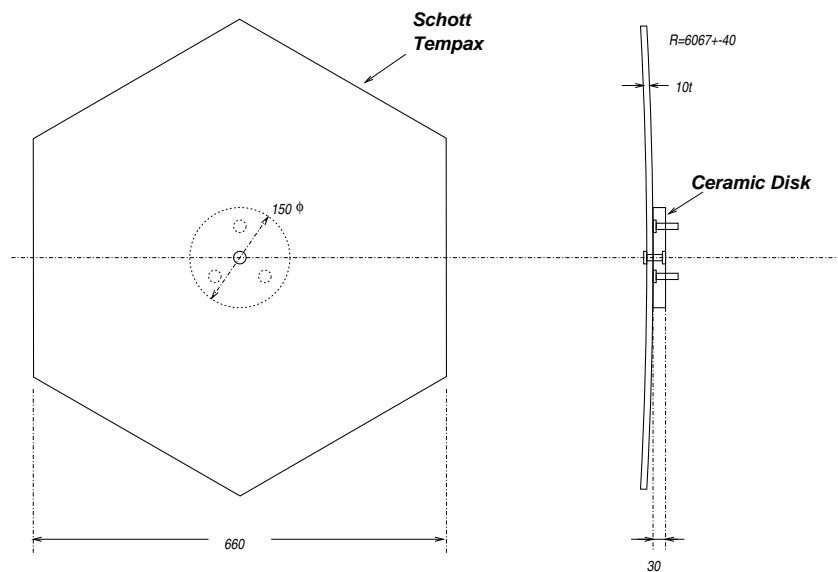
Figure 4.5: Design of the segment mirror.
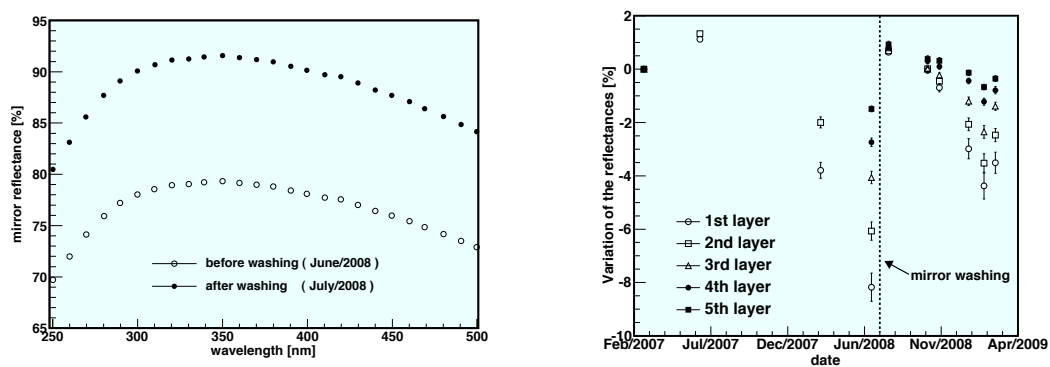
Figure 4.6: In the left, the spectral mirror reflectance of a segment mirror measured at the site. The right figure shows the time variation of mirror reflectance in five regions which are divided by height, the 1st layer is the lowest.

4.1.2   Photomultiplier Tubes and Camera

PMT cameras are installed on the focal plane of the spherical mirrors, the size of which is 1 m by 1 m (Fig. 4.7). PMT camera consists of 256 hexagonal PMTs arranged in 16×16 array to form an imaging plane which protected by the acrylic filter, KURARE paraglas. The typical transparency of the acrylic filter is shown in Fig. 4.9. Each camera covers the FOV of 18° in azimuth and 15.6° in elevation with a pixel acceptance of $1.1° \times 1.0°$ for one PMT. A UV transparent filter (BG3) with a thickness of 6 mm is attached in front of the PMT to reduce the number of night sky background photons with extra wavelength of our interest. The typical transparency of BG3 is shown in Fig. 4.9. The night sky background is ∼30 photoelectrons in 100ns.

HAMAMATSU R9508 is applied for the photon sensor of TA FD, which has a hexagonal bialkali photocathode and borosilicate glass window. The dimensions of the PMT and a typical quantum efficiency are shown in Fig. 4.10. The PMT has 8 dynodes of a box-line focus type. All of the PMTs have different applied negative high voltages and are set to have an equal gain of 8×10^4. The PMT is DC-coupled in order to measured the night sky background directly.

In the PMT camera, PMTs are arranged in zigzag with 1 mm spacing. The sensitive area of PMTs is not uniform. The spot size on the focal plane is less than 30 mm. Therefore, output signals of PMT suffer from the non-uniformity effect. Figure 4.8 shows the averaged non-uniformity map over 253 PMTs measured by the XY-scanner which consists of the eight UV LEDs [78] and consistent with the HAMAMATSU data.

The calibration and monitoring of the PMT gain are achieved in three steps, the absolute measurement of standard PMT, the relative gain monitoring for each camera and the correction by the PMT temperature. The absolute gain of standard PMTs are measured by CRAYS (Calibration using RAYLeigh Scattering) in a laboratory [48]. The standard light source of CRAYS is the Rayleigh scattered light of a pulsed laser (N_2 337.1nm) in nitrogen molecule gas. The absolute gain is acquired to measure the scattered light with the 10MHz FADC readout system which is used at the TA FD. Two or three standard PMTs whose gain was measured by CRAYS are installed
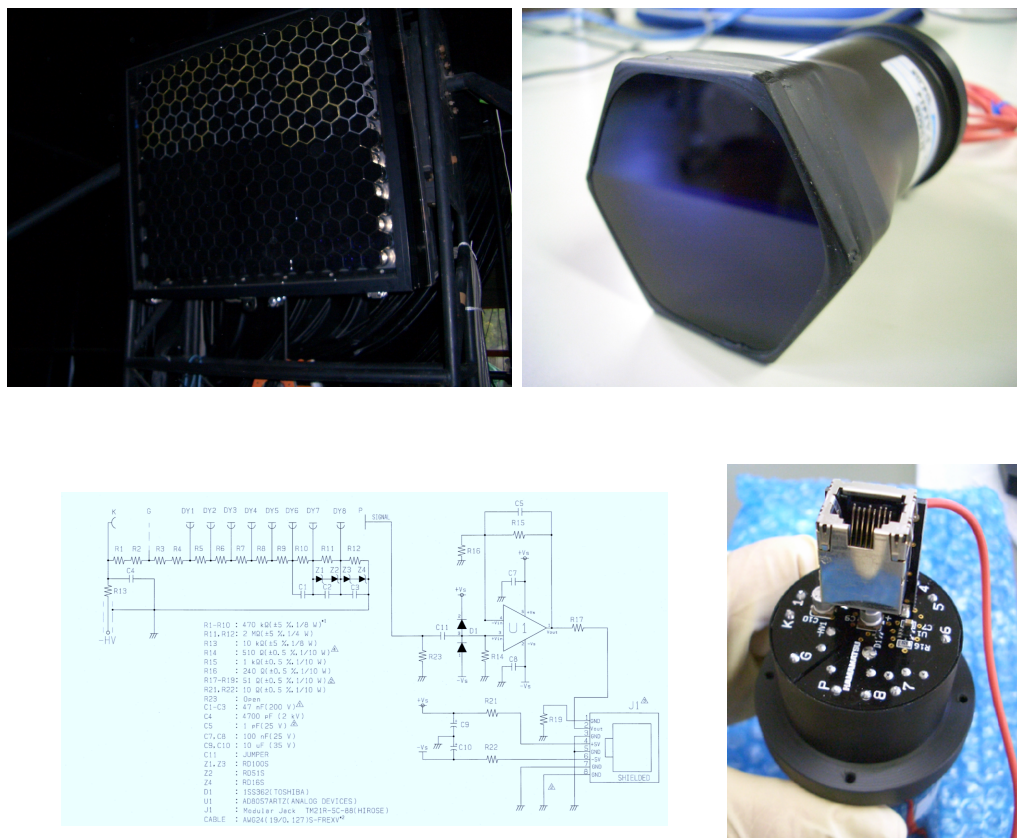
Figure 4.7: The upper left is the PMT camera in which 256 PMTs are installed and protected by the acrylic window. The upper right is the PMT in front of which the BG3 UV filter is attached. The lower left is the outline of the PMT, HAMAMATSU R9508. The lower right is the breeder circuit and the preamplifier of PMT.

in each camera. In order to monitor the gain of standard PMTs, a small light pulser
of YAP (YAlO$_3$: Ce) scintillator with ^{241}Am [49] is mounted in a BG3 filter of them.
The gain of other PMTs can be monitored relatively to compare with the intensity of
Xe flush lamp which is installed in the center of each mirror [78]. Figure 4.10 shows the
relative light intensity of Xe flasher. Responses of PMT and preamplifiers depend on
temperature. In order to correct the temperature dependence, for several PMTs the
typical temperature coefficient including preamplifiers was measured. Temperatures
of each camera which contains PMTs are measured every minute with a thermometer
installed inside of that. Therefore, we can correct the temperature effects.
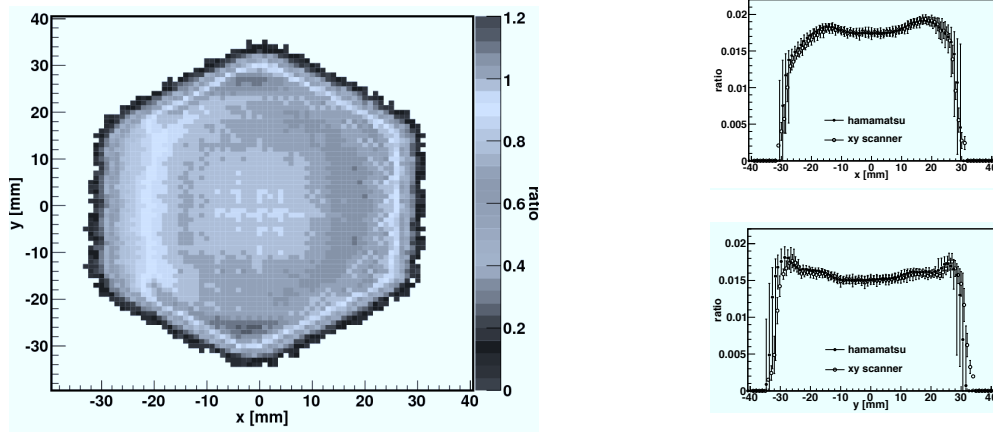
Figure 4.8: Left: The typical non-uniformity map with 1 mm × 1 mm resolution
of the photo-cathode of the PMTs. Right: The comparison of the non-uniformity
between our measurement and HAMAMATSU data.
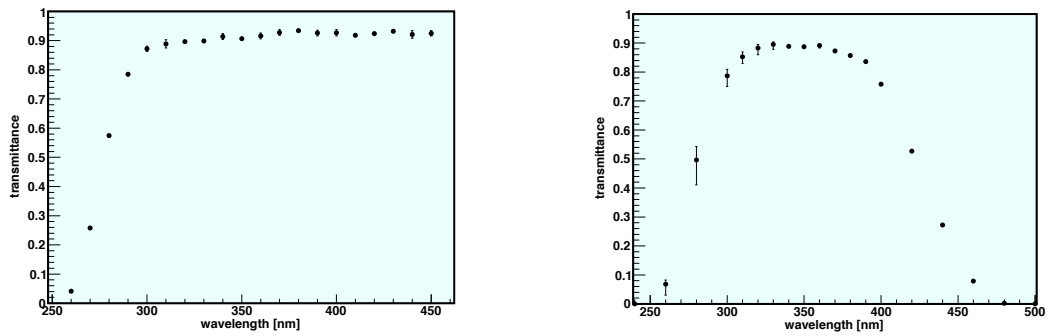
Figure 4.9: The typical transmittance of the acrylic filter to cover the PMT camera (left) and the UV filter (right).
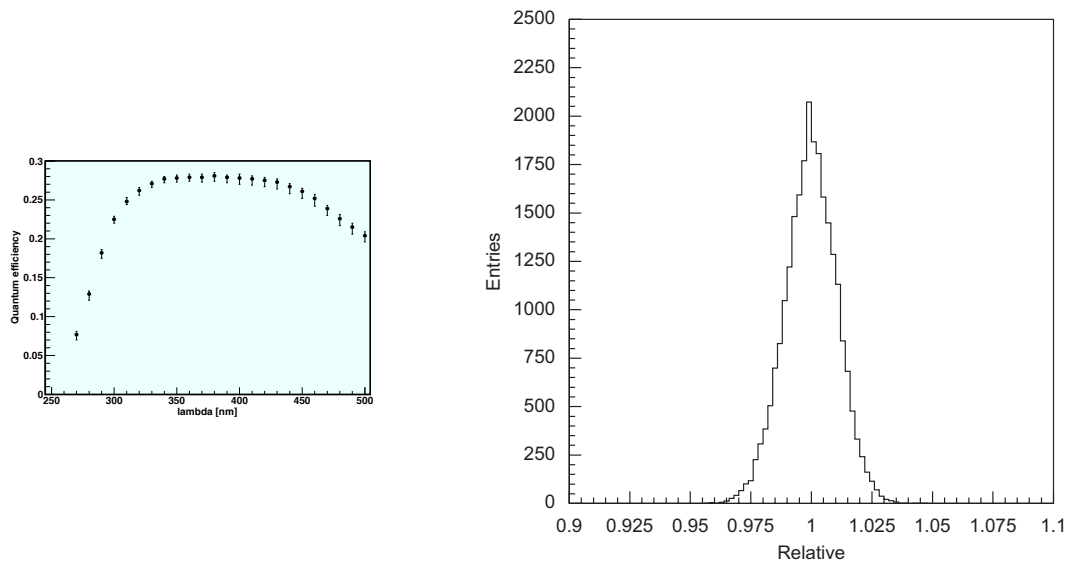
Figure 4.10: Left: The typical quantum efficiency of a photomultiplier tube, HAMA-MATSU R9508. Right:The typical relative light intensity of Xe flash lamp.

4.1.3   Trigger Electronics

TA FD trigger electronics consists of three type modules: 1) Signal Digitizer and Finder (SDF), 2) Track Finder (TF) and 3) Central Trigger Distributor (CTD). The SDF module digitizes and records the signal from PMT and calculates S/N to find fluorescence signals. The TF module recognize the air shower track based on the result of SDF. The CTD module unifies all of the modules and controls the DAQ (Data Acquisition) process.

Signal Digitizer and Finder

The SDF module digitizes the signal from PMTs by 12bit 40MHz FADC and records the output of FADC added up with 4 bins as a waveform[76]. Each SDF has 16 input channels from PMTs and 16 SDFs are assigned for each telescope.

In order to find large excess signals over the night sky background, SDF calculates moving average in several time windows of 1.6, 3.2, 6.4 and 12.8μs. The average and the standard deviation are also calculated from past 1.6ms, to normalize moving average counts. For every 12.8μs time frame of 25.6μs width, the SDF module examines the moving average counts to find fluorescence signals by comparing with a preset threshold level. The result of signal finding is sent to the TF as the first level trigger.

Track Finder

The TF module processes the hit patterns of one camera in every time frame. The hit patterns are the map of results of the first level trigger of each channel. When it recognizes the hit patterns as an air shower track, it sends the second level trigger to the CTD.

The major components of the TF are one CPLD (XC95288XL), one FPGA (XC2S400E), one configuration ROM (XC18V04) and nine SRAMs (CY7C1041). These devices are assembled onto a 9U VME printed circuit board. The block diagram of the TF module is shown in Fig. 4.11.

At each camera, one TF module communicates with the 16 SDFs via the VME bus lines. To form the second level trigger, the TF searches through the PMT hits,
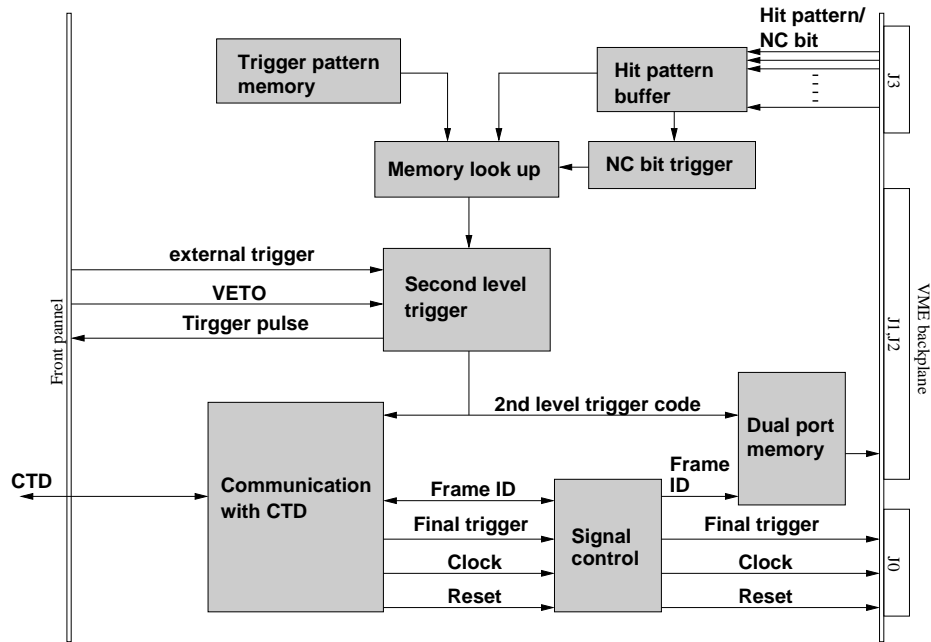
Figure 4.11: Block diagram of Telescope Array Track Finder Module.

determined by the SDFs, looking for patterns in space and time. It recognizes shower tracks on the camera or rejects accidental coincidences caused by night sky background or other noise sources such as artificial light. The TF scans over hits in the camera (as identified by the SDFs) in sub arrays of 5 by 5 PMTs. The sub array window scans over all cameras at a given observatory site for 25.6μs search window every 12.8μs. Those patterns observed are compared with the lookup table for possible track recognition. At the same time, the TF module receives "Non-Conditional" (NC) trigger information from the SDFs, which are set when significantly large signals are found in the PMTs. The TF module can also generate trigger signals by using the NC information without track identifications for calibration runs. The trigger signals generated by the TF ("second level" triggers) are sent to the CTD module. Each TF has two auxiliary inputs on its front panel for veto and external triggers, and also has an output pulse indicating a second level trigger.

The track recognition criterion for a "complete track" condition is that five adjoining PMTs in a camera are above threshold within a coincidence window of $25.6\,\mu$s, as

shown in Fig. 4.12. The TF crops a hit pattern into a 5×5 sub-matrix and searches for complete tracks in the sub-matrix. The sub-matrix is shifted column by column, row by row across the face of the camera repeating the search for a track. The number of hit patterns of 5×5 pixels is 2^{25}, the lookup table is programmed in the 8 static RAMs (CY7C1041, 256k $\times$ 16). The processing time is $25\,\mathrm{ns} \times 144$ for the pattern matchings of 144 sub-matrices in a camera.

Sliding sub matrix to search an air shower track

An example of a simulated hit pattern   Examples of the trigger patterns
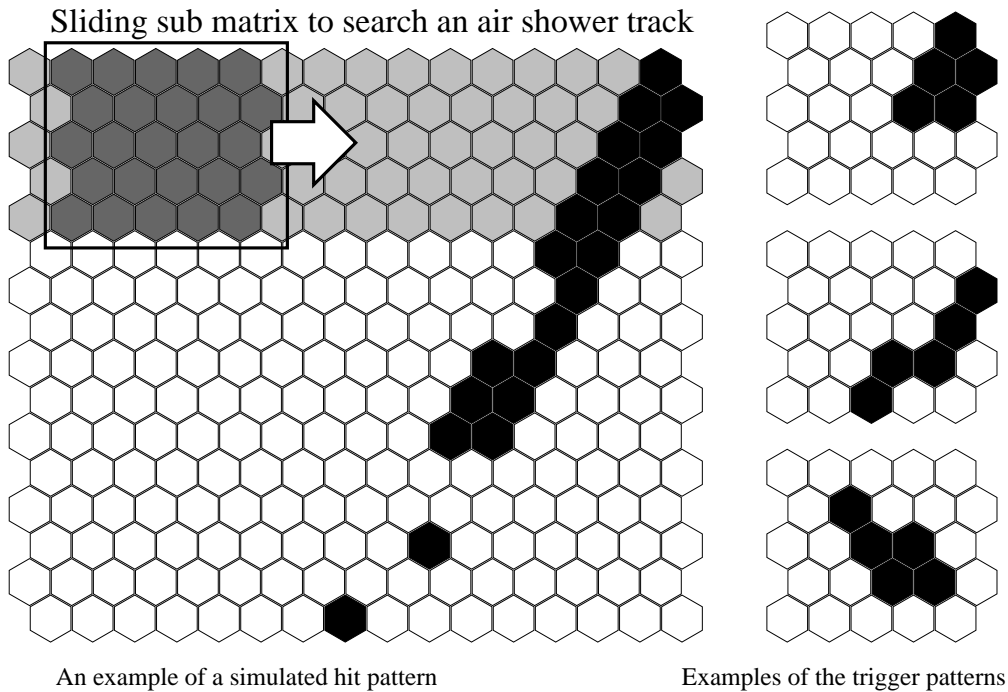
Figure 4.12: Schematic diagram of the track finding process.

An additional trigger condition implemented in the TF helps it to recognize showers which straddle two cameras leaving short tracks in each. These "partial tracks" are identified if there are three adjoining PMTs above threshold in a 4×4 sub-matrix at the boundaries of two adjacent cameras (Fig. 4.13). This is equivalent to the complete track condition, because there is an overlap with a width of one PMT (FOV $\simeq 1°$) between the fields of view of two neighboring cameras.

The TF can generate second level triggers in other two cases: first when the NC trigger initiated by a large signal in the SDF and second when an external trigger is

Sliding sub matrix to find a partial track along the camera edge

An example of a partial track hit pattern

Examples of the trigger patterns
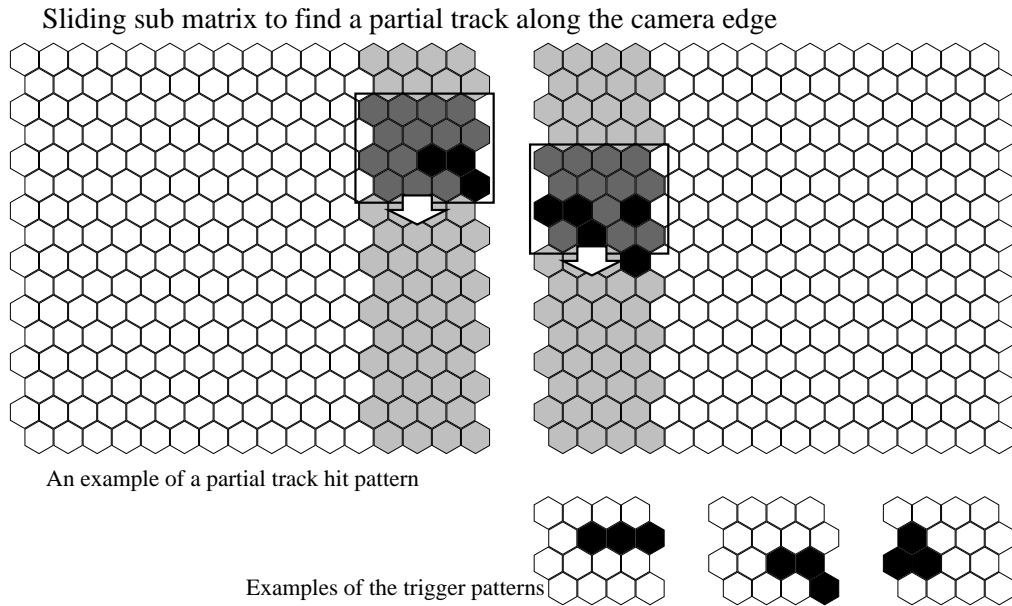
Figure 4.13: Schematic diagram of the partial track search near the boundary of a camera.

induced by a pulse input to the TF front-panel. When one of the trigger criteria is fulfilled, the TF sends the second level trigger information to CTD with a time frame ID.

Central Trigger Distributor

The CTD module generates the final trigger for the FD DAQ system to record air shower events. It also serves as the controller of the FD station system distributing the system clock to keep all of the SDFs and the TFs synchronized. It also sends the "reset" signals to initialize the frame counters.

The CTD module is a VME-9U single width board. Its major components are nine CPLD (one XC95288XL and eight XC95144), one FPGA (XC2S200E) and a configuration ROM (XC18V02). A GPS (Global Positioning System) module (Motorola M12+Timing Oncore (P283T12T1X)) is also installed on the CTD to provide precise timing of the shower events. The block diagram of CTD is shown in Fig. 4.19.

The CTD module receives and examines the second level trigger codes from all
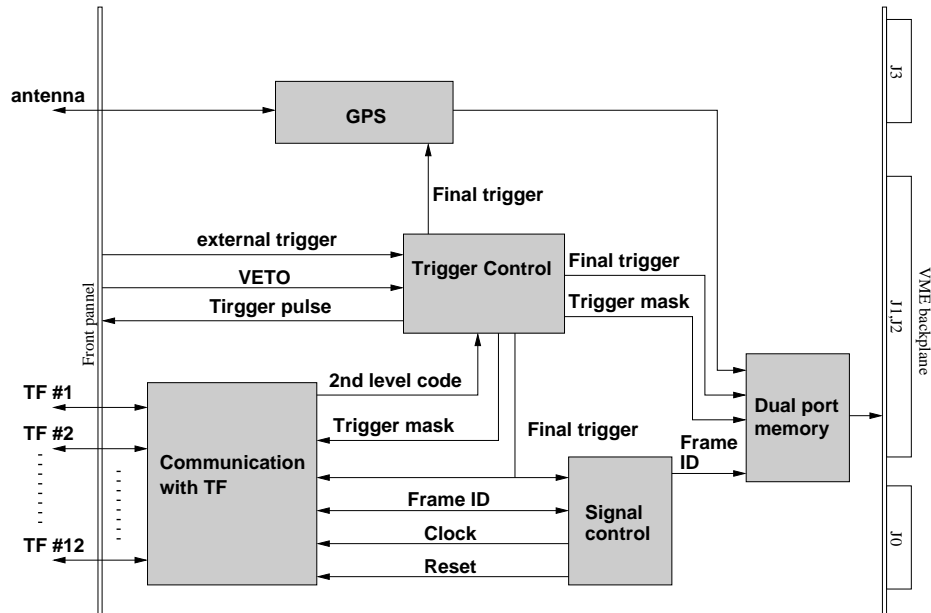
Figure 4.14: Block diagram of Telescope Array Central Trigger Distributor module.

TFs at an observatory station. When the CTD receives second level triggers with the code of a complete track from one or more TFs, it generates and distributes a "final trigger" to all TFs to record the waveform data of all the PMTs in the station. Aside from this condition, the CTD also triggers the DAQ system when two neighboring TFs send second level triggers with the code of a partial track. The CTD can generates final triggers if TFs send trigger codes of the NC triggers or external triggers for calibration runs, for example to acquire a reference light source to monitor the PMT gain [78]. A final trigger signal consists of a trigger pulse, with a readout mask which is a 12-digit binary number indicating a second level trigger in the telescopes as well as a trigger ID. At the moment of the generation of final trigger signals, the CTD and TFs send IRQ for each VME control PC to start a DAQ cycle.

Event times are calculated from the difference between the rise time of the latest 1 Pulse Per Second (PPS) signal from the GPS module and the beginning of the frame. The time difference is counted with 40 MHz system clock, the resolution of the absolute times is 25 ns. The accuracy of absolute times depends on the stability of 1 PPS signals, which is 20 ns from our measurement.

The time table of a single DAQ cycle, from the beginning of the signal finding process to the end of data transmissions into readout buffers, is shown in Fig. 4.15. It is dominated by the time required for the track finding process and data transmissions of trigger information between modules. The total process time is smaller than the frame interval of $12.8\,\mu$s. If the readout buffers of SDFs and TFs are full, CTD suspends trigger distributions. In order to measure the dead times in operations, the CTD records the IDs and the absolute times of the first and last frame in each suspended period, and also it calculates the sum (length) of these periods. This information is transferred to the VME control PC for the CTD.
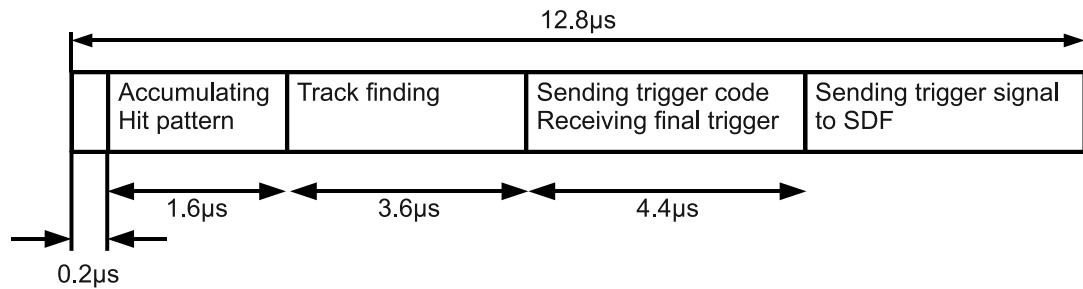
Figure 4.15: The time table of a single triggering cycle.

The CTD module supplies 40MHz system clock pulse to all the trigger electronics modules and sends the reset pulse to synchronize the all of them. If TF misses to receive the system clock, TF switches to the TF inner clock and stands the error bit.

The absolute time information can be known for each triggered event data by GPS time information and the number of clock pulses from the latest 1PPS. This time information is important in analysis other FD station's and the SD array's triggered events and accuracy of less than μ second order is required.

The clock is monitored by counting the number of the clock pulses in the interval of the 1PPS from GPS. When the frequency of clock is precisely 40,000,000, one clock pulse is equivalent to 25ns. In the actual case, there is a slight difference in the range of specification. Moreover, the number of clocks shows the temperature dependence shown in Fig. 4.16. The typical differences of clock are $-100 - -300$ clocks. The

differences are equivalent to $6.2 \times 10^{-5} - 18.7 \times 10^{-5}$ns and should be take into account.
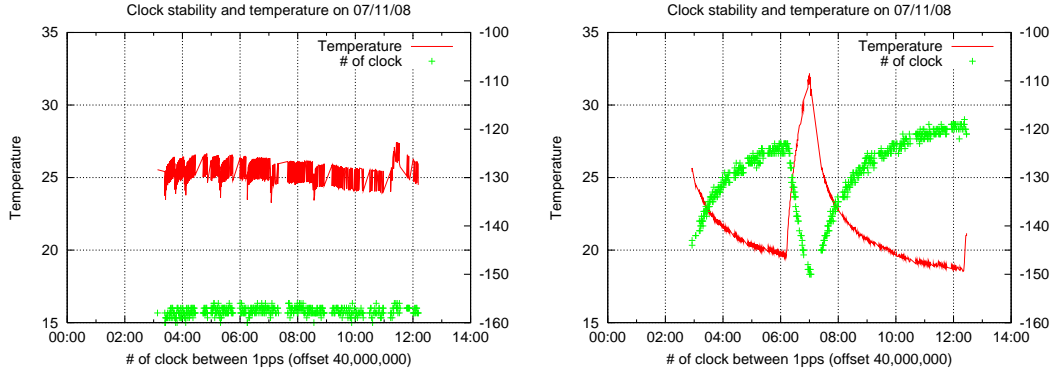
Figure 4.16: The number of clocks between in the interval of 1PPS with 40,000,000 offset and temperature at the BRM (left) and LR (right) stations. The anti correlation with temperature is shown in the number of clocks.

By track finding algorithm, aircraft exterior light is also triggered. In a stable run, trigger rate is about 2 Hz. However once airplane flights into the FOV of telescopes, trigger rate become higher to $\sim$100Hz. The CTD module can distinguish airplane trigger from others. If there are continuous trigger whose duration is over 100μs, the CTD regards them as airplane's light. After that in $\sim$10μs trigger is vetoed. Before installation of Airplane veto, the ratio of airplane was about 1/3. Now most of air plane are vetoed by the CTD.

Because of the read out and airplane veto, dead time is included in a observation time. Dead time need to be accounted for to estimate accurate exposure. The CTD module can calculate the accurate dead time. The buffer is prepared, which enable to store 8 event data. The maximum rate to acquire the air shower data is about 30Hz. This is fast enough against the expected trigger rate, which is less then 0.1Hz. If the trigger rate become more than 30Hz temporally, the data are left in the buffer not to be acquired. At this time the buffer become full (8 or predetermined limit more event data are stored) and we can not acquire the air shower data, even though there is triggered air shower event. This interval should be add up as a dead time. The TF modules send the buffer status which means the buffer is full or not to CTD. The CTD module counts the number of dead time frames and records the start and
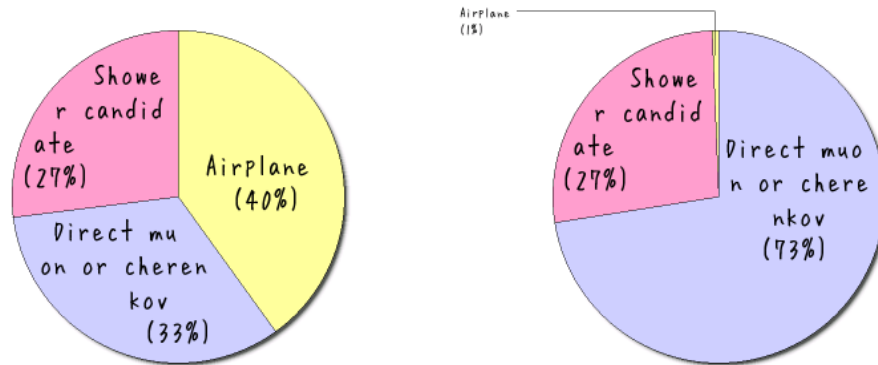
Figure 4.17: The ratio of triggered events before and after airplane veto installation.

end frame ID of dead time interval. By this information we can know the accurate dead time. Figure 4.18 is the histogram of dead time duration. The first group is caused by the airplane veto, and the second one is caused by the read out, 30ms is the minimum time to read out the data.
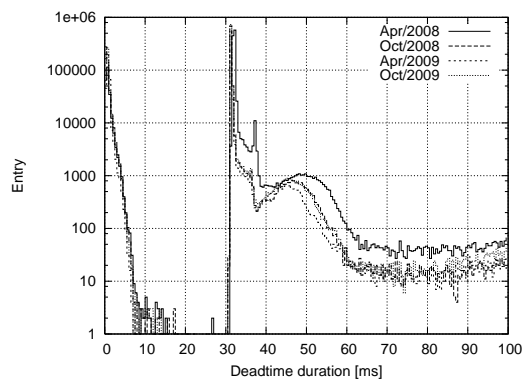
Figure 4.18: The histogram of typical dead time durations in log scale for some observation terms, Apr/2008, Oct/2008, Apr/2009 and Oct/2009.

4.1.4 Atmospheric Monitoring

TA has several atmospheric monitoring system to understand the condition of atmosphere. Air shower measurement by FD is achieved to detect fluorescence photons

emitted along the air shower axis apart from several kilo meters. The intensity of fluorescence photons are attenuated due to the atmospheric scattering in propagating through the atmosphere. In order to estimate the primary energy of air showers via detected fluorescence photon, it is quite important to understand the atmospheric profile.

LIDAR

One of the atmospheric monitoring system is LIDAR (LIght Detection And Ranging) which is widely used in the ground based observations of aerosols [79]. LIDAR is located 100 m apart from the FD station at Black Rock Mesa and consists of the pulsed laser (Nd:YAG 355nm) and the telescope mounted on the steerable stool with GPS in the dome. The system observes back scattered light of laser by air molecules via Rayleigh scattering and by aerosols via Mie scattering.

Central Laser Facility

At the center of TA site, Central Laser Facility (CLF) is located and $\sim 20\,\text{km}$ distant from FD stations [81]. CLF shoots the pulsed laser (Nd:YAG 355nm) vertical into the atmosphere. FDs observe the side scattered light of laser. The amount of scattered light from emitted 5 mJ laser at a height of 2 km is expected to be roughly equal to the fluorescence light generated by a $10^{20}\,\text{eV}$ cosmic ray. To observe the CLF event by FD, atmospheric transmittance and vertical aerosol optical depth (VAOD) can be estimated under the assumption of a one dimensional aerosol distribution.

Electron Light Source

Additionally, a Electron Light Source (ELS) is developed as an end-to-end calibration system [67]. In order to estimate the energy of comic rays, not only atmospheric profile but also fluorescence yield should be understood. The ELS system is expected to be able to calibrate fluorescence yield and detector response such as mirror reflectances, transparencies of filters, acrylic panel, Q.E. $\times$ C.E. and the gains of PMTs at the same time. The ELS is located in front of the BRM FD station 100 m apart, so that

atmospheric attenuation is negligible. The energy of the electron beam generated by the ELS is $\sim 40\,\text{MeV}$ similar to a UHECR air shower with energy $10^{20}\,\text{eV}$ at a distance of 10 km.
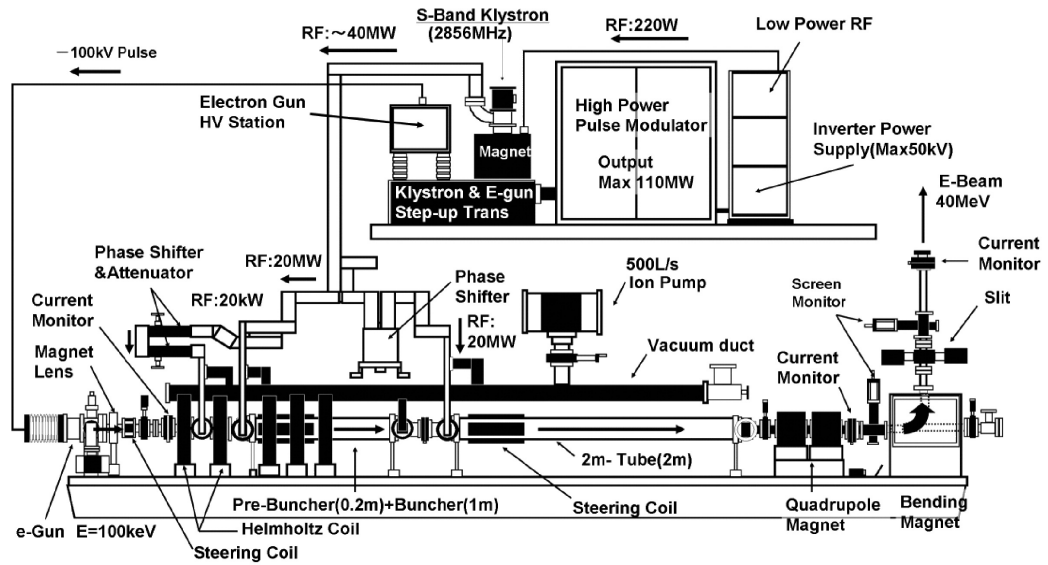
Figure 4.19: Schematic view of the ELS for the new calibration source for FD.

4.2   Surface Detector

The TA SD array consists of 507 plastic scintillation counters and arranged in a grid of 1.2 km spacing under the field of view of FDs [55]. The detection area of TA SD is 678 km^2 and is 7 times larger than that of AGASA which is 100 km^2 with 111 counters. Trigger condition is more than 3 neighboring counters which detect 3 or more muons. The trigger efficiency reaches 100% for UHECRs with energy above $10^{18.7}$ eV with zenith angle less than 45° [64]. It's duty cycle is expected to be more than 95% .

Each detector consists of 2 layers of plastic scintillators with 12 mm thick and 3 m^2 area separated with 1.0 mm stainless. 96 wavelength shifting fibers are installed in the grooves with 20 mm parallel intervals on the surface of each scintillator connected with a photomultiplier tubes (PMTs, Electrontube 91245A). The gains of all SD PMTs are adjusted by using cosmic ray muons remotely. The average of number of photo electrons induced by a Minimum Ionization Particle (MIP) is 24. The waveform signal through the low-pass filter with cut-off frequency of 9.7 MHz is digitized by a 12 bit FADC of which sampling rate is 50 MHz. The system clock is synchronized with a GPS and accuracy of arrival timing is 20ns.

Figure 4.20 is a SD after deployed. The power is generated by the solar panel of 120W capacity and $\sim$ 7W consumed by the electronics. Behind the panel a sealed lead-acid battery is also installed. SD array is divided by three areas to communicate for triggering and data acquisition by wireless LAN via an assigned communication tower in each. Boundary trigger can be achieved by the communication between the towers and hybrid trigger supplied by FD is now under planning.

Figure 4.20: On of the deployed surface detector.
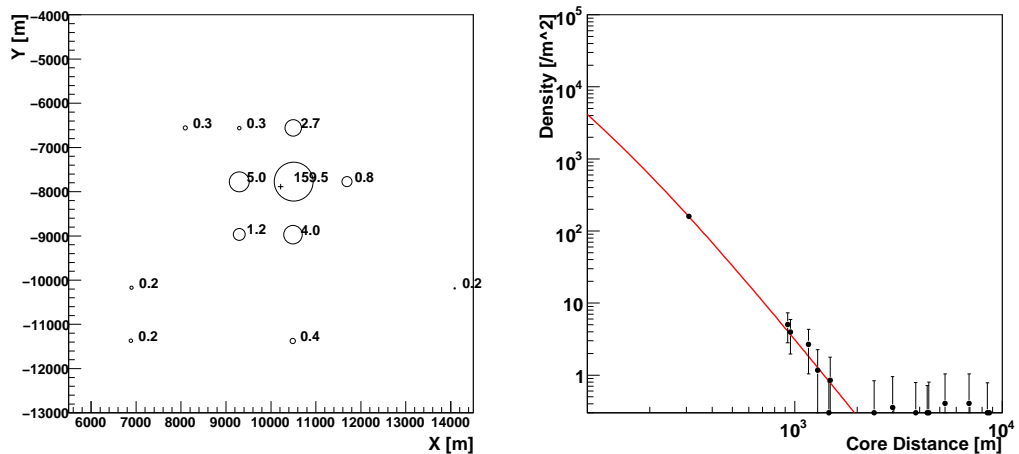
Figure 4.21: Left: A typical SD event. Circles are hit detectors with radius proportional with number of detected particles in logarithm. Right: Preliminary analysis of lateral distribution of left figure's event.

Chapter 5

TA FD Simulation and Shower Reconstruction

In order to estimate the fluorescence and Cherenkov signal at the detector, the TA FD Simulation is achieved by mainly two steps, the event generation and detector simulation. The event generation reproduces shower developments, light emission and propagation in the atmosphere In the detector simulation, the signal to be detected by the actual detector configuration is estimated. After that, the shower reconstruction is applied to the result of the simulation and the performance of the reconstruction is estimated.

5.1   Event Generation

Air shower developments in the atmosphere are given by the CORSIKA air shower simulation[38]. CORSIKA is one of the most popular detailed simulation code of extensive air showers. As primary particles, protons, light nuclei up to iron or photons can be treated. Particles travel through the atmosphere and interact with air nuclei or decay. In general, U.S. standard atmosphere are adopted, in which atmospheric

Table 5.1: Parameters of the U.S. standard atmosphere.

Layer i	altitude h(km)	a_ig/cm^2	b_ig/cm^2	$a_i$cm
1	0... 4	-186.5562	1222.6562	994186.38
2	4... 10	-94.919	1144.9069	878153.55
3	10... 40	0.61289	1305.5948	636143.04
4	40... 100	0.0	540.1778	772170.16
5	100 <	0.01128292	1	10^9

density is given by

$$T(h) = \begin{cases} a_i + b_i \exp(\frac{-h}{c_i}) & i = 1, 2, 3, 4 \\ a_5 - b_5 \frac{h}{c_5} \end{cases} \tag{5.1}$$

where h is the height and parameters are shown in table.5.1.

CORSIKA gives particle distributions at the ground and longitudinal profiles. Longitudinal profiles at each atmospheric depth are mainly divided in two parts, the number of particles and energy depositions. For the number of particles, γ, e^+, e^-, μ^+, μ^-, hadrons and nuclei are taken into account. Cherenkov photons can be optionally considered. In the energy deposition, γ energy cut, ionization and energy cut of $e^\pm, \mu^\pm$ and hadrons and neutrinos are given, where energy cut is the total energy of particles with energy below the given threshold level. For the fluorescence technique, the energy deposition can be applied which are proportional to the number of fluorescence photons in principle. Some characteristic parameters of longitudinal profile, $X_{\max}, N_{\max}, X_{\mathrm{int}}$, are also given as fitting parameters of modified Gaisser-Hillas function.

5.1.1 Simulation of Light Emission

FD telescopes detect fluorescence light emitted isotropic along shower axes. Air shower particles also emit Cherenkov light which shows the directivity along the shower axis with small angle. Although the number of photons of fluorescence and Cherenkov are comparable shown in Fig. 5.1, detected photons can be assumed

mainly as fluorescence photons due to the directivity of Cherenkov radiation, unless the direction of air shower is toward the detector. However, Cherenkov photons are scattered by the molecules or aerosols while propagating through the atmosphere. In some geometrical case of shower axes, scattered Cherenkov photons injecting the detectors should be taken into account. Such contribution of Cherenkov emission can cause overestimation of primary energy, when the detected photons are assumed as only fluorescence emission.
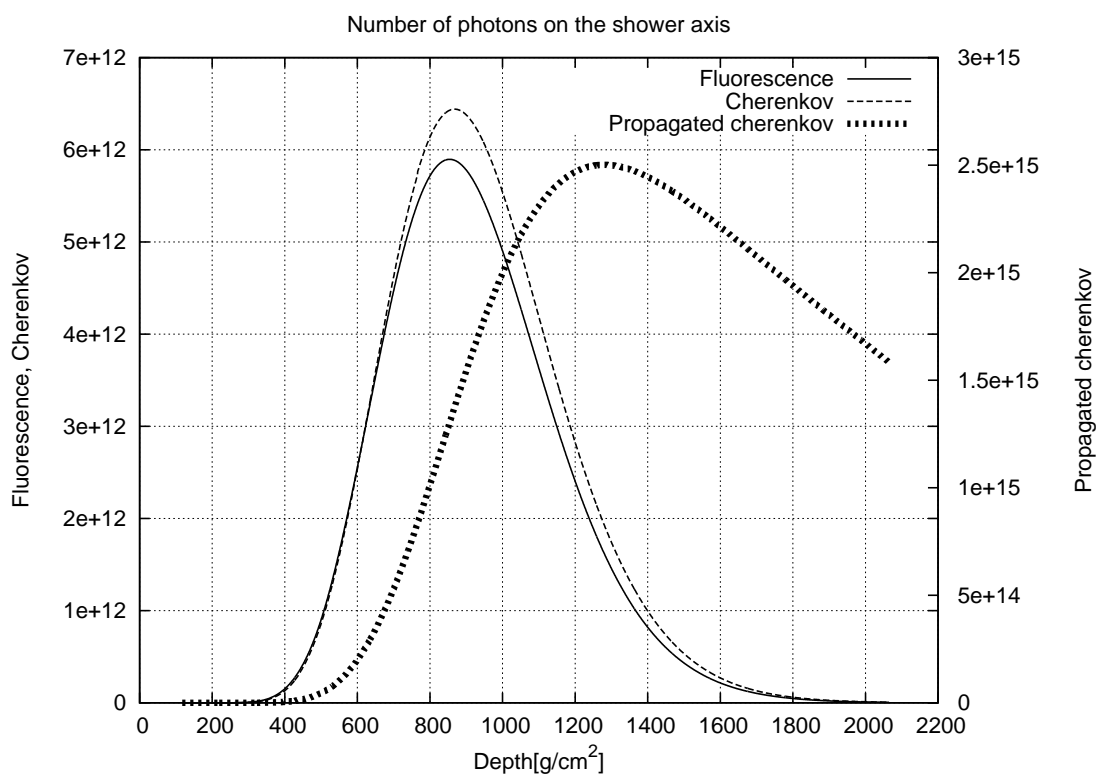
Figure 5.1: The number of photons along the shower axis emitted by an air shower caused by a proton with energy 10^{20} eV. The solid line and dashed line are the number of fluorescence and Cherenkov photons emitted at each depth. The dotted line is the number of total Cherenkov photons undergoing the attenuation by Rayleigh and Mie scattering. In this figure, the wavelength of Cherenkov emission is $250 - 500$ nm.

5.1.2 Fluorescence Emission

The number of fluorescence light is proportional to the energy deposition of charged particles and given by

$$N_\gamma^{\mathrm{fl}} \;\;=\;\; Y_{\mathrm{fl}} E_{deposit} \Delta X, \tag{5.2}$$

where Y_{fl} is the fluorescence yield [photons/eV] and $E_{deposit}$ is the ionization energy loss per depth. Fluorescence emission is isotropic, so that number of detected fluorescence photons is given by

$$N_{\gamma,\mathrm{det}}^{\mathrm{fl}} \;\;=\;\; N_\gamma^{\mathrm{fl}} \frac{A_{\mathrm{eff}}}{4\pi r^2} T_{\mathrm{atm}} \varepsilon_{\mathrm{det}}, \tag{5.3}$$

where A_{eff} is the effective mirror area of telescope, r is the distance from emission point to the detector, T_{atm} is the transparency of the atmosphere and $\varepsilon_{\mathrm{det}}$ is the detector efficiency. T_{atm} and $\varepsilon_{\mathrm{det}}$ include the wavelength, λ dependence given by

$$
\begin{aligned}
T_{\mathrm{atm}} &= \int_\lambda F_{\mathrm{fl}}(\lambda) T_{\mathrm{Rayleigh}}(\lambda) T_{\mathrm{Mie}}(\lambda) d\lambda \\
\varepsilon_{\mathrm{det}} &= \int_\lambda F_{\mathrm{fl}}(\lambda) R_{mirror}(\lambda) \tau_{paraglas}(\lambda) \tau_{BG3}(\lambda) d\lambda,
\end{aligned}
\tag{5.4}
$$

where F_{fl} is the normalized fluorescence spectrum, T_{Rayleigh}, T_{Mie} are transparency of Rayleigh and Mie scattering, R_{mirror} is the reflectivity of mirror and $\tau_{paraglas}$, τ_{BG3} are transparency of paraglas and BG3.

5.1.3 Cherenkov Emission

The shower particles emit the Cherenkov light when their energy is greater than threshold energy given by

$$E_{\mathrm{th}}(h) \;\;=\;\; \frac{m_e c^2}{\sqrt{2\delta(h)}}, \delta(h) = n(h) - 1. \tag{5.5}$$

where m_e is the electron mass and $n(h)$ is the refractive index of atmosphere at the height h. In the case of electrons, the threshold energy is 21 MeV at the sea level, where $n = 1.00029$. The energy distributions of shower particles are given by the shower age (Fig. 5.1.3 left).
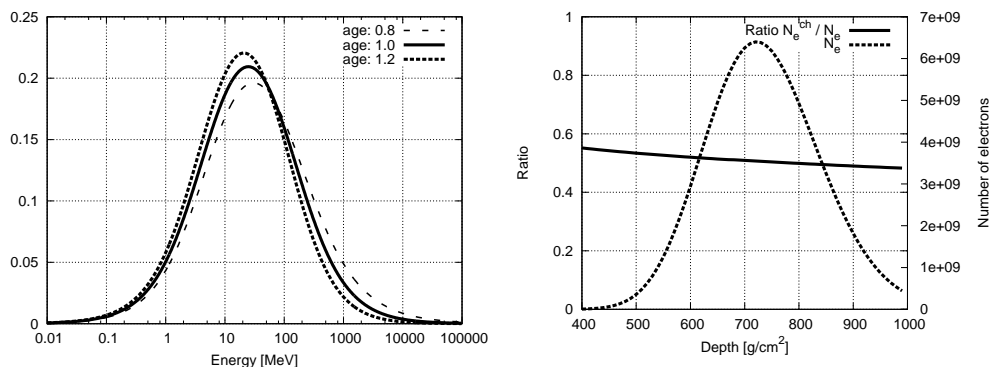
Figure 5.2: Left: The energy distribution of electrons in an air shower for each ages. Right: The ratio of the number of electrons emitting Cherenkov light.
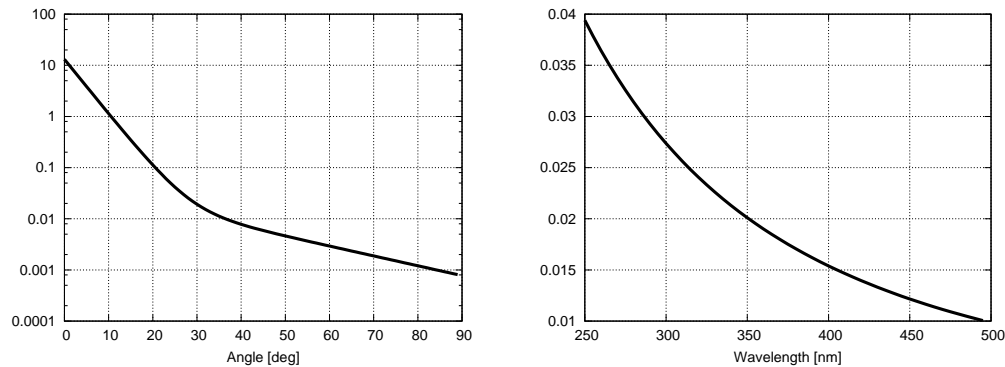
Figure 5.3: Left: The normalized angular distribution of Cherenkov light at shower age of 1.0 . Right: The wavelength spectrum of Cherenkov emission.

The smaller the shower age is, the distribution of electrons shifts to higher energy. Thus the number of Cherenkov photons shows shower age dependence. The angular distribution of Cherenkov emission obeys that of electron momentum directions and is shown in left of Fig. 5.3. The spectrum of Cherenkov emission(Fig. 5.3 right) also should be taken account. The number of Cherenkov emission detected at the

detectors

$$N_{\text{det}}^{\text{ch}} \quad = \quad N_e Y_{\text{ch}} A(\theta) T_{\text{atm}} \varepsilon_{\text{det}}, \tag{5.6}$$

where, Y_{ch} is the Cherenkov yield, $A(\theta)$ is the angular fraction, T_{atm} and ε_{det} is the detector efficiency. T_{atm} and ε_{det} also include the wavelength dependence the similar as Eq. 5.4.

5.1.4 Atmospheric scattering

In order to estimate the contribution of scattered light, the phase function of scattering should be considered. The phase function of Rayleigh scattering is given theoretical, $I(\theta) \propto (1 + \cos^2 \theta)$. However, the phase function of Mie scattering is complicated due to the size or structure of aerosols dependence. In this simulation, the phase function measured near the TA site, Dugway where HiRes located, is adopted (Fig. 5.4).
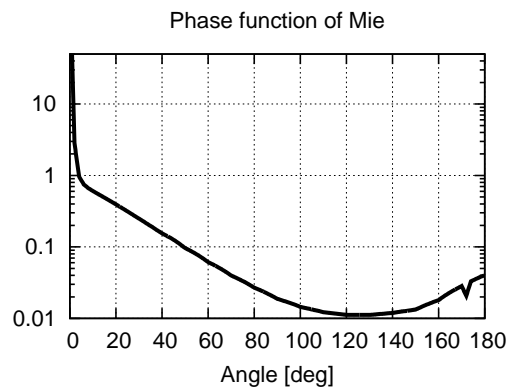
Figure 5.4: The phase function observed at HiRes site, Dugway.

5.1.5 Contribution of Cherenkov Radiation

In Fig. 5.1 dot line is the total number of Cherenkov photons at the given depth, in which atmospheric attenuation of Rayleigh and Mie scattering are considered as

following

$$N^{ch}_{\gamma,total}(X) \;\;=\;\; N^{ch}_{\gamma}(X) + T_{\mathrm{atm}}N^{ch}_{\gamma,total}(X - \Delta X) \tag{5.7}$$

where $N^{ch}_{\gamma}(X)$ is the number of Cherenkov photons emitted at the depth of X, and T_{atm} is the transparency of atmosphere. The maximum number of fluorescence photons corresponds to the shower maximum, but that of Cherenkov shifts deeper due to the attenuation propagating along the shower axis.

Figure 5.5 shows that the comparison of the number of photons reach the detector for different geometries. In Fig. 5.5, the red area is the contribution of fluorescence and the green, blue and pink are the contribution of Mie scattered, direct and Rayleigh scattered Cherenkov respectively. When the shower axis is perpendicular to the direction of FOV, across the FOV, fluorescence signal is dominant but Mie scattered Cherenkov is not so small. In the case of that the shower axis is toward to the detector (middle of Fig. 5.5), there is a huge contribution of Cherenkov light which inject directly. On the other hand, when the shower core located at not so far and across the field of view of the detector, the contribution of Rayleigh scattered Cherenkov light becomes not negligible. Thus, the estimation of scattered Cherenkov light is quite important to reconstruct the primary energy and also the X_{max}.
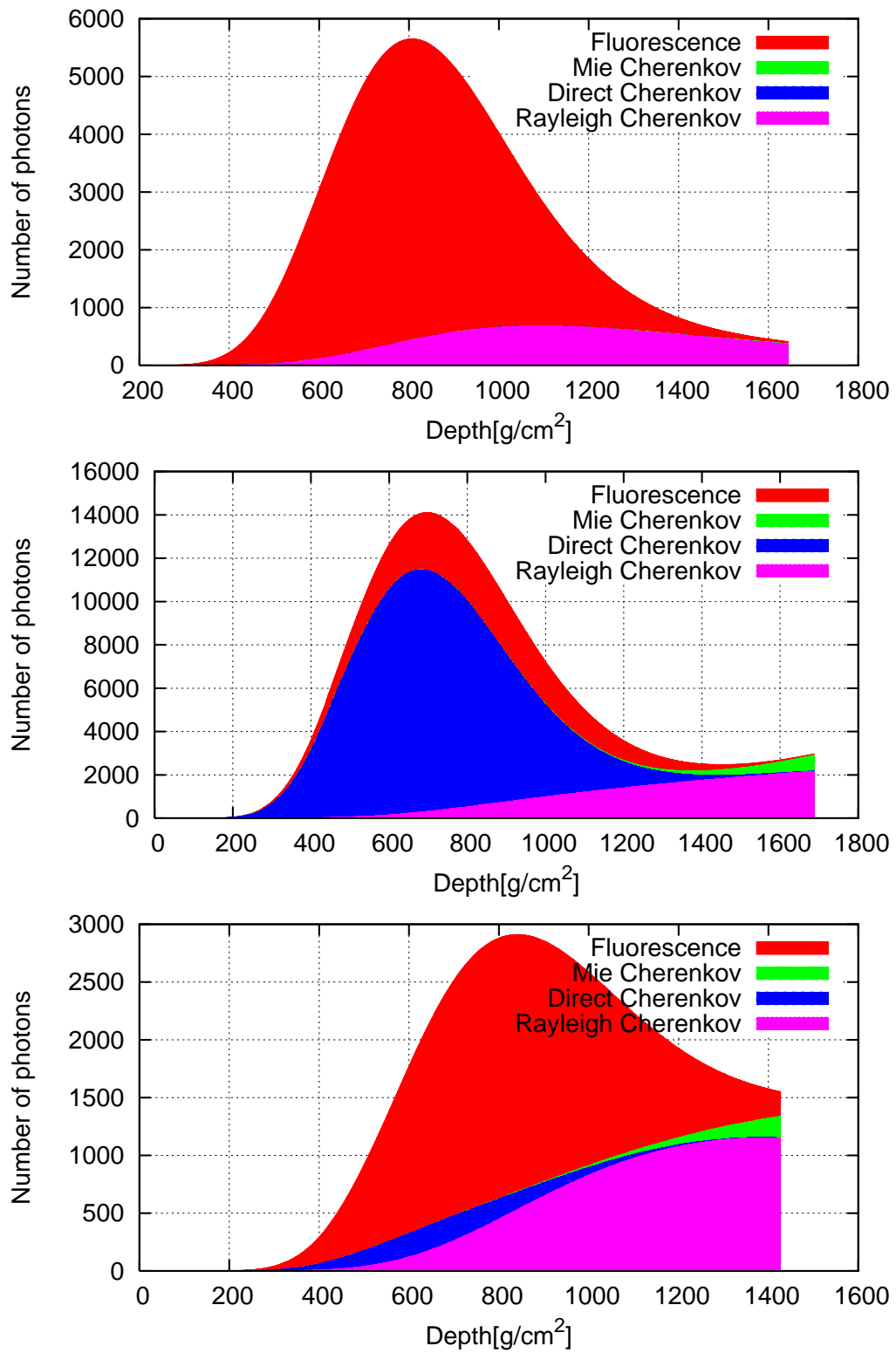
Figure 5.5: The comparison of the contribution of Cherenkov emission at the detector. Upper: crossing in the FOV. Middle: toward to the detector. Lower: crossing in the FOV nearby a station of ~ 10km.

5.2   Detector Simulation

In order to estimate the signal detected by the fluorescence detector, the detector structure and response should be simulated in the actual condition.

The fluorescence detector receives the injection photons from the outside of building which contain the twelve telescopes. From the door to the photon sensor, there are many complicated structure which obscure the flux of injection light. All the structure of detector such as the frame, building and etc. are considered based on the blue print or measured values. The example of considered structure is shown in Fig. 5.6.
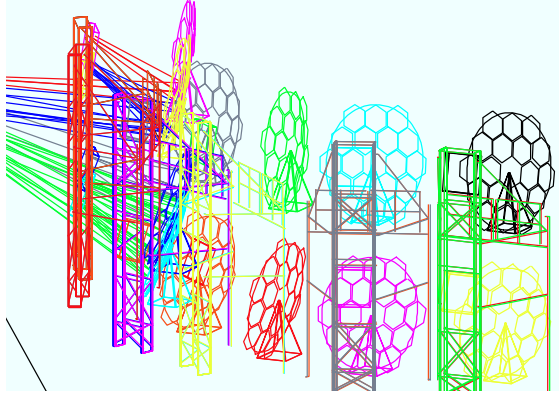
Figure 5.6: The structure considered in the Detector simulation.

For the detector efficiency, the mirror reflectivity, transparency of paraglas and BG3 UV filter and the uniformity, Q.E. and C.E. of PMT are considered. Number of photons are converted to the number of photo-electrons and finally saved as FADC counts with 10MHz time resolution. Night sky background is also taken into account. The distribution of the night sky background is Poisson distribution and include the bin to bin correlation. The signal of n_{th} bin affect the next $(n + 1)_{\text{th}}$ bin so called bin to bin correlation. The variance of that is ~ 8 photo-electron which is the typical value observed at the TA site.

5.3   FD Shower Reconstruction

The procedure of FD shower reconstruction is mainly divided in PMT selection, geometrical reconstruction and shower development reconstruction. The geometrical reconstruction is achieved by the information of viewing directions of triggered PMTs. Triggered PMTs include accidental triggered PMTs, so that such PMTs should be excluded. After geometrical reconstruction, the shower development on the reconstructed shower axis are reproduced by Monte Carlo simulation.

5.3.1   PMT Selection

Triggered PMTs include the PMTs which triggered accidental caused by night sky background. These PMTs should be excluded, which can mislead in the geometrical reconstruction or overestimate the number of detected photons. The PMT selection is divided in mainly three steps as following.

First Selection

At first, S/N of all the PMTs are calculated to find the fluorescence signals. The calculation of S/N is based on the algorithm of SDF. The SDF calculates the average and variance of baseline for several tens of milli-seconds. The moving average of the signal with several time windows, $1.6, 3.2, 6.4, 12.8\mu$ s, is also calculated, given by

$$b(t) \;=\; \int_0^{N\Delta t} a(t-\tau)d\tau \Big/ N\Delta t = \sum_{k=0}^{N-1} a(t - k\Delta t)\Big/N, \tag{5.8}$$

where $a(t)$ is the waveform data, $\Delta t = 100\,\mathrm{ns}$ and $N = 16, 32, 64, 128$. S/N is defined as

$$\mathrm{S/N} \;=\; \sqrt{\frac{N\,(b(t) - E(a))^2}{V(a)}}, \tag{5.9}$$

where $E(a)$ and $V(a)$ are the average and variance of waveform respectively. When the S/N exceeds the given threshold level, here six, the PMT is extracted.

The amount of fluorescence photons are estimated by the number of photo-electrons which is calculated by the integration of waveform. In order to the apply the proper pulse width for waveform integration, the position and width of pulse are determined by the asymmetric triangle shape fitting. The position given by the fitting is defined as the signal arrival timing.

Second Selection

The first selection cannot exclude the accidental triggered PMTs enough. In the second selection, PMTs whose viewing direction obviously do not point shower tracks are excluded. At first, shower track is roughly determined by Hough transform in the theta-phi space, where theta and phi is the elevation and azimuth angle of PMT FOV(Fig. 5.7). Hough transform is one of the method to find the line structure[29]. In the distribution of the angle distance between the shower track and PMTs, PMTs isolated from the main distribution are excluded.
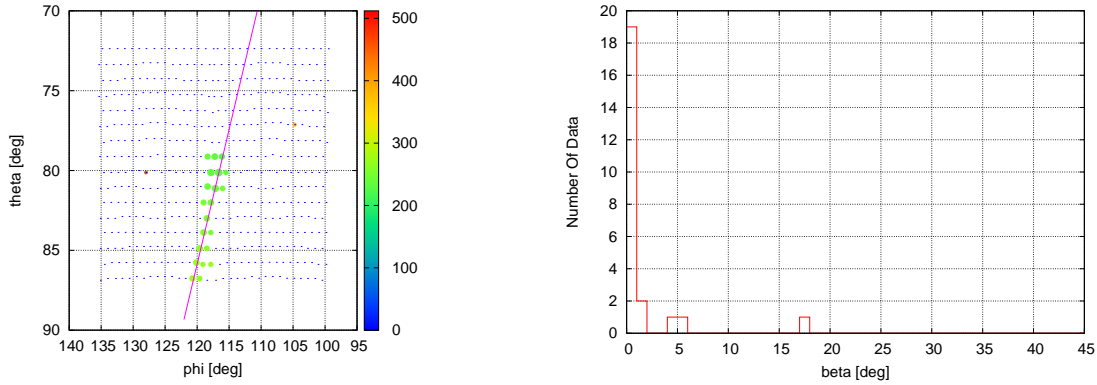
Figure 5.7: The left figure shows the viewing directions of triggered PMTs and extracted line by the Hough transform. The right figure shows the distribution of angle distance between the shower track and PMT FOV.

Third Selection

Through the two selections above, noise PMTs located on the shower tracks cannot be excluded. In the third selection, the signal arrival timing are applied to select the PMTs.

In principle, the signal arrival timing is determined by the geometrical condition of the shower axis and detectors. When ψ and α_i are the angle of the shower axis and the viewing direction of each PMTs against the direction to the center of shower track (Fig. 5.8), the arrival time of photons t_i is given by

$$t_i \;\; = \;\; t^* + \frac{1}{c} \frac{\sin \psi - \sin \alpha_i}{\sin(\psi + \alpha_i)} r_0,$$ (5.10)

where t^* is the time that shower particles arrive at the center of shower track, r_0 is the distance from the center of shower track. The open angle, α_i, between the direction vector toward the center of shower track, $\boldsymbol{n}_c$, and the PMT viewing direction vector, $\boldsymbol{n}_i$, is given by

$$\alpha_i \;\; = \;\; \cos^{-1}\left(\boldsymbol{n}_i \cdot \boldsymbol{n}_c\right).$$ (5.11)

PMTs obviously apart from the line fitted by the Eq. 5.10 can be excluded shown in Fig. 5.8.
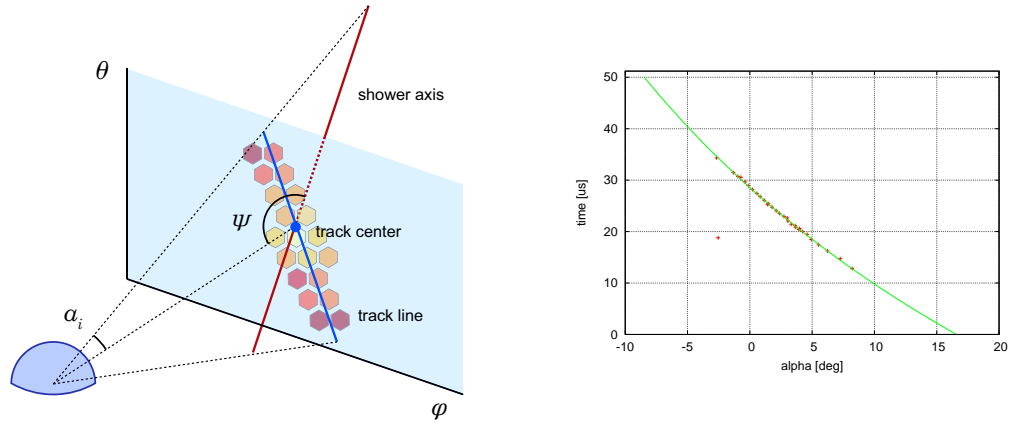
Figure 5.8: Left: The geometrical condition defined for the third selection. The result of the time fitting. Right: The geometrical condition defined for the third selection. The result of the time fitting.

5.3.2   Geometrical Reconstruction

The procedure of geometrical reconstruction is achieved by mainly two processes, determination of shower detector plane (SDP) and shower axis. SDP is the plane which include the shower axis and the detector position which is defined as the center of FD station. The vector of viewing angle of ith PMT, $\boldsymbol{k}^i$, should be nearly perpendicular with the normal vector of SDP, $\boldsymbol{n}_{\mathrm{SDP}}$. The SDP is determined to minimize the χ^2,

$$\chi^2 \;=\; \sum_i \frac{w_i(\boldsymbol{n}_{\mathrm{SDP}} \cdot \boldsymbol{k}^i)^2}{\sigma_i^2}, \tag{5.12}$$

where σ_i is the normalization factor, $\sigma_i = \sin 0.8°$, and w_i is the weight of each PMT. The weight is how close to the axis and given by

$$w_i \;=\; \frac{N_i^{p.e.}}{\overline{N}^{p.e.}}, \tag{5.13}$$

where $N_i^{\mathrm{p.e.}}$ is the number of photoelectrons of ith PMT and $\overline{N}^{p.e.}$ is that of average of all the PMTs.

In the case of stereo reconstruction, the shower axis is determined by the intersection line of SDPs of each FD station. Then the arrival direction $\boldsymbol{n}$ is determined by

$$\boldsymbol{n} \;=\; \frac{\boldsymbol{n}_i \times \boldsymbol{n}_j}{|\boldsymbol{n}_i \times \boldsymbol{n}_j|}, \tag{5.14}$$

the suffix i,j correspond to the FD stations.

5.3.3   Inverse Monte Carlo Method

Once the geometry of the shower axis is determined, the shower development is reconstructed by the intensity of injection photons at the detector. In principle, the inverse procedure of Eq. 5.3 or Eq. 5.6 can reconstruct the shower developments. However, according to the simulation, contribution of Cherenkov light cannot be neglected and

is hard to be estimated. At least two factors of Cherenkov contribution can be enumerated, the geometrical dependence in which angular distribution of Cherenkov light and scattering angle of Rayleigh and Mie should be take into account, the age dependence related with the total number of emitted Cherenkov photons. Thus, shower development is reconstructed by the Inverse Monte Carlo (IMC) method which tries various shower developments to find the most suitable with the observed data.

Using the shower axis calculated by the geometrical reconstruction, number of detected photo-electrons are simulated with various shower development based on the G-H function. Here for each G-H parameters, $X_{\max}$ is used as the fitting parameter, X_{int} is fixed as 0.0 and $N_{\max}$ is assumed 1.0. Under this condition, the $X_{\max}$ is determined to maximize the likelihood given by

$$L = \sum_{\mathrm{PMT}} \left[N^{\mathrm{PMT}}_{\mathrm{p.e.,data}} \log \left(\frac{N^{\mathrm{PMT}}_{p.e.}}{N^{\mathrm{Station}}_{p.e.}} \right) \right] \tag{5.15}$$

$$N^{\mathrm{Station}}_{p.e.} = \sum_{PMT} N^{\mathrm{PMT}}_{p.e.},$$

where $N^{\mathrm{PMT}}_{\mathrm{p.e.,data}}$ is the number of detected photo-electron of each PMT, $N^{\mathrm{PMT}}_{\mathrm{p.e.}}$ and $N^{\mathrm{Station}}_{\mathrm{p.e.}}$ are the number of simulated detected photo-electrons of each PMT at the station. Once $X_{\max}$ is determined, $N_{\max}$ is estimated as following

$$N_{\max} = \frac{N^{\mathrm{Station}}_{\mathrm{p.e.,data}}}{N^{\mathrm{Station}}_{\mathrm{p.e.}}} \tag{5.16}$$

$$N^{\mathrm{Station}}_{p.e.,data} = \sum_{PMT} N^{\mathrm{PMT}}_{p.e.,data},$$

where $N^{\mathrm{Station}}_{\mathrm{p.e.}}$ is the number of detected photo-electrons of the station. Finally, the primary energy is calculated by the integration of the G-H function over the atmospheric depth, X, given by

$$E_0 = \int_0^\infty \langle \frac{dE}{dX} \rangle f_{\mathrm{G.H}}(X) dX, \tag{5.17}$$

where $\langle \frac{dE}{dX} \rangle$ is the mean energy loss, $\sim 2.6\mathrm{MeV/g/mc^2}$, $f_{\mathrm{G.H.}}(X)$ is the G-H function

.

Figure 5.9 is a shower reconstruction result of IMC method. histograms of Fig. 5.9 is ratio of photo-electrons caused by the fluorescence or Cherenkov emission and points are number of detected photo-electrons.
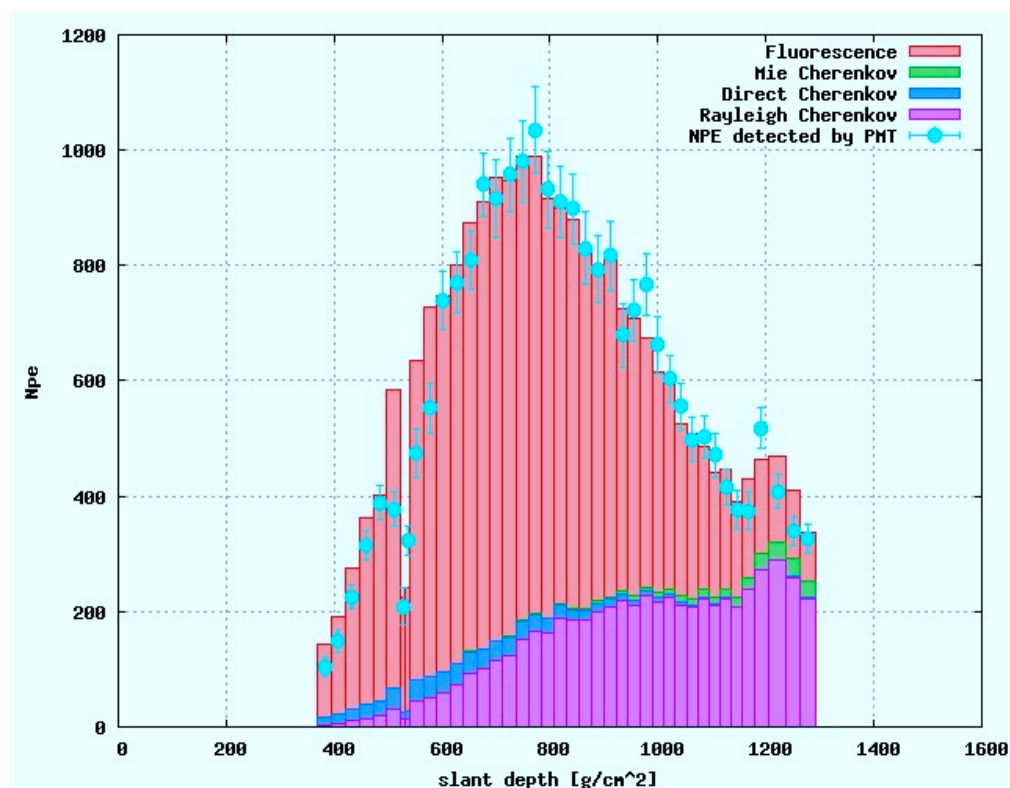
Figure 5.9: The histogram is the contribution of fluorescence and Cherenkov emission in the number of photo-electrons estimated by IMC method. The points are the number of detected photo-electrons.

5.3.4   Systematic Errors

In the shower reconstruction, there are the systematic errors by the various uncertainty. The systematics is estimated roughly 19% as following (Table 5.2). The 8% of PMT gain is the uncertainty of CRAYS measurement. The 5% of Mirror is caused by the uncertainty of the reflectivity measurement and the mirror area. The 1% of

Table 5.2: The Systematic errors of the shower reconstruction.

PMT gain	8%
Mirror	5%
Filter	1%
Aging of PMT	3%
Obstruction	1%
Mie scattering	10%
Rayleigh scattering	5%
Fluorescence yield	10%
Primary particle	5%

filter is the accuracy of measurements. The 3% of aging is the fluctuation of gain in a year. The error of Mie scattering is caused by the uncertainty of mean free path of 29.4 ± 13km. In the case of Rayleigh scattering, the uncertainty of atmospheric parameters such as pressure. The 10% of fluorescence is the systematic error of measurement [43]. The 5% of primary particle is caused by the difference of missing energy taken away by neutrinos.

Chapter 6

Mass Composition Analysis of UHECRs

In order to clarify the origin of UHECRs, determination of the mass composition is quite important. The models of acceleration by astronomical objects are constrained by the composition, such that neutron star with strong magnetic field favor heavy components. On the other hand, if the flux of UHECRs contains UHE photons or neutrinos, the exotic model such as decay of TD, z-bursts and so on can be tested. In the case of energy spectrum, the interpretation of "ankle" are transition from galactic to extra-galactic component under the assumption of mixed composition or dip due to the pair creation caused by the interaction with CMB photons in which the flux of UHECRs is dominated by purely protons.

Owing to the large fluctuation of shower longitudinal developments, the resolution of primary particle is not enough to determine the exact mass number. Thus, the mass composition analysis is achieved in statistical way using the distribution of the shower parameter, $X_{\max}$.

6.1 The $X_{\max}$ Technique

Shower developments show the energy and primary particle dependence. The higher the primary energy, the air shower develop deeper. In the case of heavy components,

nucleus can be considered as groups of protons and neutrons, so that those of air showers can be approximated by the superposition of multiple air showers caused by the protons and neutrons with lower energies. Thus, in the case of the same energies, developments of air showers induced by heavy nuclei are shallower than that of light nuclei with the same energy. Figure 6.1 is the comparison of shower developments caused by proton and iron with energy 10^{18} eV, proton air showers develop deeper and have large fluctuation in starting points of interaction. The differences is expected to be utilized to identify the primary species.
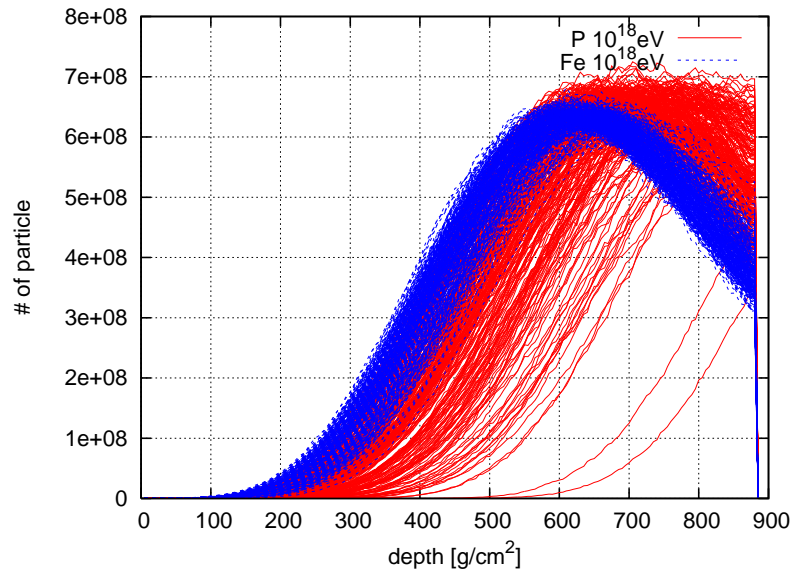
Figure 6.1: Air shower longitudinal developments of number of charged particles. Primary particles are Proton(red) and Fe(blue) with energy 10^{18} eV.

The X_{max}, the atmospheric depth at which the number of shower particles reaches maximum, is one of the most sensitive shower parameter to the primary species. The ground array measures the number of particles at the ground, the slice of shower developments. The fluorescence detectors, on the contrary, detect the fluorescence light emitted along the shower axis. Thus, the fluorescence technique is powerful strategy to identify the primary particle of air showers. However, it is difficult to determine the primary particle for event by event due to the fluctuation of developments, so that

the mass composition analysis is achieved by the comparison of the $X_{\max}$ distribution between the simulation and data.

6.2   Air Shower Simulation by CORSIKA

CORSIKA (COsmic Ray SImulations for KAscade) is the most popular code to simulate the extensive air showers initiated by high energy cosmic ray particles originally made for KASCADE experiment [38]. CORSIKA can treat many kind of primary particles as protons, light nuclei up to iron and photons, take various model of particle interaction. For hadronic interaction model, GHEISHA and FLUKA are available at low energy region and VENUS, QGSJET, DPMJET, SIBYLL, neXus, and EPOS are adopted at high energy region. For electromagnetic interactions, EGS4 or the analytical NKG formulas can be used. Options for the generation of Cherenkov radiation and neutrinos exist.

In order to acquire the distribution of $X_{\max}$, air showers are simulated in the condition of Table 6.1. The primary particle species are considered as only protons or irons because the resolution of composition is not so clear to divide in the nuclei level. Thus, the composition model is assumed as pure protons or pure irons. On the other hand, not only the various energies but also the several hadronic interaction models are adopted. The QGSJET model is based on the Gribov-Regge theory [57] [44], while SIBYLL is a minijet model [32].

The most influence factor of the shower developments are the inelastic cross-sections and the energy spectrum of forward emitted particles. However, those cannot be measured by the present accelerator and are just extrapolated. Thus, the composition analysis is achieved by using several interaction models because it cannot be concluded which model is correct. In near future, it is expected to measure the cross-section and the energy spectrum of forward particles in the energy region up to 10^{17} eV by the LHCf experiments [63].

In order to reduce the computing time, the thinning option is applied in which particles with energy below the thinning factor of primary energy are grouped as the weighted particle. Moreover, particles with energy below the E_{cut} are not traced. In

Table 6.1: The condition of air shower simulation.

Model	QGSJET-II, QGSJET-01, SIBYLL
Energy range	$10^{18.5-19.0}$ eV, $10^{19.0-19.5}$ eV, $10^{19.5-20.0}$ eV
Energy spectrum	$\propto E^{-3.1}$
Zenith	0 - 60 degree
Azimuth	random
Thinning factor	10^{-4}
E_{cut}	100keV for electromagnetic component 100MeV for hadronic component
Number of events	500

the case of the X_{max} study, thinning factor of 10^{-4} is enough to simulate the shower developments because the distribution of shower parameters such as X_{max} almost the same as the case of 10^{-5}, 10^{-6}, where the comparison with the full Monte Carlo is impossible for the huge computing time. On the contrary, thinning option should be treated more carefully, for the estimation of the particle distribution of shower particles at the ground for such as the measurement by the ground array.

6.3 X_{max} Distribution

The distributions of simulated X_{max} for various interaction models are shown in Fig. 6.2. The X_{max} of protons are deeper than that of irons in any interaction models. Furthermore, the distribution of protons X_{max} is more broad than that of irons. It looks possible to distinguish the particle species by the comparison of the distribution of X_{max}, although the distribution is partially overlapped.

Figure 6.3 are the X_{max} and energy distributions compiled from the three energy regions and normalized by the energy slope. Average X_{max} for each primary energy is shown in Fig. 6.4 calculated by the above distributions, and looks linear with logarithm of energy. If the composition is pure proton or iron, observed X_{max} agree with the each line. On the other hand, if the steeper or gentler inclination or bend structure is found, it implies the composition change with energy. The differences of

average $X_{\max}$ due to the difference models is $\sim 30\,\mathrm{g/cm}^2$ for proton and $\sim 10\,\mathrm{g/cm}^2$ for iron at the $10^{19}\,\mathrm{eV}$.
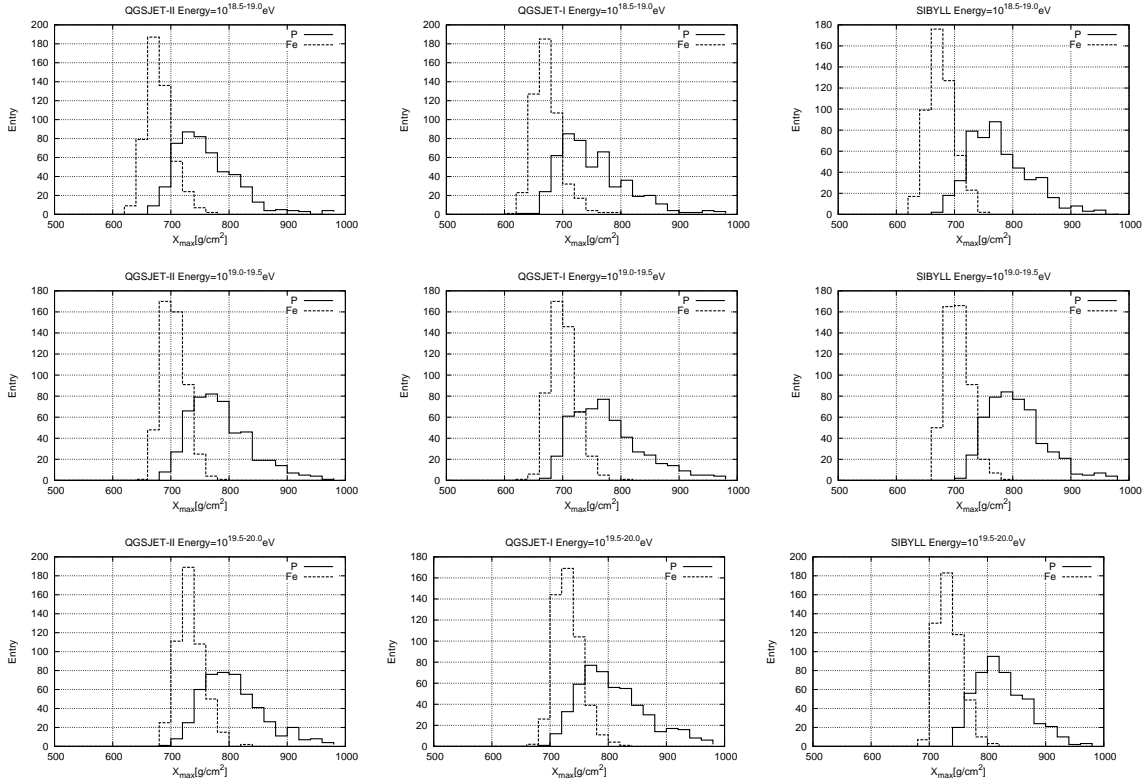
Figure 6.2: The comparison of $X_{\max}$ distribution for three energy regions, $10^{18.5}$, $10^{19.0}$ and $10^{19.5}\mathrm{eV}$ (from top to bottom), and three hadronic interaction models, QGSJET-II, QGSJET-01 and SIBYLL (from left to right).
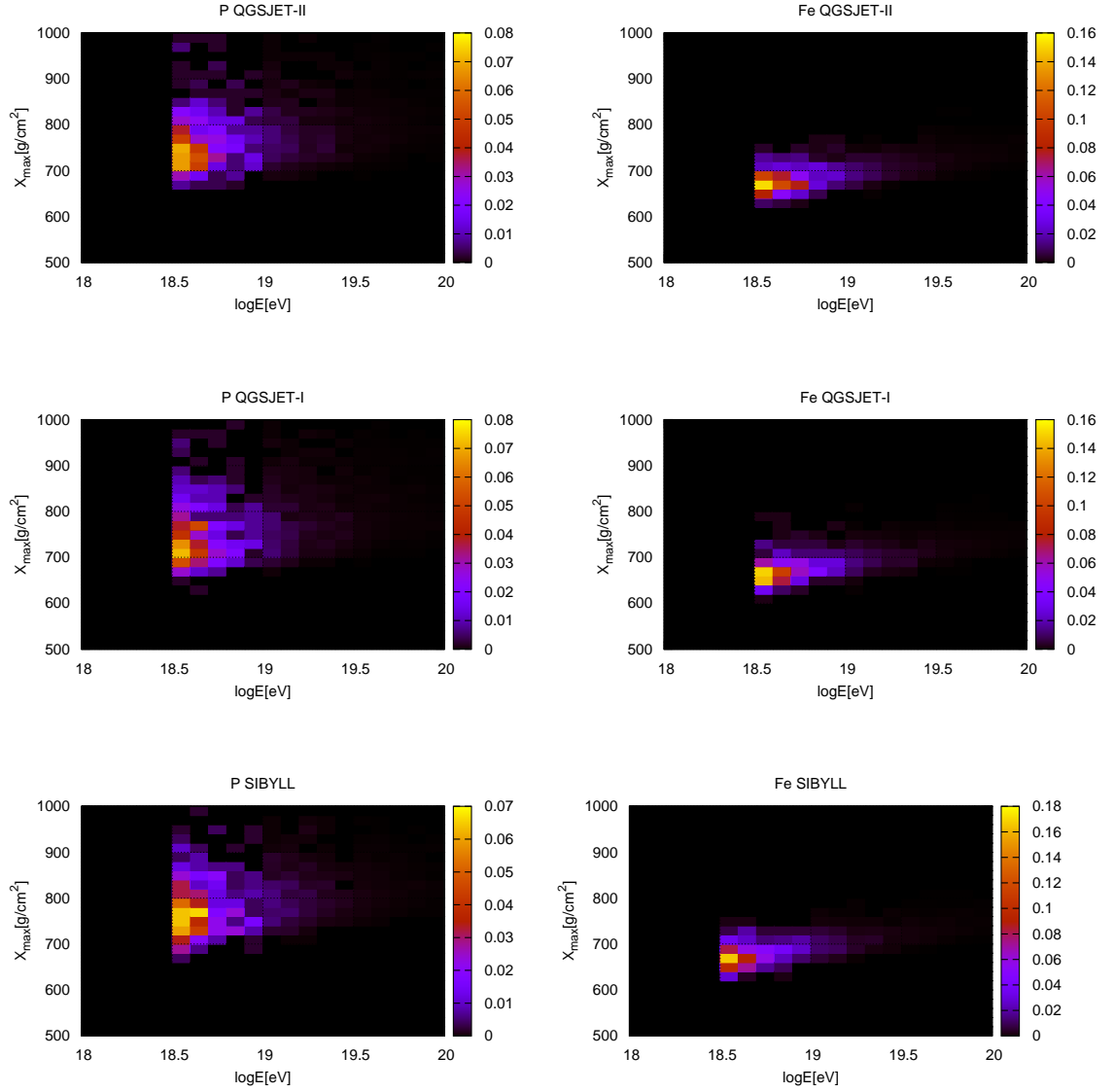
Figure 6.3: Energy and $X_{\max}$ distributions of proton (left) and iron (right) compiled from three energy regions, $10^{18.5}, 10^{19.0}$ and $10^{19.5}$eV for three hadronic interaction models of QGSJET-01, QGSJET-II and SIBYLL (from top to bottom).
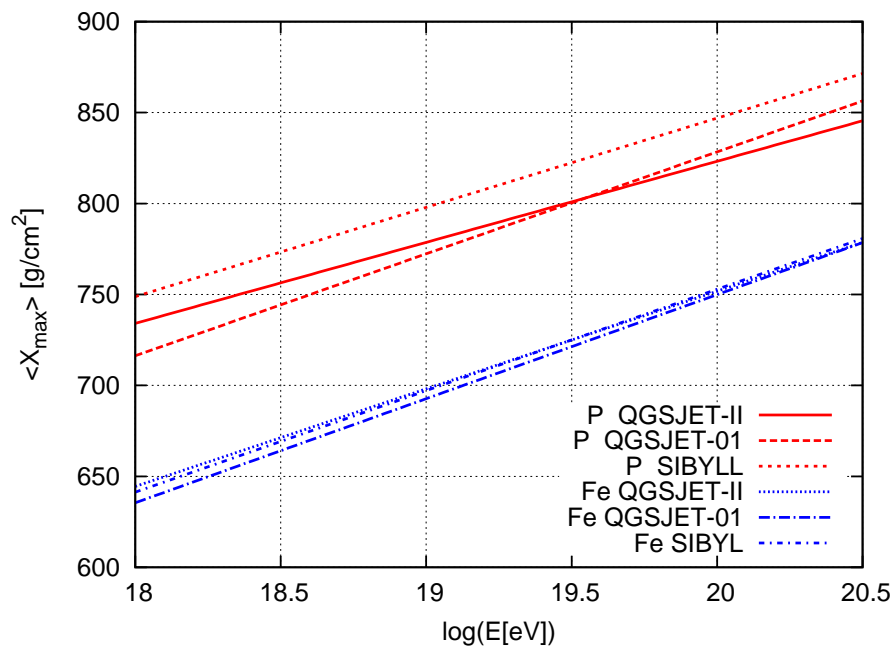
Figure 6.4: The average $X_{\max}$ calculated with the various hadronic interaction models, QGSJET-II, QGSJET-01 and SIBYLL.

6.4 Resolution Study

It is difficult to know the exact distribution of X_{max} through the observation and shower reconstruction. In order to estimate the performance of the shower reconstruction, TA FD detector simulation is achieved using the simulated air showers with the hadronic interaction models of QGSJET-II, QGSJET-01 and SIBYLL. The conditions considered in the simulation are following Table 6.2. For the atmospheric condition of Mie, the mean free path and scale height are the average values of one year measurements of LIDAR system locate at the BRM FD site.

Table 6.2: The detector simulation condition.

Detector configuration	2 FD stations (BRM, LR)
Shower cores	Within 10km around the center of 2 station
Azimuth angles	randomly
Zenith angles	$0° − 60°$
Atmosphere	U.S standard atmosphere
Mie scattering	Mean free path : 29.4km, scale height : 1.0km
Fluorescence yield	Flash [6] normalized by Kakimoto *et al.* [43]

The differences of direction, core position, energy and X_{max} between the simulated air showers and reconstructed for the case of QGSJET-II are shown in Fig. 6.5, 6.6, 6.7 and 6.8, respectively. The systematics and resolution for QGSJET-II is shown in Table 6.3. The distribution of reconstructed energy and X_{max} which expected to be observed is shown in Fig. 6.9. The resolution of X_{max} is $\sim -10\text{g/cm}^2$, there are apparently difference between the distribution of X_{max} and energies. Thus, the distribution is applied for the mass composition analysis.

For the shower reconstruction, when the X_{max} is outside of FOV of FD, the accuracy becomes much worse; before shower developments reach the shower maximum, it is difficult to extrapolate the following developments. The height of TA site is $\sim 1400\text{m}$ which equivalent the vertical atmospheric depth of $890\,\text{g/cm}^2$. It is desirable that the X_{max} is inside of FOV of FD. The Fig. 6.10 is the distribution of observed depths , X_{max},X_{start} and X_{end}, where X_{start} and X_{end} are the shallowest

and deepest atmospheric depth to be detected by the FD. Almost X_{max} are located between X_{start} and X_{end}.

In Section 6.3, the rails of average X_{max} (Fig. 6.4) was calculated based on the energy and X_{max} distribution acquired by the air simulation. However, observed energy and X_{max} distribution can not be compared with this average X_{max} rails due to the X_{max} cut bias or the bias of the shower reconstruction. The average X_{max} rails which should be compared with the data is calculated based on the reconstructed parameters by the TA FD simulation and the same reconstruction procedure as for the data. The same cut for the data should be also applied for the simulation as following; energy is above $10^{18.6}$eV, zenith angle is less than 56°, core location is within 9.6 km from the middle point of 2 FD stations and X_{mas} is within the FOV of FD. Figure 6.11 shows the average X_{max} fitted with the reconstructed energy and X_{max} distribution after the cut above.

Table 6.3: The systematics and resolutions of reconstructed parameters for each primary particle and energy (QGSJET-II). $\Delta\theta$ is the open angle between the arrival direction of simulated and reconstructed. ΔR is the difference of core location between the simulation and reconstructed. ΔE and ΔX_{max} are the systematics and resolution of Energy and X_{max}.

	log(E[eV])	$\Delta\theta$[deg]	ΔR[m]	ΔE[%]	ΔX_{max}[g/cm^2]
	18.5-19.0	1.89	238	-8.51 ± 6.18	-7.83 ± 18.57
P	19.0-19.5	1.59	178	-5.39 ± 5.77	-9.70 ± 16.30
	19.5-20.0	1.02	157	-3.29 ± 6.65	-6.77 ± 19.07
	18.5-19.0	1.73	232	-14.41 ± 5.46	-11.29 ± 13.82
Fe	19.0-19.5	1.19	153	-9.62 ± 4.24	-9.58 ± 10.64
	19.5-20.0	0.97	125	-4.62 ± 4.36	-9.16 ± 10.97
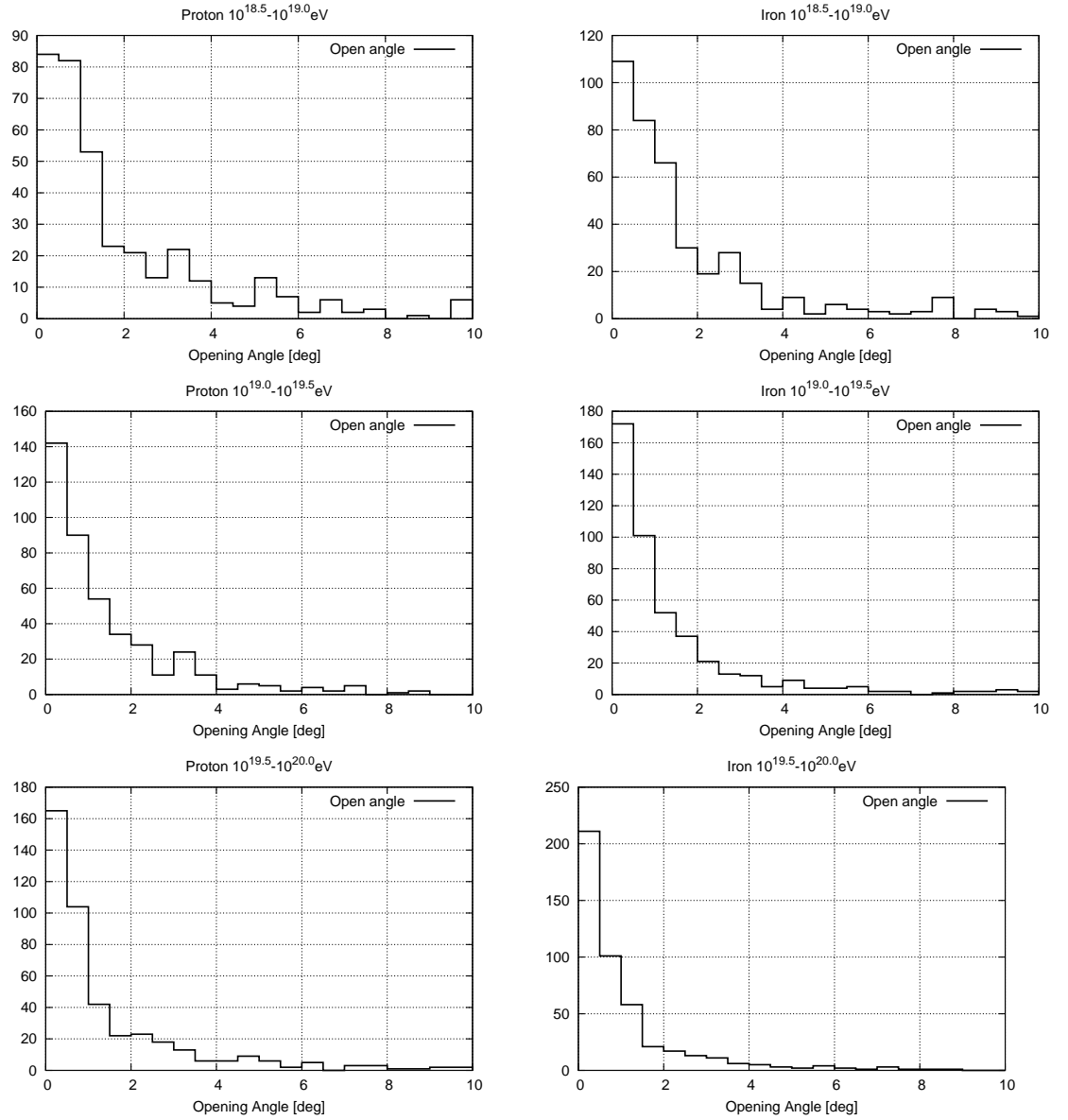
Figure 6.5: The differences of direction between the simulation and reconstruction for each energy regions of $10^{18.5}$, $10^{19.0}$ and $10^{19.5}$eV (from top to bottom). Primary particles are Protons (left) or Irons (right). Hadronic model is QGSJET-II.
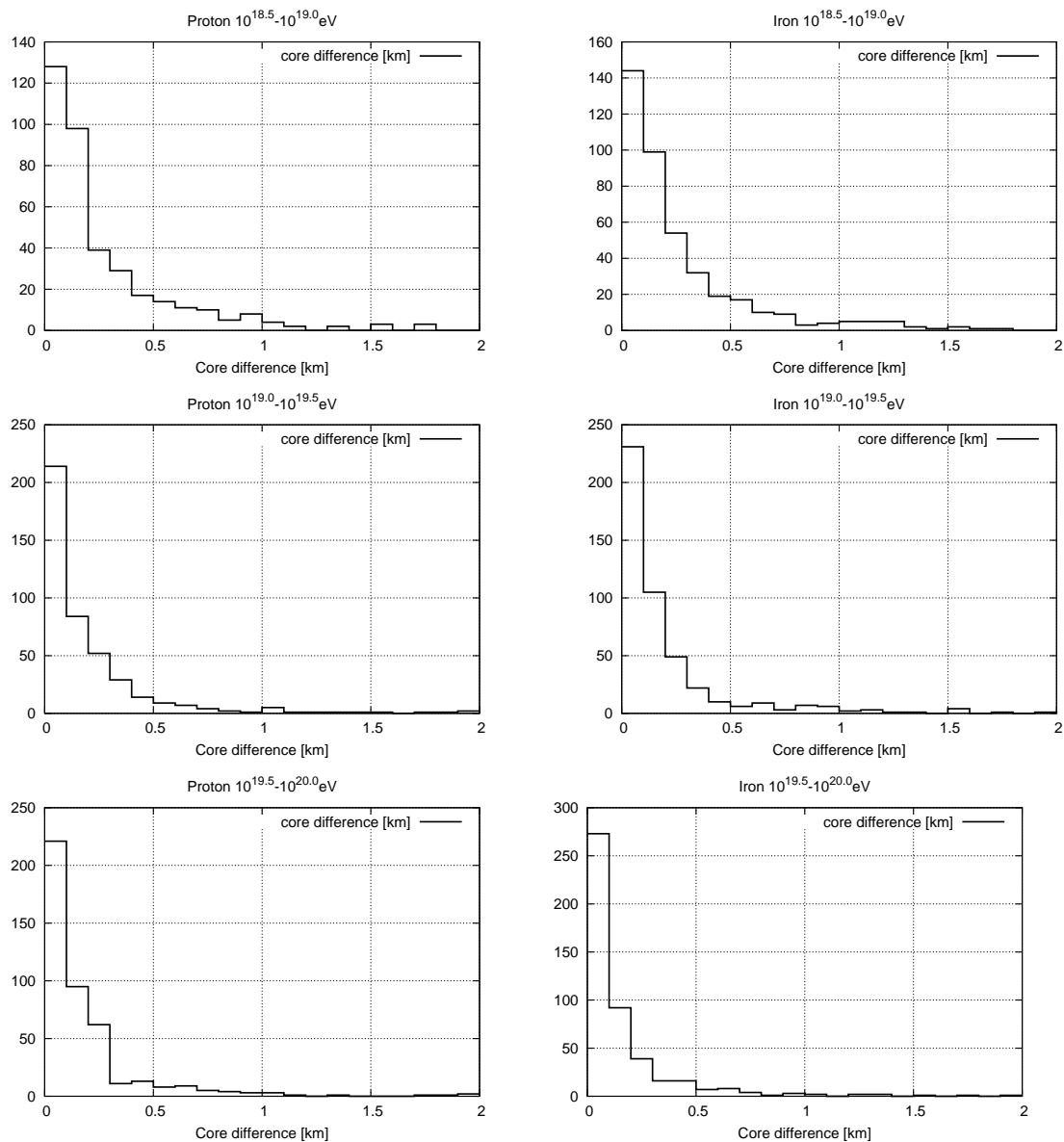
Figure 6.6: The differences of core position between the simulation and reconstruction for each energy regions of $10^{18.5}, 10^{19.0}$ and $10^{19.5}$eV (from top to bottom). Primary particles are Protons (left) or Irons (right). Hadronic model is QGSJET-II.
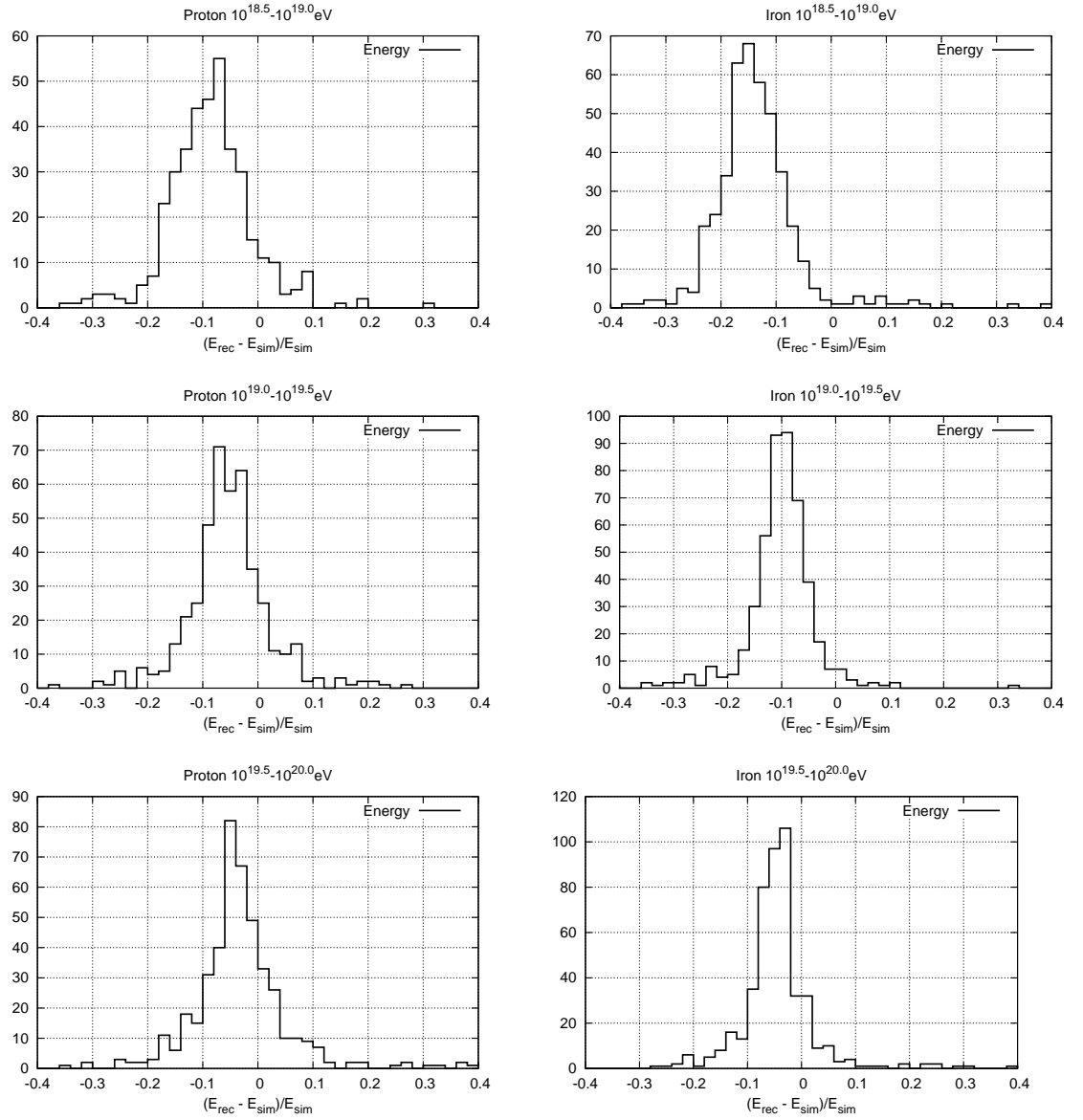
Figure 6.7: The differences of energy between the simulation and reconstruction for each energy regions of $10^{18.5}, 10^{19.0}$ and $10^{19.5}$eV (from top to bottom). Primary particles are Protons (left) or Irons (right). Hadronic model is QGSJET-II.
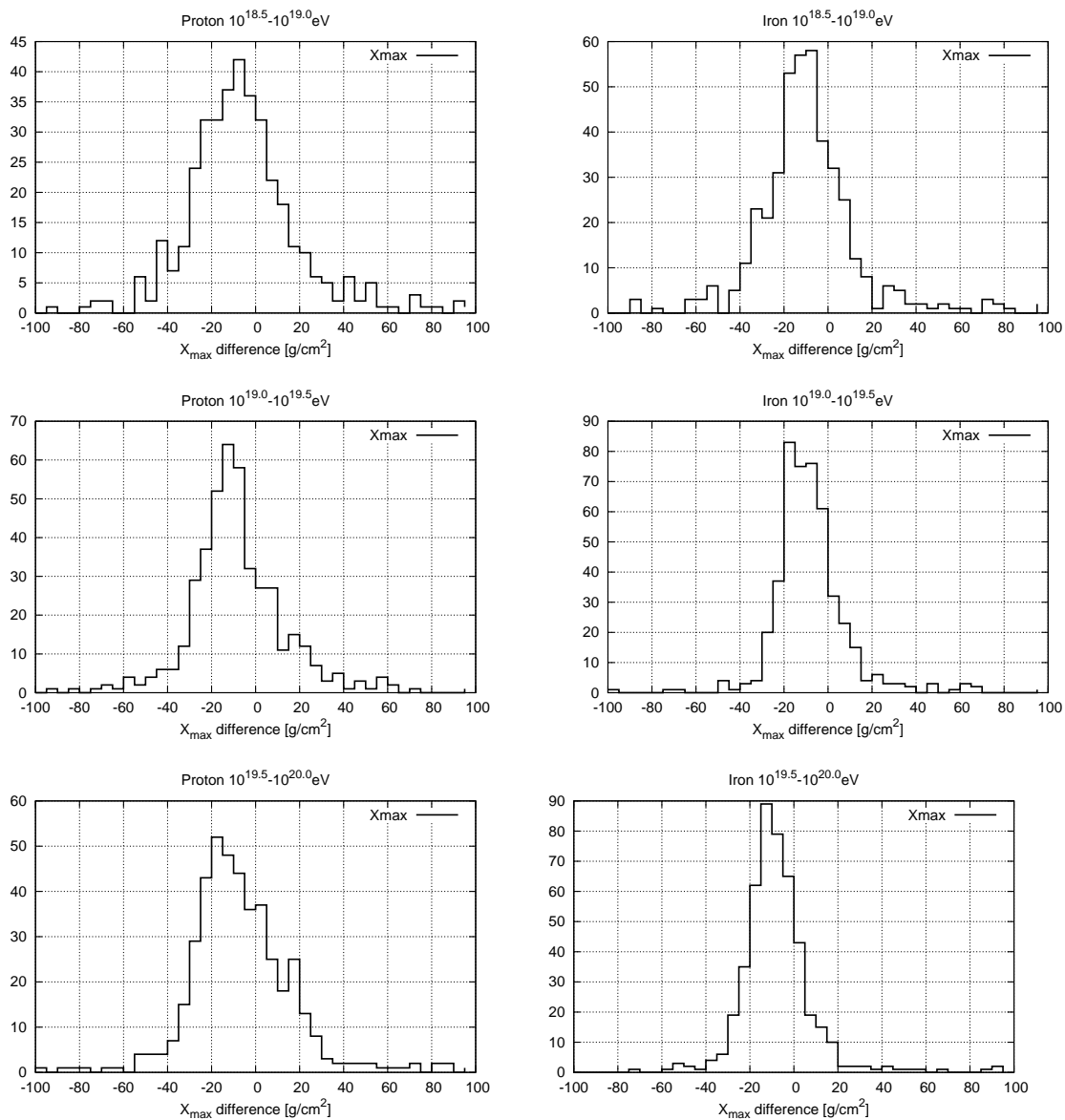
Figure 6.8: The differences of $X_{\max}$ between the simulation and reconstruction for each energy regions of $10^{18.5}$, $10^{19.0}$ and $10^{19.5}$eV (from top to bottom). Primary particles are Protons (left) or Irons (right). Hadronic model is QGSJET-II.
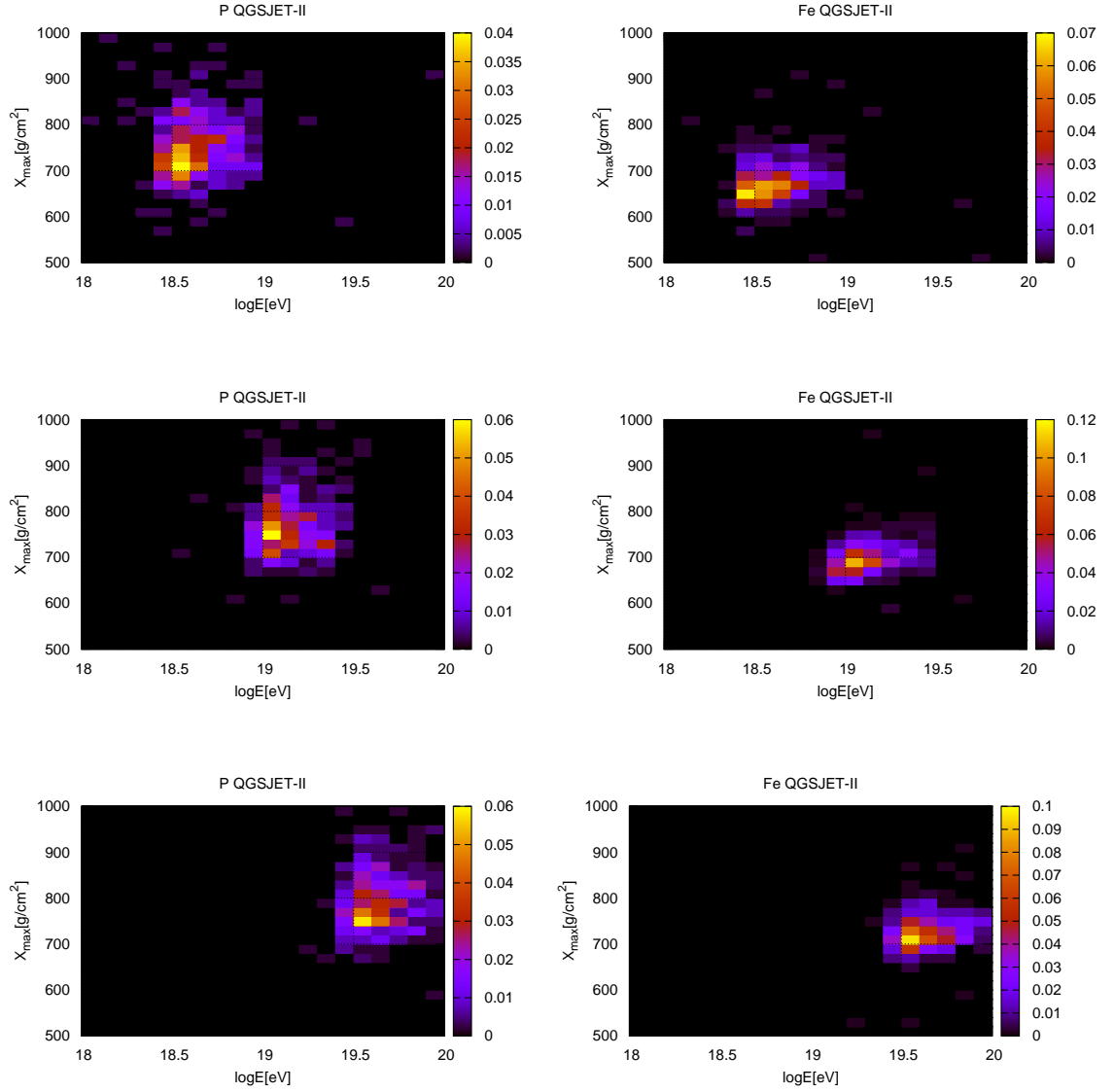
Figure 6.9: The reconstructed energies and $X_{\max}$ expected to be observed by TA FD stereo for each energy regions of $10^{18.5}$, $10^{19.0}$ and $10^{19.5}$eV (from top to bottom). Primary particles are Protons (left) or Irons (right). Hadronic model is QGSJET-II.
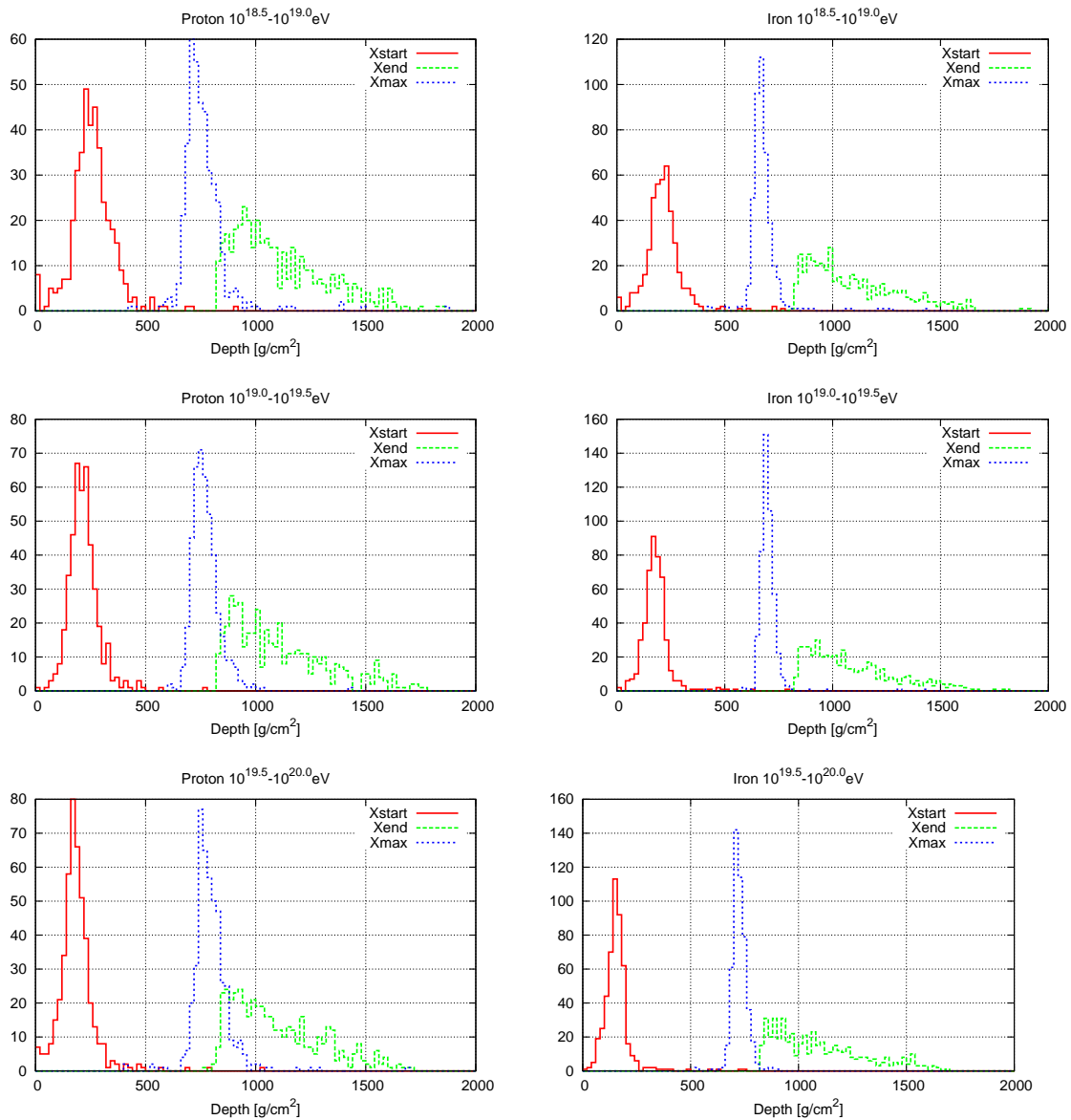
Figure 6.10: The distribution of $X_{\max}$,X_{start} and X_{end} (QGSJET-II).
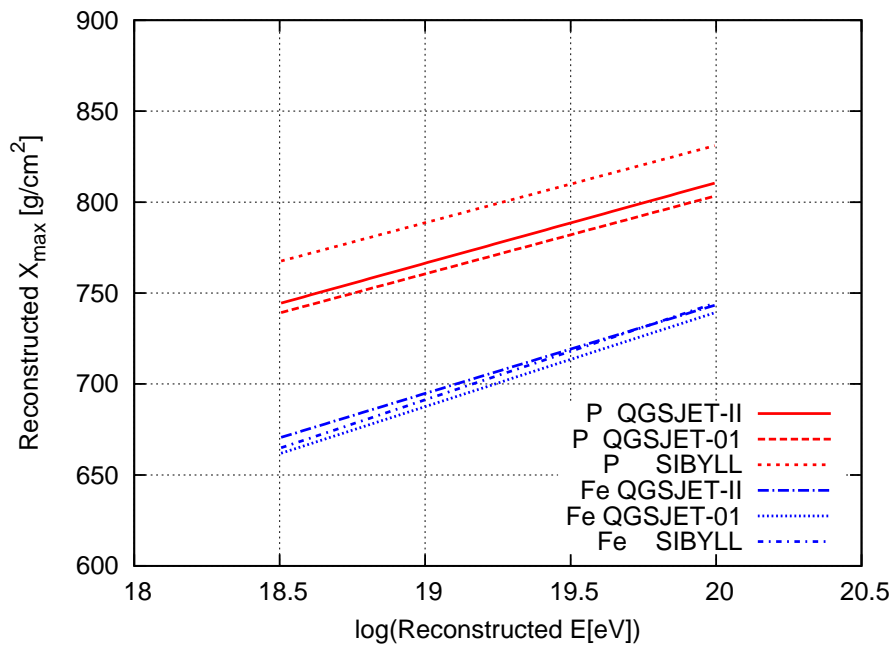
Figure 6.11: The average of reconstructed X_{max} calculated with the various hadronic interaction models, QGSJET-II, QGSJET-01 and SIBYLL.

Chapter 7

Data Analysis

7.1 FD Observation

The first test observation on July 2005 with one telescope systems at BRM site was achieved and succeeded to detect the fluorescence signals of air showers. On Mar. 2007, the trigger system which unify whole electronics in each FD station was installed completely at BRM. On July 2007, the system was installed at LR also and test observation was achieved and stereo observation was started on Nov. 2007. TA started the stereo observation with whole telescopes from Dec. 2007, two telescope stations and twelve telescopes in each. From Dec. 2007, TA achieve the observation stable. Moreover, the trigger system was updated to implement the airplane veto on Mar. 2008. Fig. 7.1 shows the observation time. In this analysis, the data set acquired by BRM and LR FD site from Nov. 2007 to Oct. 2009 will be used.

7.2 Stereo Event Selection

TA FDs can observe air showers stereoscopic. Stereo measurements improve the geometry determination than monocular measurements. The accuracy of geometry determination affect air shower reconstruction directly. In order to determine the primary energy, we have to estimate the amount of fluorescence photons attenuated with passing through the atmosphere. To calculate the degree of the attenuation, the

94
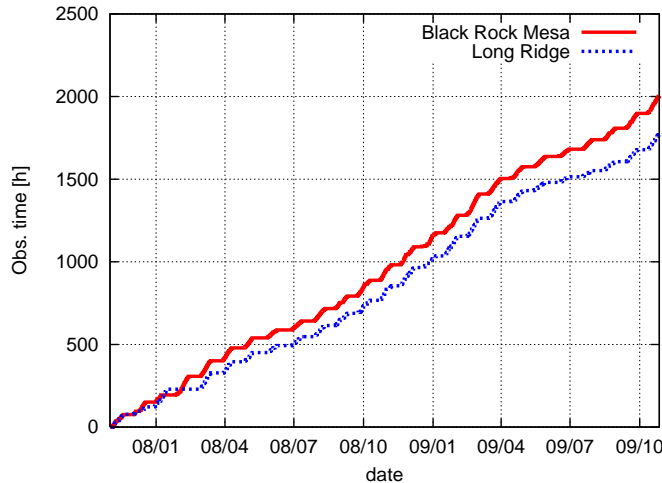
Figure 7.1: The total observation time of each FD station.

geometrical information is needed. Moreover, X_{max} resolution is also affected directly. In this analysis, stereo event are used for composition analysis because of the worse angular determination of monocular geometrical reconstruction.

Observation by two FD stations are achieved independently, so that stereo events are extracted based on the time difference between two stations. The time resolution of FD is 25ns and absolute time information is acquired by the GPS. The time difference between two FD station is simulated in Fig. 7.2, when air shower cores are distributed within the TA site, zenith angle is $0°, 60°$ and azimuth angle is randomly. In this analysis, to avoid the bias of trigger efficiency, the time differences are estimated just geometrical. This estimation is safe enough not to miss the stereo event even if very week air shower to be not triggered.

Under the criteria, not only air shower stereo events but also noise events survive. Noise events are caused by the laser shot of CLF or LIDAR, navigation light of airplanes (before airplane veto was installed) and unidentified object. It is guessed that unidentified objects are caused by the artificial light reflected by low clouds or smoke from the power station. Thus, in order to extract stereo events, simple shower selection was applied as following.

Peak time Durations of fluorescence signals caused by air showers are expected to
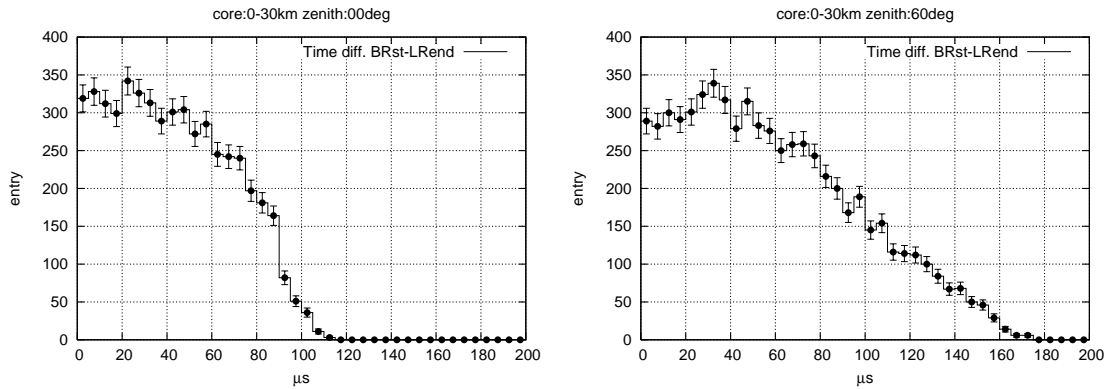
Figure 7.2: The simulated time difference the initial time at BRM station the end time at LR, where the initial time is the first time that a photon from air shower reaches at the detector and the end time is the last one.

be $\sim \mu$ s. On the other hand, Cherenkov light incident directly or muons hit PMT camera directly do not show the time difference with the resolution of TA FD, 10MHz. In this selection, when signal peak timings are distributed within 300ns, such event is excluded.

Calibration In order to monitor the detector response, shower data include the calibration data of Xe flash lamp. Such calibration data is also excluded.

CLF CLF is the beautiful stereo event although looks like up going air shower. Up going events in the specific FOV are identified CLF. CLF GPS time information log are also take into account.

Airplane Signals caused by navigation light of airplane have very long duration of $\sim$ ms or less. In a time window of data acquisition, the signals look like monotone increasing. When data include the PMTs which shows the monotone increasing, the data is identified as airplane signal. After installing the airplane veto, such events become quite rare.

Even if such event selections are applied, noise events survive which have been not expected. It is difficult to exclude automatically, but the number of such events shows the date dependence. Therefore, if the number of events per day exceeds a

hundred, the data of the noisy day are exclude explicitly. After the cut, 3060 events are survived against the 30730 events which extracted based on the time differences.

7.3 Stereo Data Analysis

For 3060 events selected by the above selections, the shower reconstruction is achieved. These events include the nose events yet, but such noise event are cut after shower reconstruction. After applying the shower reconstruction and quality cut, 248 events are extracted, where criteria of quality cut are following.

- A shower maximum, X_{max}, is observed, X_{max} is located between the X_{start} and X_{end}. X_{start} is the atmospheric depth of the most shallow point which is detected along the shower axis. X_{end} is the atmospheric depth of the deepest point which is detected along the shower axis.

- A zenith angle is less than $60°$.

The Fig. 7.3 is the shower track of one of the typical event observed on 2008/Dec/30. This event was observed by two FD stations clearly. The Fig. 7.4 is the result of shower reconstruction of the same event. The number of photoelectrons detected at the telescopes are reconstructed including the photoelectrons caused by the Cherenkov emission. This event reconstructed as following (Table 7.1).

Figure 7.5 shows the distribution of azimuth and zenith angle of the shower axis in the TA coordinate. Figure 7.6 is the scatter plot of shower cores of the stereo events. The shower cores mainly distributed around the center of 2 FD stations. The histograms of energies and X_{max} is shown in Fig. 7.7. Cosmic rays observed in the energy range of $10^{18} - 10^{20}$ eV. Figure 7.8 shows the distribution of X_{max}, X_{start} and X_{end}.

Table 7.1: The result of reconstruction of the shower data observed on 2008/Dec/30 10:49 (UTC), where azimuth is clockwise from the north and the origin of coordinate is CLF, the center of TA site.

Zenith	Azimuth	Core [km]	Energy	$X_{\max}$
3.23°	144.0°	0.086, -6.101	5.72×10^{19} eV	739.25g/cm^2
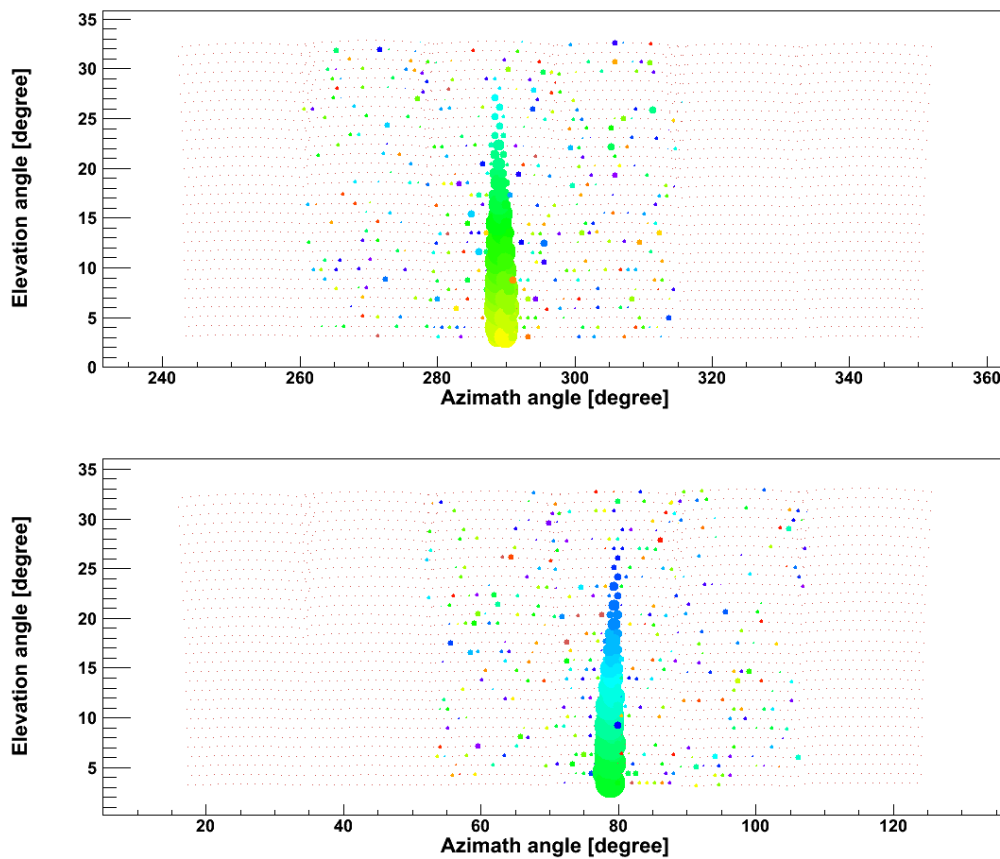
Figure 7.3: One of the shower track observed by BRM (upper) and LR (lower) station on 2008/Dec/30 10:49 (UTC). The position of colored circle corresponds the FOV of each PMT. The size and colors of circles represents the number of detected photoelectrons, and the arrival time of signals, blue to yellow.
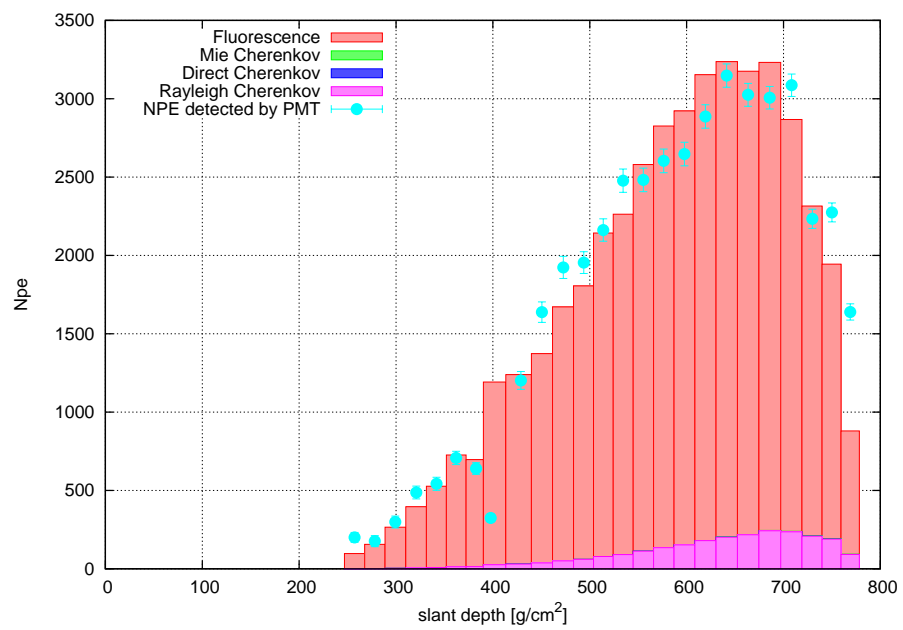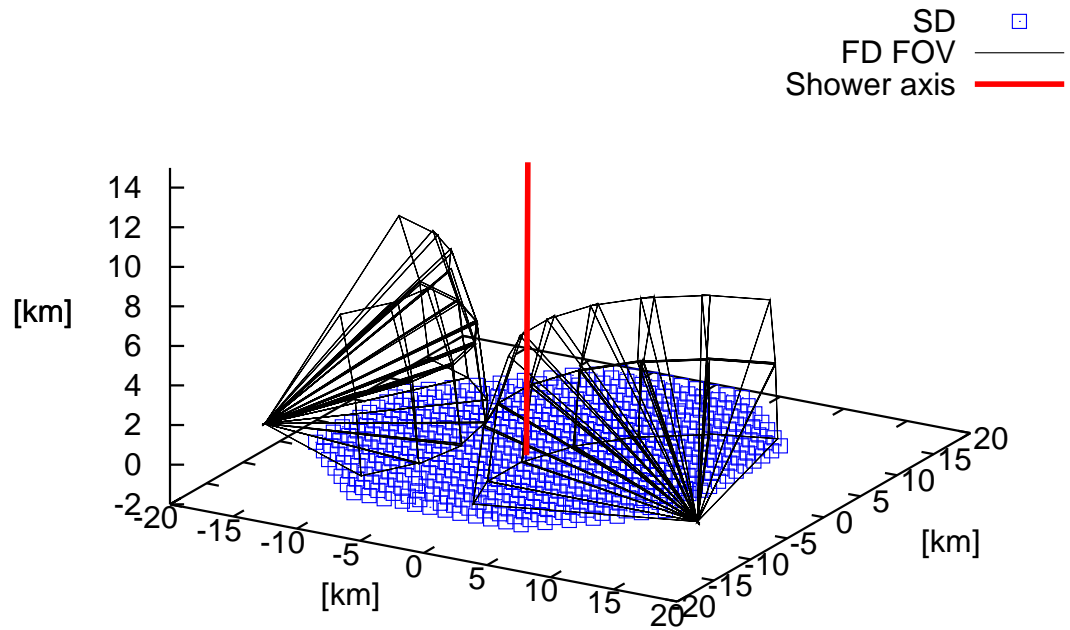
Figure 7.4: One of the reconstructed shower data observed on 2008/Dec/30 10:49 (UTC). The reconstructed shower axis (red line), in which the black line is the FOV of each telescopes and blue points are the SDs (upper) and the reconstructed ratio of photoelectrons caused by fluorescence and Cherenkov emission (lower) .
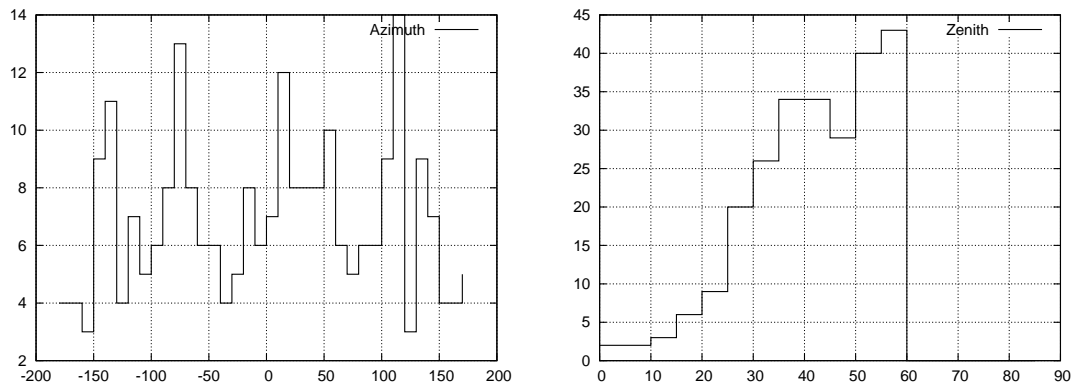
Figure 7.5: The histograms of reconstructed azimuth (left) and zenith (right) angles.
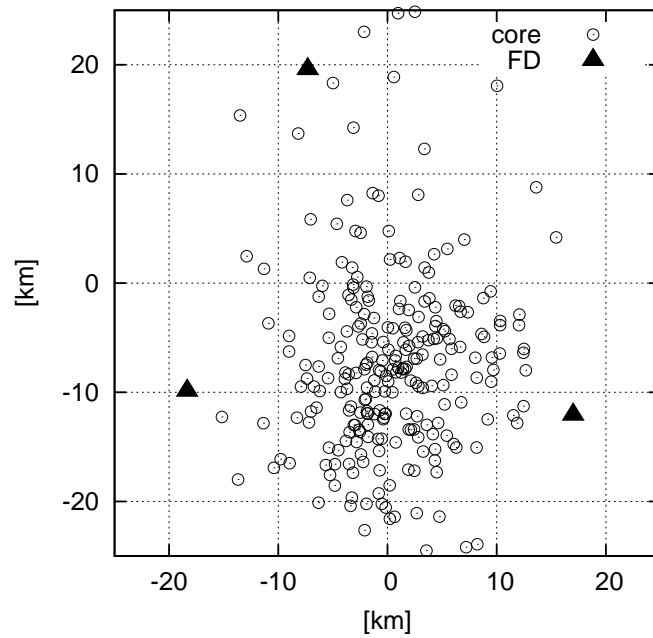
Figure 7.6: The scatter plot of reconstructed shower core positions.
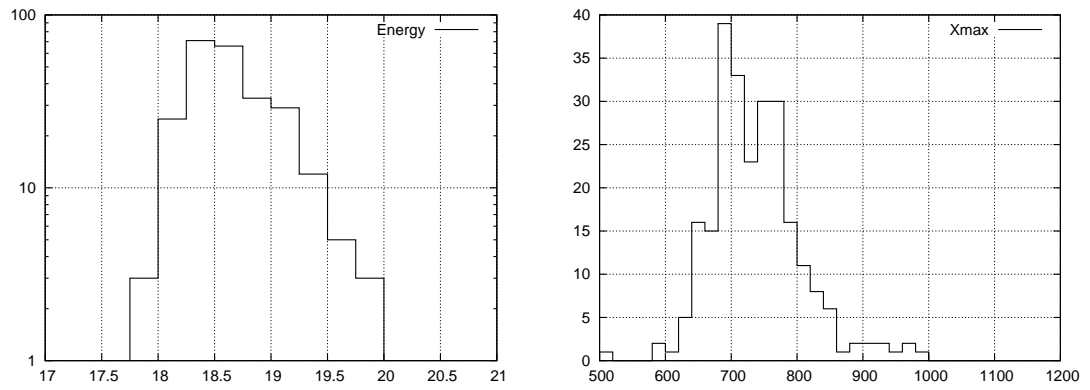
Figure 7.7: The histograms of reconstructed energies (left) and $X_{\max}$ (right).
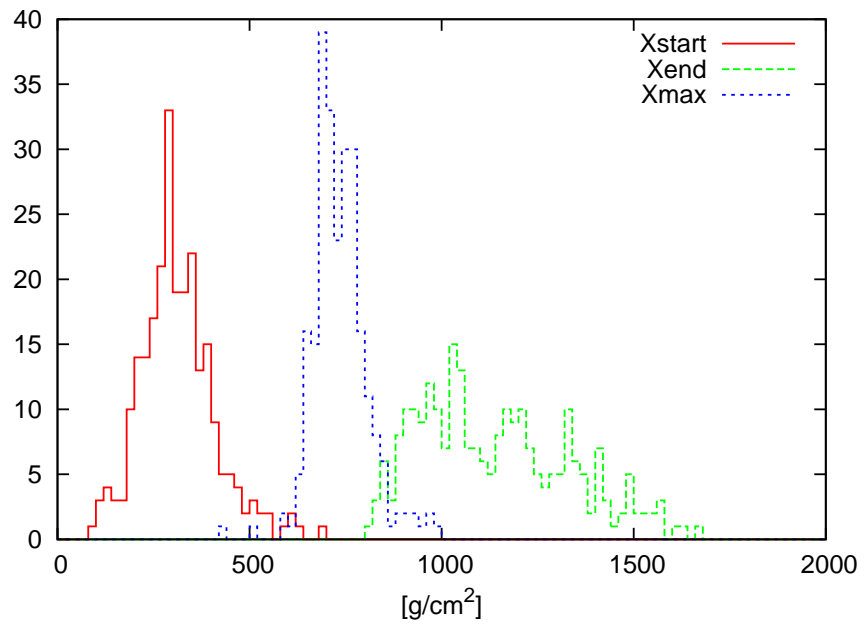
Figure 7.8: The histograms of reconstructed $X_{\max}$, X_{start} and X_{end}.

7.4   Data Comparison with Simulation

7.4.1 $X_{\max}$ Distribution

Figure 7.9 shows the comparison of $X_{\max}$ between the data and simulation. In Fig.
7.9, the histograms is of reconstructed $X_{\max}$ of simulated air showers of QGSJET-II
expected to be observed at TA FD for the protons (upper) and irons (lower), and the
points are the data. For the other interaction models of QGSJET-01 and SIBYLL,
the comparisons are shown in Figs. 7.10. The TA FD simulation is performed under
the conditions enumerated in Table 6.2. Thus, both distributions should contain
the data and simulated events which satisfy the condition as following; 1) energy is
above $10^{18.6}$eV, 2) zenith angle is less than 56°, 3) core location is within 9.6 km
from the middle point of 2 FD stations and 4) X_{mas} is within the FOV of FD. The
differences between the condition of the former and the latter is the consideration
for the contribution of the edge events of the simulation condition. For example, in
this work, only the air showers with energy above $10^{18.5}$eV were simulated but air
showers with little lower energy can be reconstructed as above $10^{18.5}$eV due to the
energy resolution of a few percent (Table 6.3). Thus, for the cut condition of energy,
zenith angle and core location, the resolution of reconstruction should be taken into
account. The air shower simulation was performed in three energy regions and the
expected distribution is compilation of three regions each of them are weighted. The
χ^2 cut is also applied for the data because of the bad fit which comes from the noise
of electronics or the influence of the atmospheric locality which are not included in
the detector simulation yet.

In spite of the low statistics, there is a good agreement between the distribution of
data and of the proton model with the chi-square / dof of 1.33. For the case of iron,
on the contrary, the chi-square / dof is 27.39. This can suggest that the iron model
is rejected with the usual significance level. The distribution of $X_{\max}$ of the pure
iron model is much shallower than that of proton, moreover the breadth of the $X_{\max}$
distribution of iron is more sharp than that of proton. Even though the systematics
originate from the uncertainty of the hadronic interaction model, the difference is
large. The chi-square / dof for iron distributions are much larger than proton, when

the X_{max} was shifted to minimize the chi-square shown in Fig. 7.11.

7.4.2 Average X_{max}

In Fig. 7.12, the reconstructed energies and X_{max} are plotted with rails of average X_{max} in Fig 6.11. Here, the same cut in 7.4.1 is also applied for the data. The distribution shows broad and this means that the proton model seems to be favored (see Fig. 6.9). From this distribution, the average X_{max} is acquired which are divided in three bins (Fig. 7.13). In the energy range from $10^{18.6}$ to $10^{19.3}$eV, the data agrees with the pure proton model of QGSJET.

In Fig. 7.14, the average X_{max} of other experiments, HiRes (upper) and PAO (lower), are plotted with the rails of various hadronic models. The average X_{max} cannot be compared directly with those of other experiments because of the differences of bias. In this work, the distribution of reconstructed X_{max} and energy includes the reconstruction bias, e.g. ~ -5 % for energy and ~ 10g/cm^2 for X_{max}, and X_{max} cut bias. In the HiRes plot, they corrected the acceptance bias of 16g/cm^2 for the data points [2], where protons are assumed as primary particles. HiRes data suggests that the composition of ultra-high energy region is dominated by purely protons. On the other hands, Auger data implies that the flux of UHECRs contains light components above the energy of $10^{18.5}$ eV [7].

7.5 Discussion

The mass composition of cosmic rays with energy above 10^{14}eV is investigated by the X_{max} technique. Below the energy of 10^{17}eV, X_{max} is observed by Cherenkov detectors, and above the energy the fluorescence technique is applied for the X_{max} measurements.

The mass composition is getting heavier from the energy of 10^{15}eV and at the energy of 10^{17}eV almost iron (Fig. 2.12). KASCADE also reported that the mass composition at 10^{17}eV is almost iron by the measurement of the energy spectra selected by mass groups or the mean mass number using the particle detectors [82].
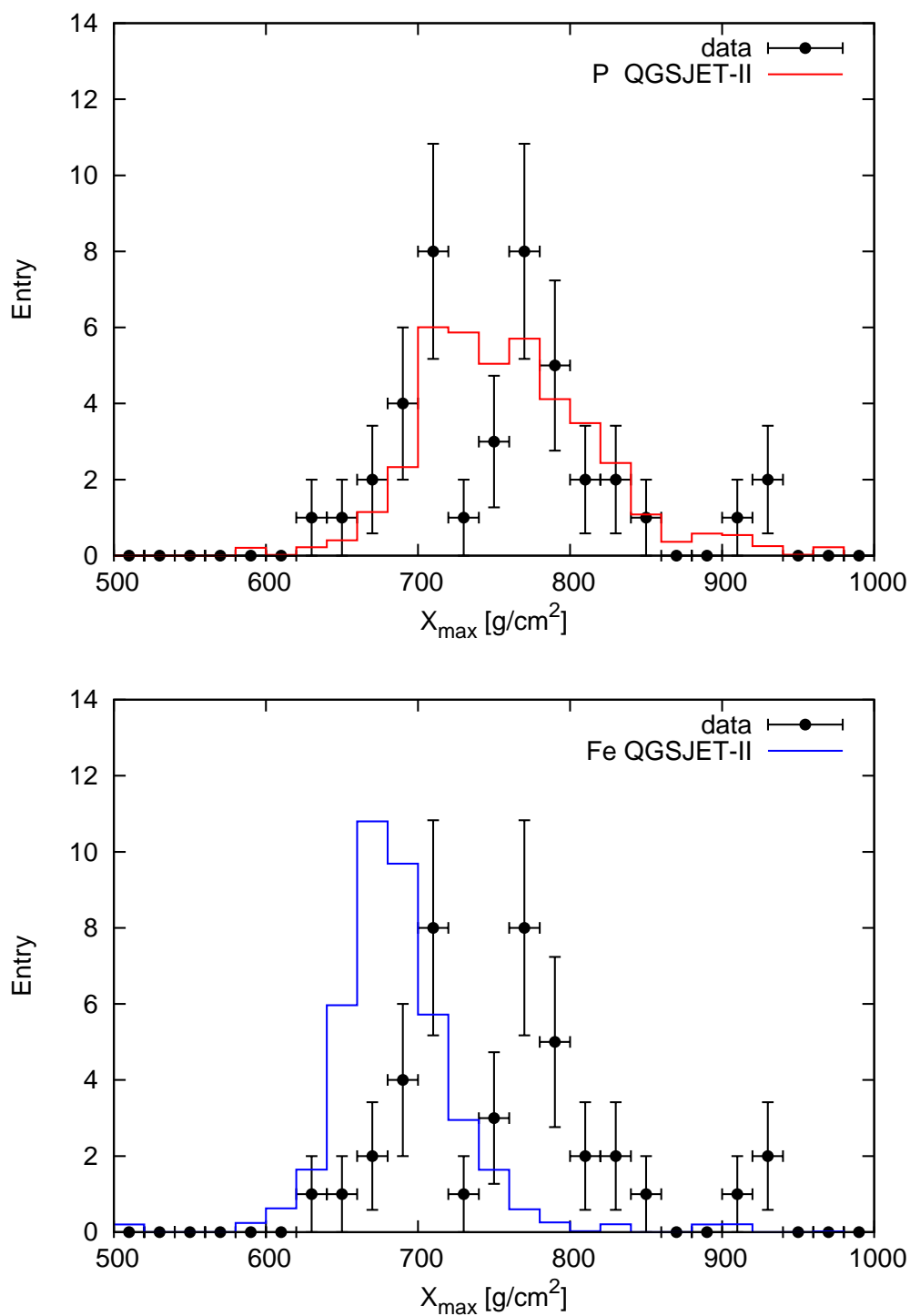
Figure 7.9: The comparisons of $X_{\max}$ between the data and simulation of proton (upper) or iron (lower) primary for the case of QGSJET-II.
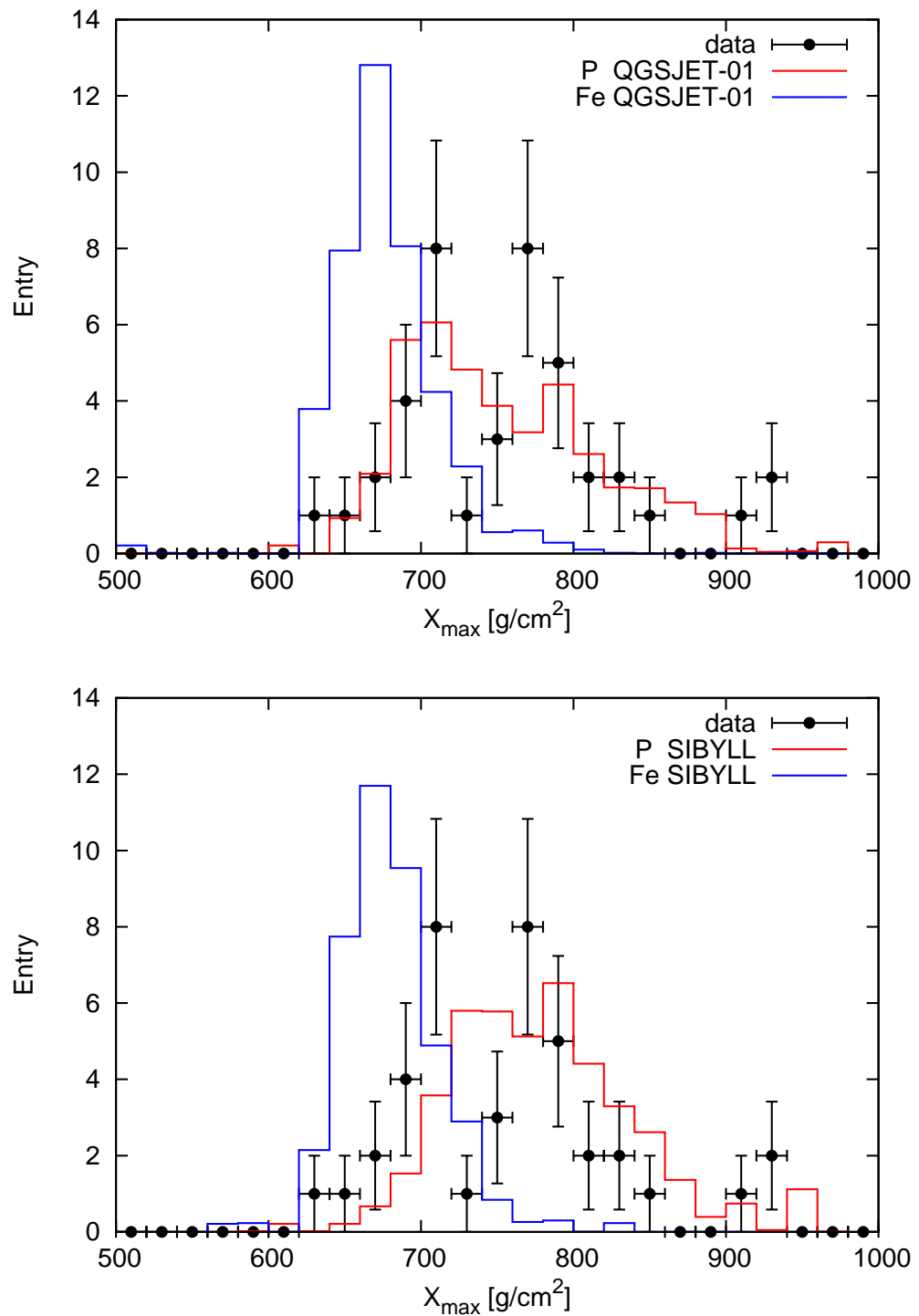
Figure 7.10: The comparisons of X_{max} between the data and simulation of pure proton (red) or iron (blue) with various hadronic interaction models; upper is QGSJET-01 and lower is SIBYLL.
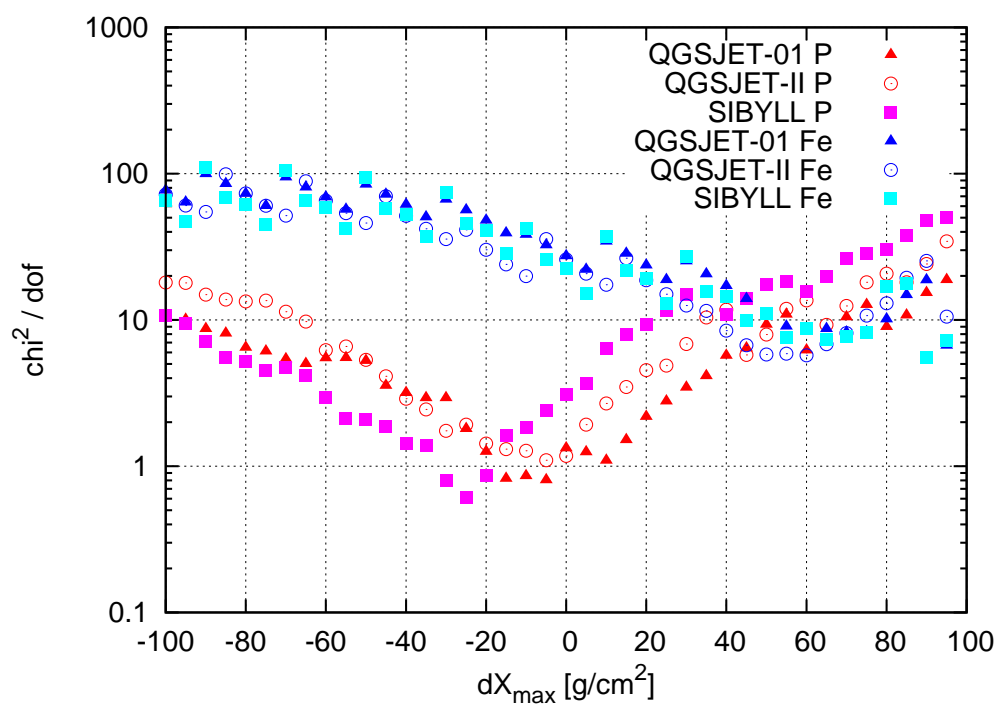
Figure 7.11: The chi-squares / dof for various models, when the $X_{\max}$ is shifted of $dX_{\max}$. In any hadronic models of iron, the chi-squares are much larger than that of proton models, even though $X_{\max}$ is shifted.
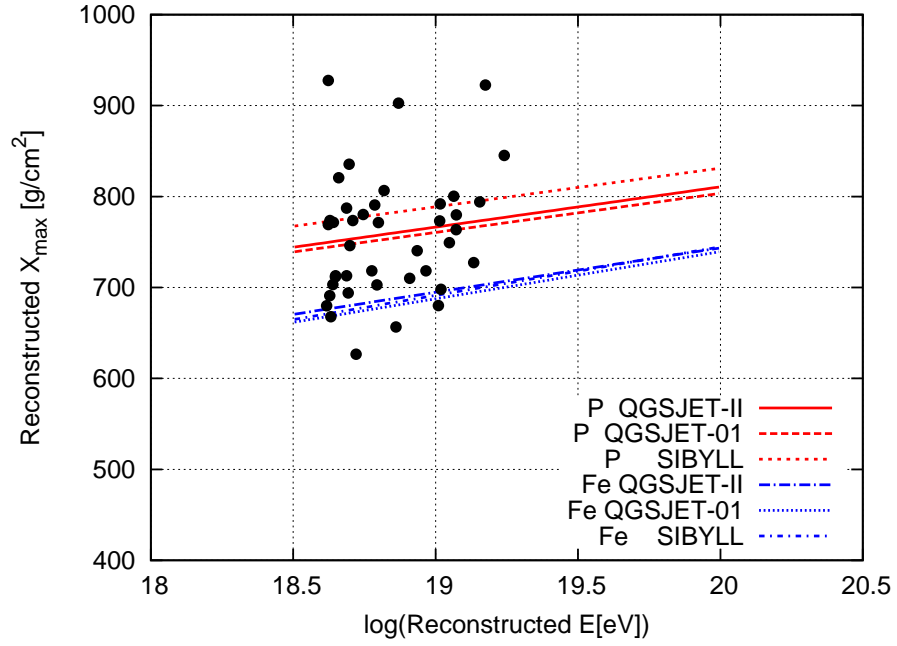
Figure 7.12: The scatter plot of reconstructed X_{max} with log energy.
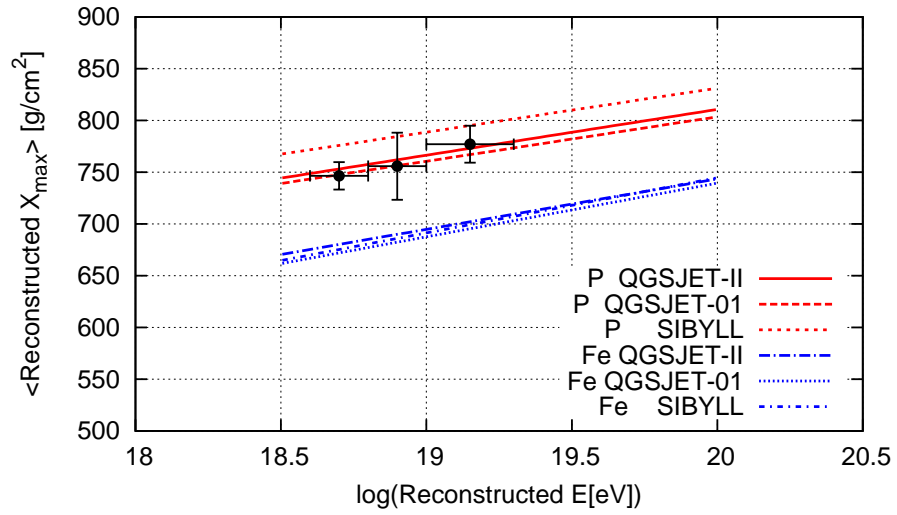
Figure 7.13: The average X_{max} compared with the average reconstructed X_{max} rails of simulation with the hadronic models of QGSJET-II, QGSJET-01 and SIBYLL.
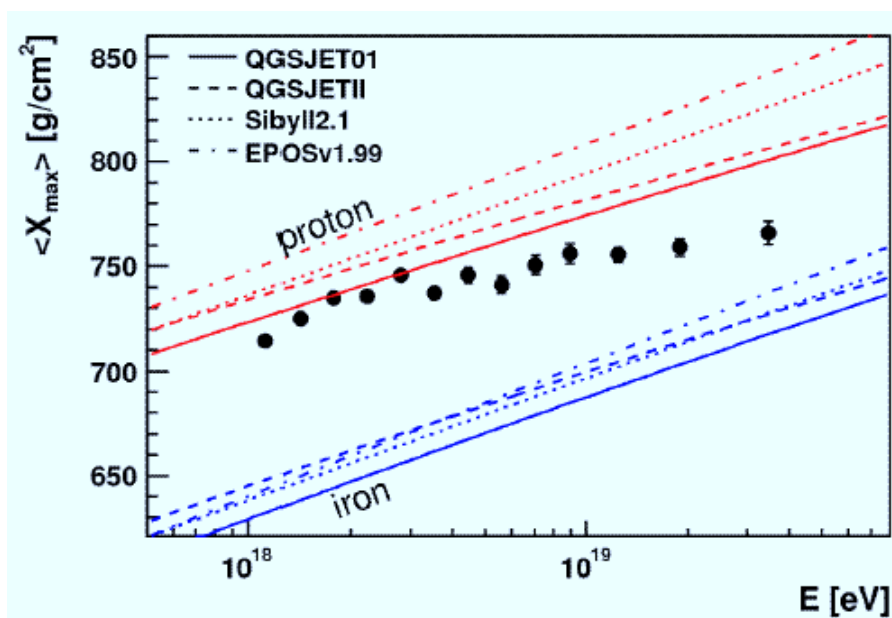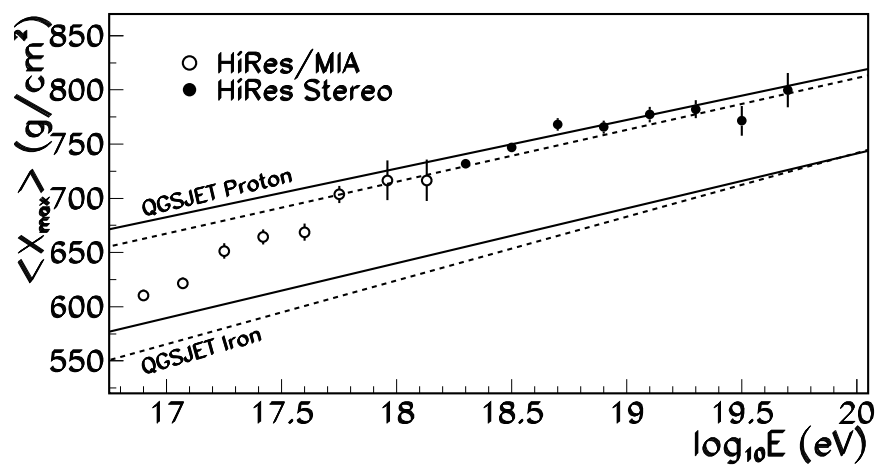
Figure 7.14: The average X_{max} of HiRes and PAO compared with the simulation with various hadronic models.

Below the energy of 10^{17}eV, cosmic rays are assumed as galactic components. The transition of mass number is explained due to the limitation of acceleration by astronomical objects or confinement in the galaxy.

Above 10^{18}eV, the mass composition seems to be changed to light components, almost protons. HiRes reported that the mass composition above 1.6×10^{18}eV is dominated by proton [18][2]. PAO, on the contrary, suggested that the mass composition changes to heavier components from $10^{18.5}$eV [7]. The comparison of the distribution of reconstructed $X_{\max}$ between the data and simulation of this work shows good agreement with the pure proton model, moreover the averaged reconstructed $X_{\max}$ is also consistent with the model.

When the mass composition of UHECRs are mainly proton, cosmic-ray sources are mainly extra galactic astronomical objects such as AGN. The scale of deflection by the galactic magnetic field is much smaller than the case of iron and the correlations between the arrival direction and the astronomical objects are expected, if the astronomical objects are active. It is also the advantage for TA FD that TA is located in the northern hemisphere and covers the anti-galactic center not to be suffered from the magnetic field of the galactic center. Thus, identification of the sources can be expected.

Not only the source models but also the interpretation of the energy spectrum shape can be constrained. At least above $10^{18.6}$eV, the mass composition is pure protons by this work, below the energy, the mass composition of HiRes and MIA or PAO is additionally proton dominated. When the mass composition above 10^{18}eV is purely proton, UHECRs can be assumed as extra galactic components. Therefore, the bending shape in the energy spectrum at the energy of $10^{18.5}$eV can be explained as the result of the interaction with the CMB photons, (dip model [14]). According to this interpretation, the energy scale of observed UHECRs can be calibrated. For the observation of UHECRs, the energy scale has been one of the crucial points for any experiments. The energy scale of AGASA type detectors strongly relies on the hadronic interaction model which cannot be established yet. On the other hand, the fluorescence technique also has uncertainties of fluorescence yield or atmospheric condition which cannot be controlled for the energy estimation. TA is constructing

the ELS to calibrate the detector efficiency and fluorescence yield in the actual atmosphere, simultaneously. The dip model, on the contrary, does not suffer from the model dependence of the injection spectrum. Thus, the energy calibration by the position of dip can be the most powerful strategy. By this work, however, the mass composition in the energy region below $10^{18.5}$eV cannot be concluded. Therefore, the transition model from the galactic to extra-galactic model[13] cannot be excluded.

From this work, the composition of UHECRs is consistent with pure proton model. Therefore, above the energy of $\sim 10^{18.6}$eV, UHECRs are almost extra galactic components. At the energy of 10^{17}eV, the composition of cosmic rays are heavy almost irons. In other words, cosmic rays around the energy are the galactic components. In the future, it is important to clarify the transition from the galactic to extra galactic components in the energy region between 10^{17} to $10^{18.5}$eV. For the purpose, TA FD analysis extends the energy region to lower energy. In the low energy region, it is difficult to observe cosmic-ray air showers with primary energy below $\sim 10^{18}$eV stereoscopically. On the other hand, the reconstruction accuracy of monocular analysis is worse than that of stereo analysis due to the difficulty of geometry determination. If there is an arrival time information of shower particle at the SD, the geometry determination is much improved. However, the trigger efficiency of SD is not enough below the energy of $10^{18.4}$eV, where the efficiency is $\sim 50\%$. Therefore, TA FD is planning the implement of hybrid trigger system, which triggers the SD events by the trigger information of FD. For the low energy observation, TA Low-energy Extension (TALE) is also planned [66], TALE project plans to install more FDs near the present FD stations to achieve the stereo observation.

Chapter 8

Conclusion

The air shower data observed by TA FD from Nov. 2007 to Oct. 2009 were re-constructed. The number of reconstructed events by stereo analysis is 248 with the condition; $\theta_{\text{zenith}} < 60°$ and $X_{\text{start}} < X_{\text{max}} < X_{\text{end}}$. The UHECR mass composition analysis is achieved by the comparison between the simulated shower data and the reconstructed data. For the shower simulation, CORSIKA code is used with the various hadronic interaction models of QGSJET-II, QGSJET-01 and SIBYLL. In this analysis, the composition model is assumed as the pure proton or pure iron. In the distribution of X_{max} (Fig. 7.9) with the selection condition of $\theta_{\text{zenith}} < 56°$, core location within 9.6 km from the middle point of 2 FDs, $E > 10^{18.6}$eV and $X_{\text{start}} < X_{\text{max}} < X_{\text{end}}$, there is a good agreement with the pure proton model of QGSJET. The average X_{max} calculated from the distribution of energies and X_{max} of the data (Fig. 7.13) is also consistent with the pure proton composition model of QGSJET within the error bars in the energy region from $10^{18.6}$ to $10^{19.3}$ eV.

In the case of HiRes-MIA and HiRes stereo, the mass composition changes from heavy to light component up to 10^{18}eV, and is dominated by purely proton above the energy [18, 2]. The PAO, on the contrary, reported that the mass composition is protonic only up to $10^{18.5}$eV and getting heavier above the energy [7]. The above results are derived by the average and RMS of X_{max} study. This work suggests that the mass composition from from $10^{18.6}$ to $10^{19.3}$ eV is consistent with the pure proton model by not only the average but also the distribution of X_{max}.

It is quite important to determine the mass composition with wider energy region for the clarification of the origins of UHECRs. For the transition from the galactic to extra-galactic component, the mass composition of lower energy region below $10^{18.5}$eV is especially powerful information. The stereo detection efficiency below the energy, however, is getting worse and moreover the the determination of arrival direction by mono analysis is much worse than stereo analysis. Therefore, TA is planning the implement of hybrid trigger system from FD to SD for not triggered low energy events by the current SD trigger system. This is because, the timing information of SDs improves the geometrical reconstruction [42]. TA Low-energy Extension is also planned, in which FDs are deployed near the present FD stations for stereo observation of lower energy cosmic rays [66].

Appendix

Abbreviations

BRM	Black Rock Mesa (FD site)
CLF	Central Laser Facility
CRAYS	Calibration using RAYLeight Scattering
CTD	Central Trigger Distributor module
CPLD	Complex Programmable Logic Device
DAQ	Data Acquisition
ELS	Electron Light Source
FADC	Flash Analog Digital Converter
FD	Fluorescence Detector
FOV	Field of View
FPGA	Field Programmable Gate Array
G-H function	Gaisser-Hillas function
GPS	Global Positioning System
GZK cutoff	Greisen-Zatsepin-Kuzmin cutoff
IMC	Inverse Monte Carlo
LIDAR	LIght Detection And Ranging
LR	Long Ridge (FD site)
MD	Middle Drum (FD site)
NKG function	Nishimura-Kamata-Greisen function
PAO	Pierre Auger Observatory
PMT	Photomultiplier Tube
SD	Surface Detector
SDF	Signal Digitizer and Finder module
TA	Telescope Array
TF	Track Finder module

Acknowledgments

Reference

[1] Abbasi R, Abu-Zayyad T, Al-Seady M, et al. *Astroparticle Physics*, 32(1):53 – 60, 2009.

[2] Abbasi R, Abu-Zayyad T, Al-Seady M, et al. *submitted to Physical Review Letters*.

[3] Abbasi R, Abu-Zayyad T, Allen M, et al. *Physical Review Letters*, 100(10):101101, 2008.

[4] Abbasi R, Abu-Zayyad T, Amann J, et al. *Astroparticle Physics*, 22(2):139 – 149, 2004.

[5] Abbasi R, Abu-Zayyad T, Amann J, et al. *Astroparticle Physics*, 25(1):74 – 83, 2006.

[6] Abbasi R, Abu-Zayyad T, Belov K, et al. *Astroparticle Physics*, 29(1):77 – 86, 2008.

[7] Abraham J, Abreu P, Aglietta M, et al. *the 31th International Cosmic Ray Conference, Lodz, Poland*, 2009.

[8] Abraham J, Abreu P, Aglietta M, et al. *Astroparticle Physics*, 29(3):188 – 204, 2008.

[9] Abraham J, Abreu P, Aglietta M, et al. *Phys. Rev. Lett.*, 101(6):061101, 2008.

[10] Abraham J, Aglietta M, Aguirre I, et al. *Nuclear Instruments and Methods in Physics Research Section A: Accelerators, Spectrometers, Detectors and Associated Equipment*, 523(1-2):50 – 95, 2004.

[11] Abu-Zayyad T, Al-Seady M, Belov K, et al. *Nuclear Instruments and Methods in Physics Research Section A: Accelerators, Spectrometers, Detectors and Associated Equipment*, 450(2-3):253 – 269, 2000.

[12] Ahn E, Medina-Tanco G, Biermann P, et al. *ArXiv Astrophysics e-prints*, November 1999.

[13] Allard D, Parizot E, Olinto A. *Astroparticle Physics*, 27(1):61 – 75, 2007.

[14] Aloisio R, Berezinsky V, Blasi P, et al. *Astroparticle Physics*, 27(1):76 – 91, 2007.

[15] Ave M, Bohacova M, Buonomo B, et al. *Astroparticle Physics*, 28(1):41 – 57, 2007.

[16] Baltrusaitis R, Cady R, Cassiday G, et al. *Nuclear Instruments and Methods in Physics Research Section A: Accelerators, Spectrometers, Detectors and Associated Equipment*, 240(2):410 – 428, 1985.

[17] Bird D, Corbato S, Dai H, et al. *Astrophysical Journal*, 424:491–502, March 1994.

[18] Bird D, Corbató S, Dai H, et al. *Phys. Rev. Lett.*, 71(21):3401–3404, Nov 1993.

[19] Blandford R, Eichler D. *Physics Reports*, 154(1):1 – 75, 1987.

[20] Blasi P, Epstein R, , et al. *The Astrophysical Journal Letters*, 533(2):L123–L126, 2000.

[21] Boldt E, Ghosh P. *Monthly Notices of the Royal Astronomical Society*, 307:491–494, August 1999.

[22] Boothby K, Chantell M, Green K, et al. *The Astrophysical Journal Letters*, 491(1):L35–L38, 1997.

[23] Bunner A. PhD thesis, Cornell University, 1967.

[24] Cesarsky C. *Ann. Rev. Astron. Astrophys.*, 18:289, 1980.

[25] Coleman S, Glashow S. *Phys. Rev. D*, 59(11):116008, Apr 1999.

[26] Cronin J. *Nuclear Physics B - Proceedings Supplements*, 138:465 – 491, 2005. Proceedings of the Eighth International Workshop on Topics in Astroparticle and Undeground Physics.

[27] Dickinson J, et. al. *the 26th International Cosmic Ray Conference*, 3:136, 1999.

[28] Dova M, Mancenido M, Mariazzi A, et al. *Astroparticle Physics*, 31(4):312 – 319, 2009.

[29] Duda R, Hart P. *Comm. ACM*, 15:11–15, 1972.

[30] Egorova V, Glushkov A, Ivanov A, et al. *Nuclear Physics B - Proceedings Supplements*, 136:3 – 11, 2004. CRIS 2004 Proceedings of the Cosmic Ray International Seminars: GZK and Surroundings.

[31] Fermi E. *Phys. Rev.*, 75(8):1169–1174, Apr 1949.

[32] Fletcher R, Gaisser T, Lipari P, et al. *Phys. Rev. D*, 50(9):5710–5731, Nov 1994.

[33] Fowler J, Fortson L, Jui C, et al. *Astroparticle Physics*, 15(1):49 – 64, 2001.

[34] Gaisser T, Hillas A. *the 15th International Cosmic Ray Conference*, 1977.

[35] Greisen K. *Ann. Rev. Nucl. sci*, 10:63, 1960.

[36] Greisen K. *Phys. Rev. Lett.*, 16(17):748–750, Apr 1966.

[37] Hayashida N, Honda K, Honda M, et al. *Journal of Physics G: Nuclear and Particle Physics*, 21(8):1101–1119, 1995.

[38] Heck D, et. al. Report fzka 6019. Technical report, Forschungszentrum Karlsruhe, 1998.

[39] Hillas A. *Journal of Physics G: Nuclear Physics*, 8(10):1461–1473, 1982.

[40] Hillas A. *Annual Review of Astronomy and Astrophysics*, 22(1):425–444, 1984.

[41] Hillas A, Lapiken J. *the 15th International Cosmic Ray Conference*, 1977.

[42] Ikeda D, Sagawa H, Tsunesada Y, et al. *the 31th International Cosmic Ray Conference, Lodz, Poland*, 2009.

[43] Kakimoto F, Loh E, Nagano M, et al. *Nuclear Instruments & Methods in Physics Research, Section A: Accelerators, Spectrometers, Detectors and Associated Equipment*, 372(3):527–533, 1996.

[44] Kalmykov N, Ostapchenko S, Pavlov A. *Nuclear Physics B - Proceedings Supplements*, 52(3):17 – 28, 1997.

[45] Kamata K, Nishimura J. *Progress of Theoretical Physics Supplement*, 6:93–155, 1958.

[46] Kang H, Ryu D, Jones TW. *The Astrophysical Journal*, 456:422–+, January 1996.

[47] Kawai H, Yoshida S, Yoshii H, et al. *Nuclear Physics B - Proceedings Supplements*, 175-176:221 – 226, 2008. Proceedings of the XIV International Symposium on Very High Energy Cosmic Ray Interactions.

[48] Kawana S, Inoue N, Fukushima M, et al. *the 31th International Cosmic Ray Conference, Lodz, Poland*, 2009.

[49] Kobayashi M, Shinkawa T, Sato T, et al. *Nuclear Instruments and Methods in Physics Research Section A: Accelerators, Spectrometers, Detectors and Associated Equipment*, 337(2-3):355 – 361, 1994.

[50] Kronberg P. *Reports on Progress in Physics*, 57(4):325–382, 1994.

[51] Lawrence M, Reid R, Watson A. *Journal of Physics G: Nuclear and Particle Physics*, 17(5):733–757, 1991.

[52] Linsley J. *Phys. Rev. Lett.*, 10(4):146–148, Feb 1963.

[53] Nagano M, Kobayakawa K, Sakaki N, et al. *Astroparticle Physics*, 20(3):293 – 309, 2003.

[54] Nerling F, Blumer J, Engel R, et al. *Astroparticle Physics*, 24(6):421 – 437, 2006.

[55] Nonaka T, Okuda T, , et al. *the 31th International Cosmic Ray Conference, Lodz, Poland*, 2009.

[56] Olinto A. *Physics Reports*, 333-334:329 – 348, 2000.

[57] Ostapchenko S. *Nuclear Physics B - Proceedings Supplements*, 151(1):143 – 146, 2006. VERY HIGH ENERGY COSMIC RAY INTERACTIONS.

[58] Ostrowski M. *Astron. Astrophys.*, 335:134–144, July 1998.

[59] Paling S, et. al. *the 25th International Cosmic Ray Conference*, 5:253, 1997.

[60] Peter B. *Nuovo Cimento*, 22(4):800 – 819, 1961.

[61] Puget J, Stecker F, Bredekamp J. *The Astrophysical Journal*, 205:638–654, April 1976.

[62] Rachen J, Biermann P. *Astron. Astrophys.*, 272:161–+, May 1993.

[63] Sako T, Adriani O, Bonechi L, et al. *Nuclear Instruments and Methods in Physics Research Section A: Accelerators, Spectrometers, Detectors and Associated Equipment*, 578(1):146 – 159, 2007.

[64] Sakurai N, Yoshida S, Sagawa H, et al. *the 30th International Cosmic Ray Conference, Merida, Mexico*, 2007.

[65] Sato H, Tati T. *Progress of Theoretical Physics*, 47(5):1788–1790, 1972.

[66] Scott L, Bergman D, Hughes G, et al. *the 31th International Cosmic Ray Conference, Lodz, Poland*, 2009.

[67] Shibata T, Enomoto A, Fukuda S, et al. *Nuclear Instruments and Methods in Physics Research Section A: Accelerators, Spectrometers, Detectors and Associated Equipment*, 597(1):61 – 66, 2008. Proceedings of the 5th Fluorescence Workshop.

[68] Stecker F. *Nuclear Physics B - Proceedings Supplements*, 136:309 – 318, 2004. CRIS 2004 Proceedings of the Cosmic Ray International Seminars: GZK and Surroundings.

[69] Suga K. *Proc. 5th Interamerican Seminar on Cosmic Rays, Lapaz, Bolivia*, II:XLIX, 1962.

[70] Svetlana K, et. al. *the 27th International Cosmic Ray Conference*, 1:145, 2001.

[71] Swordy S. *Space Science Reviews*, 99(1/4):85–94, 2001.

[72] Takami H, Sato K. *The Astrophysical Journal*, 681(2):1279–1286, 2008.

[73] Takeda M, Hayashida N, Honda K, et al. *Phys. Rev. Lett.*, 81(6):1163–1166, Aug 1998.

[74] Takeda M, Hayashida N, Honda K, et al. *The Astrophysical Journal*, 522:225, 1999.

[75] Takeda M, Hayashida N, Honda K, et al. *The Astrophysical Journal*, 522(1):225–237, 1999.

[76] Taketa A, Fukushima M, Ohoka H, et al. *the 29th International Cosmic Ray Conference, Pune, India*, 2005.

[77] Thompson C, Duncan R. *Monthly Notices of the Royal Astronomical Society*, 275:255–300, July 1995.

[78] Tokuno H, Murano Y, Kawana S, et al. *Nuclear Instruments and Methods in Physics Research Section A: Accelerators, Spectrometers, Detectors and Associated Equipment*, 601(3):364 – 371, 2009.

[79] Tomida T, Tsuyuguchi Y, Ukai H, et al. *the 31th International Cosmic Ray Conference, Lodz, Poland*, 2009.

[80] Uchihori Y, Nagano M, Takeda M, et al. *Astroparticle Physics*, 13(2-3):151 – 160, 2000.

[81] Udo S, Cady R, Fukushima M, et al. *the 30th International Cosmic Ray Conference, Merida, Mexico*, 2007.

[82] Ulrich H, Antoni T, Apel W, et al. *the 27th International Cosmic Ray Conference, Hamburg*, 2001.

[83] Venkatesan A, Miller M, , et al. *The Astrophysical Journal*, 484(1):323–328, 1997.

[84] Vietri M. *Astrophysical Journal*, 453:883–+, November 1995.

[85] Waldenmaier T, Blumer J, Klages H. *Astroparticle Physics*, 29(3):205 – 222, 2008.

[86] Waxman E. *Phys. Rev. Lett.*, 75(3):386–389, Jul 1995.

[87] Waxman E, Miralda-Escude J. *The Astrophysical Journal Letters*, 472(2):L89–L92, 1996.

[88] Weiler T. *Astroparticle Physics*, 11(3):303 – 316, 1999.

[89] Yoshida S, Dai H. *Journal of Physics G: Nuclear and Particle Physics*, 24(5):905–938, 1998.

[90] Yoshida S, Teshima M. *Progress of theoretical physics*, 89(4):833–845, 19930425.

[91] Zatsepin G, Kuzmin V. *JETP Letters*, 4(3), 1966.

List of Figures

List of Tables